

**DEVELOPMENT OF MICROMACHINED PROBES FOR BIO-NANO
APPLICATIONS**

A Dissertation

by

MURAT KAYA YAPICI

Submitted to the Office of Graduate Studies of
Texas A&M University
in partial fulfillment of the requirements for the degree of

DOCTOR OF PHILOSOPHY

August 2009

Major Subject: Electrical Engineering

**DEVELOPMENT OF MICROMACHINED PROBES FOR BIO-NANO
APPLICATIONS**

A Dissertation

by

MURAT KAYA YAPICI

Submitted to the Office of Graduate Studies of
Texas A&M University
in partial fulfillment of the requirements for the degree of

DOCTOR OF PHILOSOPHY

Approved by:

Chair of Committee,	Jun Zou
Committee Members,	Christi K. Madsen
	Arum Han
	Hong Liang
Head of Department,	Costas Georgiades

August 2009

Major Subject: Electrical Engineering

ABSTRACT

Development of Micromachined Probes for Bio-Nano Applications.

(August 2009)

Murat Kaya Yapici, B.S., Texas A&M University

Chair of Advisory Committee: Dr. Jun Zou

The most commonly known macro scale probing devices are simply comprised of metallic leads used for measuring electrical signals. On the other hand, micromachined probing devices are realized using microfabrication techniques and are capable of providing very fine, micro/nano scale interaction with matter; along with a broad range of applications made possible by incorporating MEMS sensing and actuation techniques. Micromachined probes consist of a well-defined tip structure that determines the interaction space, and a transduction mechanism that could be used for sensing a change, imparting external stimuli or manipulating matter.

Several micromachined probes intended for biological and nanotechnology applications were fabricated, characterized and tested. Probes were developed under two major categories. The first category consists of Micro Electromagnetic Probes for biological applications such as single cell, particle, droplet manipulation and neuron stimulation applications; whereas the second category targets novel Scanning Probe topologies suitable for direct nanopatterning, variable resolution scanning probe/dip-pen nanolithography, and biomechanics applications.

The functionality and versatility of micromachined probes for a broad range of micro and nanotechnology applications is successfully demonstrated throughout the five different probes/applications that were studied. It is believed that, the unique advantages of precise positioning capability, confinement of interaction as determined by the probe tip geometry, and special sensor/actuator mechanisms incorporated through MEMS technologies will render micromachined probes as indispensable tools for microsystems and nanotechnology studies.

*for my parents
Selma and Cahit
and in loving memory of my grandmother Vesile*

ACKNOWLEDGEMENTS

Foremost, I wish to express my profound gratitude to my advisor, Dr. Jun Zou, who has been a great source of inspiration, and who has provided invaluable scientific guidance in various aspects of my research. I am especially thankful to him for giving me the opportunity to work on a variety of projects related to the work presented herein.

I would also like to thank Dr. Hong Liang. She shared her invaluable experience and knowledge in the surface science and tribology area. I am thankful to her and members of her research group for their fruitful collaborations on various projects during my graduate study. I would like to thank Dr. Christi K. Madsen and Dr. Arum Han for their constructive comments at various stages in this work. I also would like to thank them for their commitment and sincere efforts for providing a good working environment in the Solid State Labs.

I wish to thank Dr. Donald Naugle and Dr. A. Esad Ozmetin for being great collaborators. I would like to thank them for sharing their broad experience and facilities. Their expertise in magnetic characterization helped me to accurately test and characterize some of the devices presented in this work. I also would like to thank Dr. Zhendong Cheng and Dr. Dawei Luo for their help on micro droplet synthesis.

I would like to thank several research group members I worked with over the past years. And special thanks go to my friends whose existence made my stay at Texas A&M an enjoyable and a memorable one; they know who they are.

Last, but most importantly, the continuous courage and support received from my family is sincerely appreciated. I would like to thank my brother, Dr. Guney Guven Yapici for being a friend, roommate, colleague and a consultant during my graduate study. I want to thank my aunt Muzeyyen for her endless love and support ever since I have known myself. The immense love of my parents, Selma and Cahit Yapici, has been a key aspect in the construction of my graduate work. Without their support, this work would not be possible.

TABLE OF CONTENTS

	Page
ABSTRACT	iii
DEDICATION	iv
ACKNOWLEDGMENTS.....	v
TABLE OF CONTENTS	vi
LIST OF FIGURES.....	viii
LIST OF TABLES	xiii
 CHAPTER	
I INTRODUCTION.....	1
1.1 Motivation	1
1.2 Summary of Works	2
II MEMS-BASED MICRO ELECTROMAGNETIC PROBE FOR BIOLOGICAL MANIPULATION AND STIMULATION	5
2.1 Introduction	5
2.2 Device Design and Simulation	7
2.3 Device Fabrication	9
2.4 Experimental Characterization	13
2.5 Magnetic Particle Manipulation	20
2.6 Discussion and Conclusions	22
III PERMALLOY-COATED TUNGSTEN MICRO ELECTROMAGNETIC PROBE FOR MICRO DROPLET MANIPULATION	23
3.1 Introduction	23
3.2 Probe Development	25
3.3 Droplet Synthesis	37
3.4 Droplet Manipulation	38
3.5 Results and Discussion.....	42
3.6 Conclusions	44

CHAPTER	Page
IV GOLD-COATED SCANNING PROBES FOR DIRECT WRITE OF SUB-MICRON METALLIC STRUCTURES	45
4.1 Introduction	45
4.2 Principle of Material Transfer	46
4.3 Probe Fabrication	47
4.4 Experimental Results.....	50
4.5 Conclusions	53
V SCANNING PROBES WITH PRECISELY DEFINED TIP CONTACT AREAS FOR SCANNING PROBE LITHOGRAPHY	54
5.1 Introduction	54
5.2 Principle and Validation	56
5.3 Fabrication of Scanning Probe Array with Different Tip Contact Area	60
5.4 Demonstration of Variable-Resolution SPL	67
5.5 Conclusions	70
VI MICROFABRICATION OF COLLOIDAL SCANNING PROBES WITH DIFFERENT TIP RADII OF CURVATURE.....	71
6.1 Introduction	71
6.2 Process Principle	74
6.3 Process Development and Validation	76
6.4 Discussion and Conclusions	84
VII CONCLUSIONS	85
REFERENCES	86
VITA	97

LIST OF FIGURES

	Page
Figure 1. Schematic of the micro electromagnetic probe to be developed. It consists of a supporting substrate, a solenoid conducting coil and a protruding (permalloy) magnetic core with a sharp tip.	8
Figure 2. Simulated magnetic field distribution of different probe tip designs: (a) Field distribution of a probe tip with a taper angle of 15.2° ; (b) Field distribution of a probe tip with a taper angle of 43.6° ; (c) Field distribution of a four-tip design; (d) Line plot in log-log scale showing the rapid fall of the magnetic field with respect to distance from the probe tip for a probe design with taper angle 15.2° , shown in the inset is a pictorial representation of the simulation conditions.	10
Figure 3. An illustration of the fabrication process for the micro electromagnetic probe: (a) Fabrication of gold bottom conductors and SU-8 insulation and guiding structures; (b) Fabrication of the permalloy magnetic cores; (c) Assembly of the magnetic core on the chip and placement of the top conductors with wire bonding.....	11
Figure 4. (a) Scanning electron micrograph of a fabricated micro electromagnetic probe; (b) Optical microscopy pictures of permalloy magnetic cores with different tip profiles.	13
Figure 5. Scanning Hall probe microscope setup for micro electromagnetic probe characterization. The gap between the probe tip and Hall sensor is estimated to be $\sim 20\ \mu\text{m}$	14
Figure 6. (a) Finite element simulation showing the temperature distribution on the micro electromagnetic probe under 300 mA input current; (b) Plot of the probe tip temperature under different input current levels.	15
Figure 7. Magnetic field output $20\ \mu\text{m}$ from the tip of the tested micro electromagnetic probe as a function of input current.	17
Figure 8. The B-H curve of the permalloy magnetic core characterized by the scanning Hall probe microscope located about $20\ \mu\text{m}$ from the tip of the core.....	17
Figure 9. Measured spatial distribution of the magnetic field output (the component parallel to the axis of the probe) with an input current of 300 mA: (a) surface plot; (b) and (c) axial field plots along the diagonals of the probe tip obtained from the cross-sectional field distribution.	18

Figure 10.	Manipulation of fluorescent magnetic particles using the developed electromagnetic probe (observed under a fluorescence microscope): (a) Magnetic particles stay in their equilibrium position; (b) and (c) After the probe is turned on, magnetic particles move steadily towards the probe tip.	21
Figure 11.	Manipulation of magnetic particle agglomerate: (a) At $t = 0$ s, magnetic field is applied; (b) At $t = 2$ s, magnetic agglomerate moves toward the probe tip; (c) At $t = 4$ s, magnetic agglomerate is captured.	21
Figure 12.	Schematic diagram of probe-based manipulation of droplets. The use of multiple magnetic probes and micromanipulators allows complex droplet manipulation.....	24
Figure 13.	Schematic design of the new electromagnetic probe with a hybrid magnetic core.	26
Figure 14.	Finite element simulation of the magnetic field generated by a permalloy-coated tungsten probe: (a) The spatial field distribution below the tip; (b) The line plot (in log scale) of the magnetic field vs. the distance from the probe tip.	28
Figure 15.	(a) Schematic of a typical electroplating setup, where the entire target is exposed to the plating solution, with large anode-cathode separations; (b) Scanning electron micrographs of the commercially obtained tungsten needle before permalloy coating; (c) Scanning electron micrographs of the commercially obtained tungsten needle after permalloy coating.	30
Figure 16.	Illustration of the deposition rate necessary to preserve the tip profile. In order to have the same probe profile ($\alpha_1 = \alpha_2$) or decrease the taper angle ($\alpha_2 < \alpha_1$), the deposition ratio $\Delta x / \Delta y$ should be less than or equal to $\tan(\alpha_1)$ or w/l . The grey region represents the original tungsten needle structure.	31
Figure 17.	Finite element simulation showing the current density distribution on the tungsten probe.	32
Figure 18.	(a) Schematic of the new electroplating setup to enable controlled plating of permalloy; (b) the actual setup.	33
Figure 19.	Scanning electron micrograph of a permalloy-coated tungsten needle using the new plating setup.....	34
Figure 20.	Optical image of the permalloy-coated tungsten magnetic probe.	35

	Page
Figure 21. Experimental SHPM measurement of the output magnetic field vs. DC input current for the tested micro electromagnetic probe.	36
Figure 22. B-H curve of the magnetic probe measured using the scanning Hall probe microscope.	37
Figure 23. Illustration of the synthesis of stable alginate droplets containing magnetic particles. The alginate and magnetic particle solution is put in a syringe pump and applied to a capillary needle that is connected to an electrospray device.	38
Figure 24. Illustration of droplet manipulation with the new electromagnetic probe. In selective droplet capture the cover slip in the figure is kept in place, whereas in non-selective droplet capture and capture-transport experiments the cover slip is removed.	39
Figure 25. Concentration dependent manipulation of alginate droplets.	40
Figure 26. Non-selective droplet manipulation.	41
Figure 27. Droplet capture and transportation.	42
Figure 28. An illustration of the direct “write” of metallic nanostructures using a metal-coated scanning probe.	46
Figure 29. Process flow diagram outlining the fabrication of the scanning probes.	49
Figure 30. Scanning electron micrograph of an array of fabricated scanning probes for the writing experiment: (a) The entire array; (b) Zoom-in view of a probe tip.	50
Figure 31. A scanning electron micrograph showing the existence of a wear scar on the scanning probe tip after writing.	51
Figure 32. Computer images reconstructed from AFM measurement results showing the formation of metallic gold structures as a result of direct “write” on a silicon substrate: (a), (b) AFM images of gold lines (linewidths of ~ 600 nm and ~ 400 nm, respectively); (c) AFM image showing the rare case where dots were formed (diameter ~ 650-900 nm).	52
Figure 33. An illustration of variable-resolution SPL process using an array of both “sharp” and “blunt” probes.	56
Figure 34. Summary of existing micromachining processes to realize “blunt” tips.	56

Figure 35.	An illustration of the controllable process for the formation of variable sized cavities based on bulk micromachining of an SOI wafer.....	57
Figure 36.	Scanning electron micrographs of bulk etched cavities in a {100} SOI substrate. Inset (a) shows the cavity with the largest window opening (20 μm) and a flat square base, whereas inset (j) is the cavity with the smallest window opening (11 μm) and a sharp endpoint, from (a) to (j) window opening decreases by 1 μm in each cavity. Inset (k) and (l) show perspective views of the cavities.	59
Figure 37.	An illustration of the fabrication process for scanning probes with different contact areas. The process flow is divided into three steps: (1) tip formation where variable sized cavities for tip molding are precisely defined, (2) deposition of the desired probe and tip materials, and (3) the probe release by sacrificial layer etching.	61
Figure 38.	An illustration of the top and cross sectional views of an etched cavity. Due to possible rounding of sharp corners during lithography, an undesired overhang of the oxide layer over the silicon cavities is possible. Removal of the oxide layer is necessary to prevent probe lock-in during the release step.	62
Figure 39.	Process flow diagram outlining the maskless photoresist filling of the cavities before oxide removal.	63
Figure 40.	Scanning electron micrograph of photoresist filled cavities using the maskless photoresist filling technique.....	63
Figure 41	Optical microscopic images of fabricated scanning probe arrays: (a) Scanning probe arrays (7 \times 10) on SOI substrate before release; (b) A released scanning probe chip with SU-8 handle; (c) A zoom-in view of the probe array showing the details of the probe tips.	65
Figure 42.	Scanning electron micrographs showing the controllable fabrication of scanning probe tips with precisely defined tip contact area. Inset (a) shows the probe with the bluntest tip, and inset (l) shows the sharpest probe. Insets (b)-(k) show the close-up views of each tip in the fabricated scanning probe chip consisting of 10 cantilevers. The tip contact area decreases from $5.6 \times 5.6 \mu\text{m}^2$ in (b) to $0.8 \times 0.8 \mu\text{m}^2$ in (g) and then remains almost the same through sharper tips $\sim 200 \text{ nm}$ in (h)-(k).	66

	Page
Figure 43. (a) Optical microscopic image of a “blunt” gold probe tip with flat contact area before inking; (b) Fluorescence image of the probe tip after inked with Rhodamine-B dye; (c) Experimental setup employed in patterning experiments.....	69
Figure 44. Rhodamine-B patterns with different linewidths created simultaneously by the gold probe array.	70
Figure 45. Illustration of the applications of colloidal probes: a) Scanning probe lithography; b) Cell studies; and c) Measurement of surface interfacial forces.	72
Figure 46. Existing colloidal probe fabrication methods: a) Microsphere attachment; b) Oxidation of silicon tips; c) Thermal evaporation; d) Chemical etching.	73
Figure 47. Illustration of the mould filling technique for transforming sharp end cavities into curved ones.	75
Figure 48. Scanning electron micrograph showing (a) bulk-etched cavity in silicon with a sharp termination versus cavities with curved, round ending, (b) top view; (c) 65° tilted view of multiple rounded cavities; (d) 65° tilted view of a single round cavity.	75
Figure 49. Fabrication process flow of scanning probes with curved tips.	77
Figure 50. Scanning electron micrographs of a fabricated curved tip probe array.....	78
Figure 51. Scanning electron micrograph showing SPM tips with different radius of curvature where the tip radius of curvature is controlled by changing the solid content (%) or viscosity of the photoresist mould filling material. a) No photoresist filling 0%; b) 7.075 %; c) 14.15 %; d) 21.225 %; e) 28.3 %.	80
Figure 52. Plot of the tip radius of curvature versus photoresist solid concentration.	81
Figure 53. Illustration of the layer-by-layer filling process for controlling the tip radius of curvature.....	82
Figure 54. Scanning electron micrograph showing SPM tips with different radius of curvature where the tip radius of curvature is controlled by spinning multiple layers of photoresist at a fixed solid content (7.075 %). a) 1 time of spinning; b) 2 times; c) 3 times; d) 4 times..	83
Figure 55. Plot of the tip radius of curvature versus number of photoresist spin cycles	84

LIST OF TABLES

	Page
Table 1. Permalloy plating solution composition and electroplating conditions	29
Table 2. Summary of the photoresist concentrations and the dilution amount required in each case	79

CHAPTER I

INTRODUCTION

1.1 Motivation

In everyday life devices are used in the macro scale to interact with and manipulate matter. These devices range from sophisticated machinery to very simple tools (knives, hammers, drills etc.) even our hands that we use everyday to perform basic tasks like picking, moving, rotating, pressing etc.; in short, actuating or manipulating matter. With advancements in semiconductor fabrication technology, similar tools have been developed for application in micro and nano scale systems.

Today, one of the most widely utilized methods to aid research in the field of nanotechnology is through the use of probes that can be used to interact with matter at the micro/nano scale. Probes are of utmost importance for nanosciences since they practically serve as robotic hands that bridge the gap between the macro and the micro/nano domains.

However, so far the most widely used probe topology is simply comprised of a sharp tip used for imaging purposes in scanning probe microscopy (e.g. scanning tunneling microscopy, atomic force microscopy). Just as different tools are made in the macro scale for different purposes, probes could as well be designed for different applications to provide more functionality. Therefore, the present study has focused on developing new micromachined probe topologies for various biological and nanotechnology applications. Probes were investigated under two major categories; 1) Micro Electromagnetic Probes, 2) Scanning Probes. The first two chapters will be dedicated for micro electromagnetic probes and the next three chapters will be discussing scanning probes.

This dissertation follows the style of *Journal of Micromechanics and Microengineering*.

In chapter II, the development, characterization and biological applications of the first MEMS-based micro electromagnetic probe up-to-date is introduced; while chapter III discusses micro electromagnetic probe fabrication using controlled electroplating together with probe application in droplet-based microfluidics.

The work on scanning probes is also twofold. First, to develop new probe fabrication technologies that aim at controlling the tip geometry. Second, to investigate applications of the newly developed probes in areas other than imaging. In chapter IV, scanning probes with uniform tip profile are developed along with a direct writing (patterning) method to generate metallic structures. Chapter V introduces a new micromachining technique to control the probe tip contact area and demonstrates variable resolution scanning probe lithography, while chapter VI discusses the development of curved-tip, “colloidal” scanning probes with controllable tip radius of curvature. Brief summaries of the major points discussed in each chapter are provided below.

1.2 Summary of Works

1.2.1 Chapter II

The design, fabrication and experimental characterization of a new micromachined electromagnetic probe, which can be readily adapted to various biological manipulation and stimulation applications is presented. The micro electromagnetic probe consists of a protruding (out-of-chip), sharp permalloy needle embedded into a three-dimensional gold conducting coil. The probe fabrication is carried out using traditional surface micromachining processes coupled with assembly techniques. This hybrid approach significantly reduces fabrication difficulties and provides a simple and straightforward technique to realize integrated core-coil geometries. Furthermore, by using a scanning Hall probe microscope (SHPM), a comprehensive, high-spatial resolution characterization of the probe performance (e.g. peak magnetic intensity and spatial field distribution) is achieved for the first time. The

manipulation of sub-micron sized magnetic particles with the developed micro electromagnetic probe is also demonstrated.

1.2.2 Chapter III

This section presents the magnetic manipulation of biocompatible droplets using a probe-based approach. First, a simple method for developing magnetic probes capable of localized magnetic field delivery is described; this capability is important for precise manipulation. The fabrication of magnetic probes involves controlled electroplating of permalloy ($\text{Ni}_{80}\text{Fe}_{20}$) on commercially available tungsten needles with tip radii as small as $0.5\ \mu\text{m}$. Experimental validation of probe functionality is achieved by characterizing the magnetic response of the probe with a highly sensitive scanning Hall probe system. The magnetic probe is then employed in manipulating biocompatible alginate micro droplets with encapsulated magnetic particles. The synthesis of the droplets was conducted in-house and droplets of different sizes and magnetic particle concentrations were obtained for use in manipulation experiments. Multiple experiments were done to demonstrate the efficacy of the developed probe in manipulating droplets, which is crucial for constructing droplet-based microfluidic systems.

1.2.3 Chapter IV

This chapter discusses the fabrication and application of new gold coated scanning probes for direct “write” of sub-micron metallic structures. The scanning probe consists of a base structure made of silicon nitride and a thin gold coating. The tip profile and radius of curvature is tightly controlled in the probe fabrication to ensure a predictable tip-substrate contact. By scanning a fabricated probe on a single crystal silicon surface in ambient environment, sub-micron gold lines were formed as a result of direct gold material transfer from scanning probe tip onto silicon surface, which is believed to be induced by the friction and wear associated with the probe scanning.

1.2.4 Chapter V

This section describes a novel micromachining technique for batch fabrication of scanning probe arrays with different tip contact areas. Based on the bulk micromachining of SOI (silicon-on-insulator) substrates, it eliminates the need for time-dependent etching processes and thus is capable of simultaneously fabricating both “sharp” and “blunt” scanning probes with precisely defined tip contact areas in a controllable and repeatable manner. As an example of the application of this probe fabrication technique, prototype scanning probe arrays have been successfully fabricated and used to demonstrate variable-resolution scanning probe lithography (SPL) of fluorescent dyes in a parallel mode.

1.2.5 Chapter VI

This chapter reports the first batch-fabrication method to create colloidal scanning probes based on standard micromachining processes. Microfabrication of colloidal probe arrays having smooth surface profile with radius of curvature ranging from nanometers to tens of microns is successfully demonstrated. A new mould filling technology is developed where bulk-etched cavities with sharp endpoints are transformed into cavities with curved endings via spin coating of a liquid filling material (photoresist). The curved profile is then replicated into a stable metallic mould by evaporating a layer of aluminum, after which mould-transfer SP fabrication is conducted to create colloidal probes. Two fabrication control knobs were developed and characterized for accurate control of the tip radius of curvature. By adjusting the solid content and number of spins of the filling material different mould profiles and thereby tip radii of curvature was achieved. The new controllable technology allows rapid microfabrication of colloidal scanning probes with different tip radii of curvature which will be useful for many biological and nanotechnology applications.

CHAPTER II

MEMS-BASED MICRO ELECTROMAGNETIC PROBE FOR BIOLOGICAL MANIPULATION AND STIMULATION

2.1 Introduction

Today, the use of static or time-varying magnetic fields has attracted considerable attention in both *in-vivo* and *in-vitro* biomedical studies. For example, static or quasi-static magnetic fields have been widely used to achieve efficient manipulation and sorting of micro scale particles or biomolecules in “lab-on-a-chip” applications [1-9]. In neuroscience, human cranial stimulation with time-varying magnetic fields has been investigated to serve as a possible non-invasive therapy for certain psychological disorders, such as depression [10-12]. Recent studies have also shown that low-field magnetic stimulation (LFMS) of intensity less than 10 Gauss could change receptor binding parameters in brain membranes [13, 14] and produce antidepressant-like effects [15,16]. However, the exact cellular mechanism behind the magnetic neural stimulation method is not well understood and requires further investigation in a more quantitative way [11, 14-18].

For the above applications, a localized, concentrated and spatially reconfigurable magnetic field is necessary to achieve precise and selective manipulation or stimulation in a controllable manner [2, 19]. Such magnetic fields could be achieved by using a micro electromagnetic probe consisting of a solenoid conducting coil for magnetic field generation and a protruding magnetic core with a sharp tip for magnetic field concentration [20, 21]. Once fabricated, the micro electromagnetic probe can be readily used with a micro manipulator to deliver localized magnetic field at any location where it is needed, while the intensity and frequency of the magnetic field can be easily adjusted by changing the input driving current.

However, several technical challenges still remain in the development of micro scale electromagnetic probes. First, due to its small size and complex three-dimensional (3D) structure, the probe fabrication turns out to be complicated and difficult to

implement. Recently, significant progress has been made in microfabrication and micromachining technologies. However, their capability for creating either 3D or protruding microstructures is still limited. To fabricate the 3D conducting coil, complex fabrication steps involving thick photoresist processing [22] or repeated lithography and electroplating have to be used [23, 24]. To form the protruding magnetic core, either dry or wet bulk etching is necessary to remove the substrate material underneath, which would involve harsh chemicals and etching conditions, causing material compatibility issues.

Second, due to the small range and large gradient of the generated magnetic field, it is very difficult to achieve a good experimental characterization of the performance of the electromagnetic probe. Conventional magnetic field measurement tools, such as a Gauss meter, cannot provide the needed spatial resolution and sensitivity for such characterization. As a result, so far the design of micro electromagnetic devices has largely relied on numerical simulation and modeling. Recently, scanning techniques coupled with Hall magnetic sensing devices were employed for the characterization of stray magnetic field emanating from magnetic force microscope tips [25]. Equipped with a Hall probe (with a small sensing aperture) and a high resolution piezoelectric stage, a scanning Hall probe microscope (SHPM) system can achieve the needed sensitivity and spatial resolution for micro scale magnetic field measurement [26], and thus could be adapted to the experimental characterization of micro electromagnetic probes.

This chapter reports the design, fabrication and experimental characterization of a new micromachined electromagnetic probe. First, by combining surface micromachining and guided micro assembly, the fabrication of the electromagnetic probe has been realized with a simple and straightforward process. Next, by capitalizing upon the recent progress in SHPM a comprehensive experimental characterization of the probe performance (e.g. peak magnetic intensity, spatial field distribution, etc.) is successfully achieved. To our knowledge, this is the first one of such experiments conducted up to date. The high-spatial-resolution SHPM measurement reveals the

minute details of the micro scale magnetic field generated by the electromagnetic probe and thus is capable of providing critical information for the design, evaluation and optimization of micromachined electromagnetic probes. Finally, manipulation of fluorescent dye labeled magnetic particles is also tested as an example to demonstrate the functioning of the developed probe.

2.2 Device Design and Simulation

Figure 1 shows a schematic of the micro electromagnetic probe to be developed. It consists of a supporting substrate, a 3D gold coil and a protruding (Permalloy) magnetic core with a sharp tip. To conduct magnetic manipulation, a magnetic particle is attached to the biological sample, which is exposed to the magnetic field (\mathbf{B}) created by the micro electromagnetic probe. Suppose the magnetic particle has a total magnetic moment of \mathbf{m} , the magnetic force acting on the particle (which can be considered as a magnetic dipole) can be determined by,

$$\mathbf{F} = \nabla(\mathbf{m} \cdot \mathbf{B}) \quad (1)$$

Here, the total magnetic moment \mathbf{m} can be expressed as,

$$\mathbf{m} = V\chi_m \mathbf{B} / \mu_0 \quad (2)$$

Where χ_m is the volumetric magnetic susceptibility, and V is the volume of the particle [27-29]. Due to the probe geometry, the major component of the magnetization of the magnetic core and thus the magnetic flux from the probe tip will align with the probe axis. Labeling this component of the magnetic flux density as \mathbf{B}_z , equation (1) can be rewritten as:

$$\mathbf{F} = m_z \frac{\partial \mathbf{B}_z}{\partial z} = \frac{V\chi_m}{\mu_0} \left(\mathbf{B}_z \frac{\partial \mathbf{B}_z}{\partial z} \right) \quad (3)$$

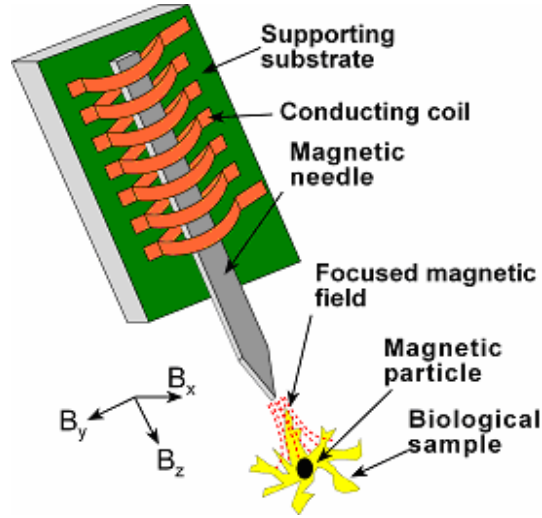


Figure 1. Schematic of the micro electromagnetic probe to be developed. It consists of a supporting substrate, a solenoid conducting coil and a protruding (permalloy) magnetic core with a sharp tip.

According to equation 3, the force on a magnetic particle will depend on the volume of the magnetic particle, magnetic susceptibility of the particle material, magnetic flux density, and the gradient of the magnetic flux density. Among these parameters, there is little control on the volume and magnetic susceptibility. The volume of the particles and their magnetic susceptibility are usually small in micro manipulation applications. Therefore, as a main design consideration, the product of the gradient of the magnetic flux density and the magnetic flux density ($B_z \frac{\partial B_z}{\partial z}$) should be maximized in order to generate appreciable levels of force or create highly localized magnetic fields which are important for selective manipulation and stimulation.

Since the gradient of the magnetic flux near the probe tip is largely affected by the probe tip profile, the magnetic field generation from different probe tip profiles was simulated using Maxwell 3D[®] electromagnetic design software. The magnetic properties of the permalloy core obtained from [30] were used in the simulation. To simplify the simulation process, the magnetic field generated by the conducting coil was

represented with a uniform magnetic field parallel to the axis of the permalloy core. Different strength of external magnetic field was applied and the magnetization of the permalloy core was found to be saturated at ~ 0.85 T when an external field of 2150 A/m is applied. This field value (2150 A/m) was then imposed as a boundary condition in all the simulations to determine the maximum capability of field generation of different probe designs. Figures 2(a) and (b) show the magnetic field distribution directly below the probe tips, for two different tip profiles having a taper angle (α) of $\sim 15.2^\circ$ and $\sim 43.6^\circ$ respectively. It is clear that smaller taper angle is more effective in creating a higher field concentration. Figure 2(c) shows the magnetic field distribution for a probe consisting of multiple tips, which indicates that this feature could be used to provide extra flexibility in controlling the magnetic field distribution. Figure 2(d) shows the field versus distance plot in log scale obtained for a probe design with (α) $\sim 15.2^\circ$.

It is seen that, the bulk permalloy core region represented by the origin of the log-log plot, reaches the saturation value of ~ 0.85 T with the externally applied field of 2150 A/m. Then, during the transition from the permalloy core to air boundary, the magnetic field starts straying from the tip and due to the difference in relative permeabilities of the two medium, an immediate fall in the magnetic field (within a distance of about 100 nm.) is observed. Moving further away from the probe tip causes the magnetic field to fall to a level of ~ 30 mT. within 20 microns from the probe tip. Based on these results, the gradient of the magnetic flux density was calculated to be on the order of 10^3 T/m which confirms the capability of the proposed device structure to generate large field gradients.

2.3 Device Fabrication

To achieve a simple and straightforward probe fabrication, a hybrid fabrication process involving surface micromachining and guided assembly has been developed, which consists of the three following steps: 1) fabrication of the probe substrates with bottom conductors of the conducting coil; 2) fabrication of the magnetic cores; and 3) assembly of the magnetic core and top conductors of the conducting coil (figure 3).

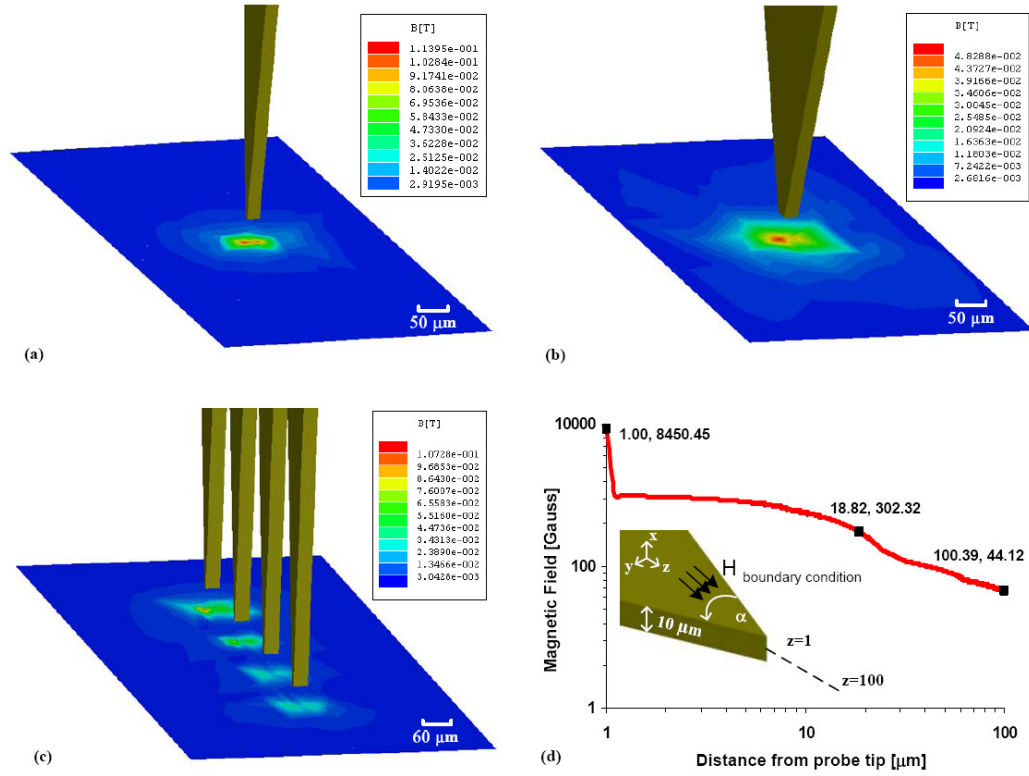


Figure 2. Simulated magnetic field distribution of different probe tip designs: (a) Field distribution of a probe tip with a taper angle of 15.2° ; (b) Field distribution of a probe tip with a taper angle of 43.6° ; (c) Field distribution of a four-tip design; (d) Line plot in log-log scale showing the rapid fall of the magnetic field with respect to distance from the probe tip for a probe design with taper angle 15.2° , shown in the inset is a pictorial representation of the simulation conditions.

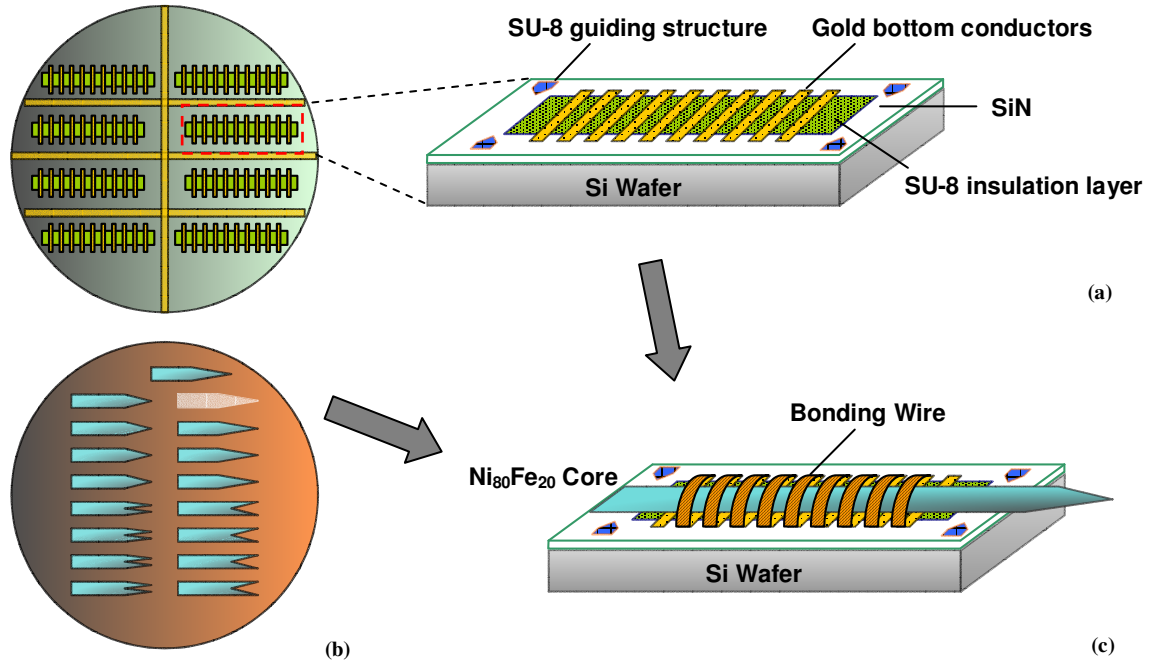


Figure 3. An illustration of the fabrication process of the micro electromagnetic probe: (a) Fabrication of gold bottom conductors and SU-8 insulation and guiding structures; (b) Fabrication of the permalloy magnetic cores; (c) Assembly of the magnetic core on the chip and placement of the top conductors with wire bonding.

1) To fabricate the probe substrate with bottom conductors, a layer of chromium (10 nm thick) and gold (300 nm thick) is deposited onto a nitride coated silicon wafer. Gold electroplating with AZ4620 photoresist mold and a subsequent etching of the chromium/gold layer are carried out to form the bottom conductors (10 μm thick) of the three-dimensional gold conducting coil. An SU-8 resist layer (10 μm thick) is patterned to provide electrical isolation between the bottom conductor and the magnetic core (to be assembled in Step 3). A second SU-8 layer (50 μm thick) is patterned to form the guiding structures for the assembly of the magnetic core. After the fabrication, the silicon wafer (with different coil designs) is cut into individual dies for subsequent probe assembly (figure 3(a)).

2) To fabricate the magnetic core, first a seed layer of chromium (10 nm thick)/copper (300 nm thick) is deposited onto a separate silicon wafer. Permalloy ($\text{Ni}_{80}\text{Fe}_{20}$) electroplating with AZ4620 photoresist mold is then conducted to form the magnetic core (10 μm thick) of the probe. Once the plating is complete, the AZ4620 mold is completely removed, which is followed by the patterning of an AZ5214 photoresist layer onto each of the permalloy cores to serve as an insulating layer between the top conductors and the core. Next, electroplated permalloy cores (with different designs) are released by sacrificial etching of the chromium /copper layer. The micro electromagnetic probe can assume different tip profiles defined by photolithography. This allows the controllable generation of various spatial field distributions for different applications (figure 3(b)).

3) To assemble the entire probe, an electroplated permalloy core is placed and bonded onto the fabricated silicon chip. The top conductors are placed by conducting gold wire bonding to form a complete 3D conducting coil (figure 3(c)). For wire bonding, a suitable wire, which allows a large processing window and operating parameters, was selected. Gold bonding wire of 1 mil (25 μm) in diameter was used, which is suitable for both wedge and ball bonding and at the same time can provide low loop heights desirable for ideal solenoid formation (Kulicke & Soffa, AW-14 Gold Bonding Wire for Universal Use).

Different conducting coils (width, length and number of turns) and probe tip profiles have been designed and fabricated. The developed fabrication process circumvents the difficulties faced in the direct microfabrication of the 3D conducting coil and the protruding magnetic core, and thus results in a simple and straightforward process. It also offers extra flexibility by allowing the assembly of any combination of conducting coil and magnetic core. The scanning electron micrograph of a fabricated probe is shown in figure 4(a). The solenoid consists of 13 turns which span a region of 1.85 mm. The magnetic core has a width of 400 μm , total shank length of 4.75 mm and a tapered extension of 1.5 mm. The probe tip has a taper angle of 15.2° . Figure 4(b)

shows other fabricated permalloy cores with alternative tip profiles, which could be used for different applications.

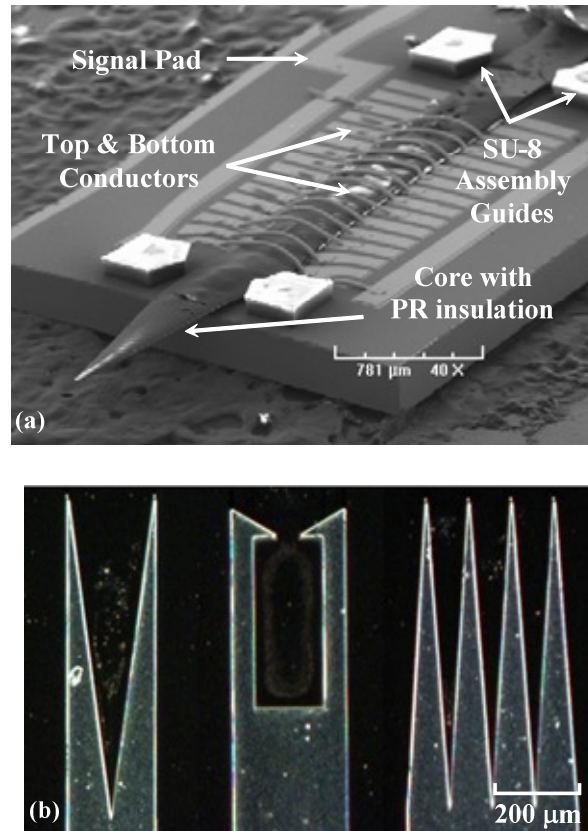


Figure 4. (a) Scanning electron micrograph of a fabricated micro electromagnetic probe; (b) Optical microscopy pictures of permalloy magnetic cores with different tip profiles.

2.4 Experimental Characterization

The experimental characterization of the micro electromagnetic probe is achieved using an SHPM system (NanoMagnetics Instruments Ltd.). The experimental test setup depicted in figure 5 shows the SHPM stage and the probe assembly designed to enable efficient testing. The micro electromagnetic probe is attached to a larger copper plate,

which facilitates both probe handling and allows rapid dissipation of the heat generated during probe operation.

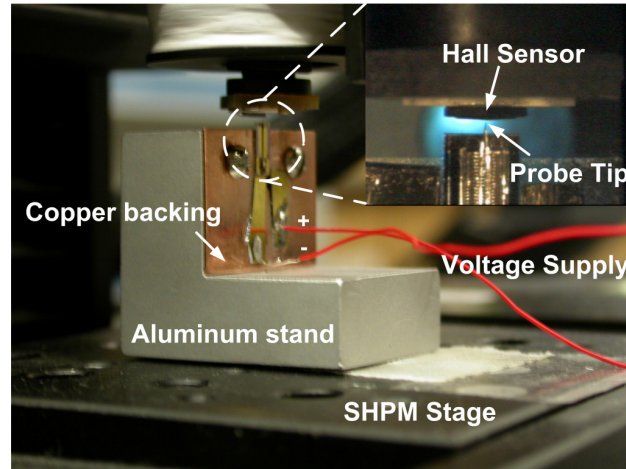


Figure 5. Scanning Hall probe microscope setup for micro electromagnetic probe characterization. The gap between the probe tip and Hall sensor is estimated to be $\sim 20 \mu\text{m}$.

To obtain the temperature distribution on the probe, ANSYS finite element analysis software was used. The plot of the temperature distribution in figure 6(a) indicates that in the case of 300 mA input current to the conducting coil, the maximum temperature on the micro electromagnetic probe is 49°C , which occurs around the connection points of the bottom and top layer conductors. On the other hand, the maximum temperature on the micro electromagnetic probe tip is 39°C . Simulations under different input currents were carried out to characterize the effect of input current on the probe temperature. Plot of the tip temperature under different input currents indicates an increasing tip temperature with higher current levels (figure 6(b)). This heat sink mechanism ensures that the permalloy magnetic cores do not show significant displacement during probe operation, allowing proper testing conditions during characterization experiments and actual operation of the probe in biological applications. The copper plate housing the micro electromagnetic probe is attached to an aluminum

stand which allows the probe tip to be easily positioned and aligned perpendicular to the Hall sensor.

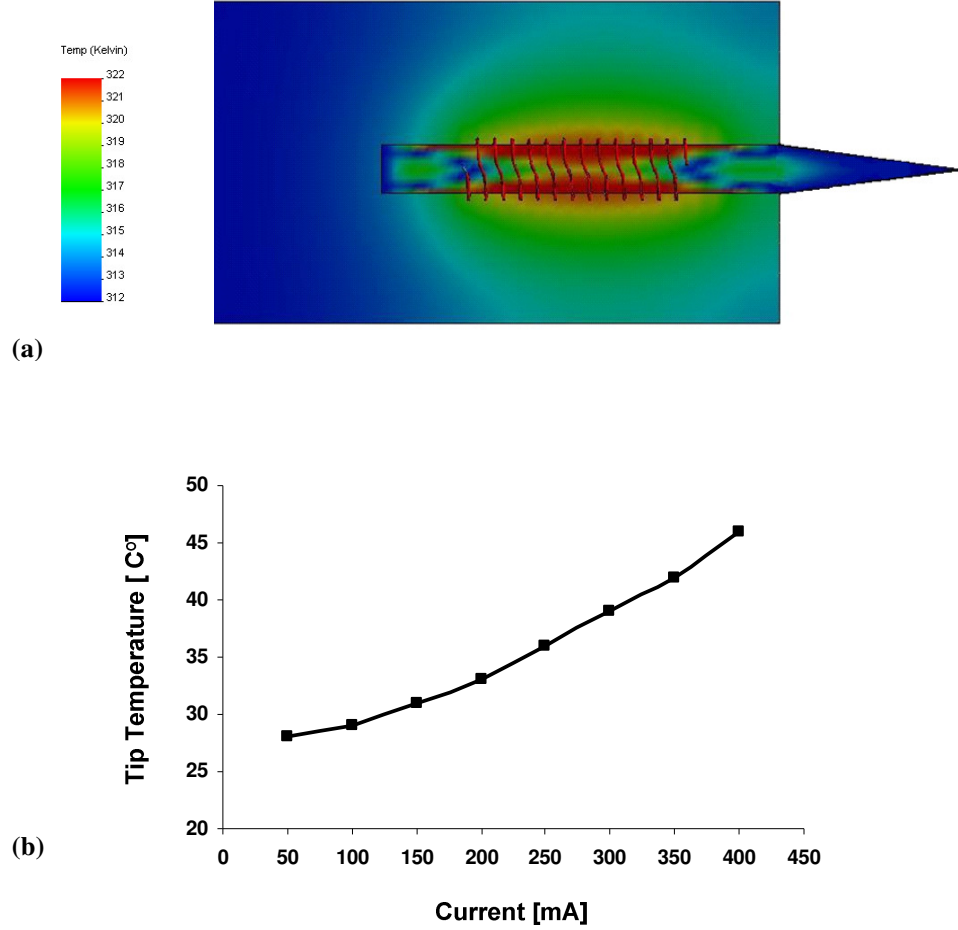


Figure 6. (a) Finite element simulation showing the temperature distribution on the micro electromagnetic probe under 300 mA input current; (b) Plot of the probe tip temperature under different input current levels.

The SHPM is equipped with a Hall sensor probe with a very small sensing aperture (less than $1 \times 1 \mu\text{m}^2$) to significantly reduce possible averaging effects in the measurement of the magnetic field. The scanning of the Hall sensor probe is performed by a piezoelectric crystal. The small sensing aperture coupled with the fine scanning

step size (100 nm) ensures a high spatial resolution necessary for the probe characterization. To avoid possible collision damage to the Hall sensor, a small gap ($\sim 20\ \mu\text{m}$) is maintained between the Hall sensor element and the probe tip. It should be noted that under this experimental setup, the Hall sensor probe mainly picks up the magnetic field component parallel to the probe axis (corresponding to B_z in figure 1). However, this should not be a big concern in our experiments since B_z is the component of the magnetic field which contributes most to the magnetic manipulation and stimulation of micro scale objects with micro electromagnetic probes.

Before the measurement, the micro electromagnetic probe tip is first demagnetized using the built-in coil of the SHPM by applying an exponentially decaying sinusoidal magnetic field with alternating polarity to the axis of the magnetic core. After the demagnetization, the tip of the micro electromagnetic probe is aligned to the Hall sensor and the peak output magnetic field density (B) as a function of the input current (I) is measured. As shown in figure 7, the output magnetic field density (B) first increases linearly as a function of the input current (I) and then saturates around 300 Gauss (30 mT), which is due to the expected ferromagnetic behavior of the core material. Next, the B-H curve of the permalloy core is obtained, which also reveals a characteristic hysteresis behavior figure 8. It should be noted that the measured saturation intensity of 300 Gauss is much lower than the saturation magnetization of permalloy (~ 0.9 Tesla) widely reported in literature [30]. This is because the Hall sensor is positioned around $20\ \mu\text{m}$ away from the probe tip. Due to its large gradient, the magnetic field of the probe will quickly diminish at locations farther away from the probe tip. In many biological applications, the samples usually have to be placed at a small distance away from the probe tip. Therefore, our measurement setup and results are valid and useful in assessing the actual magnetic field that will be experienced by the biological samples since they reflect the real working condition of the probes.

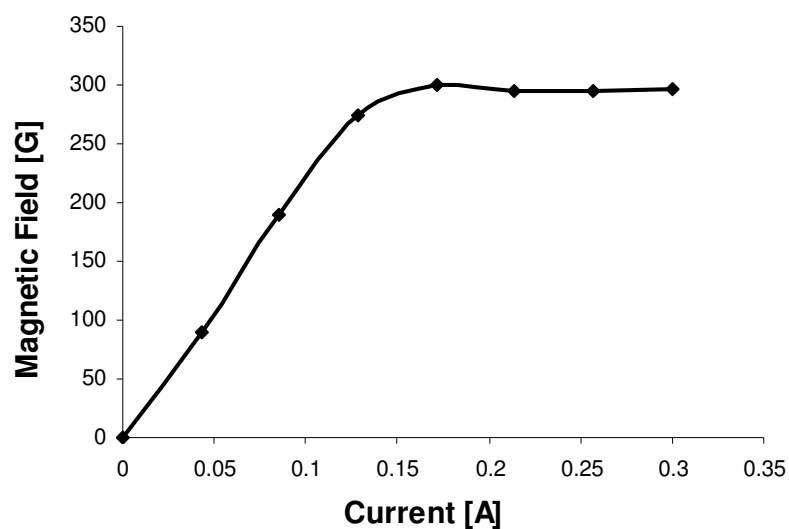


Figure 7. Magnetic field output 20 μm from the tip of the tested micro electromagnetic probe as a function of input current.

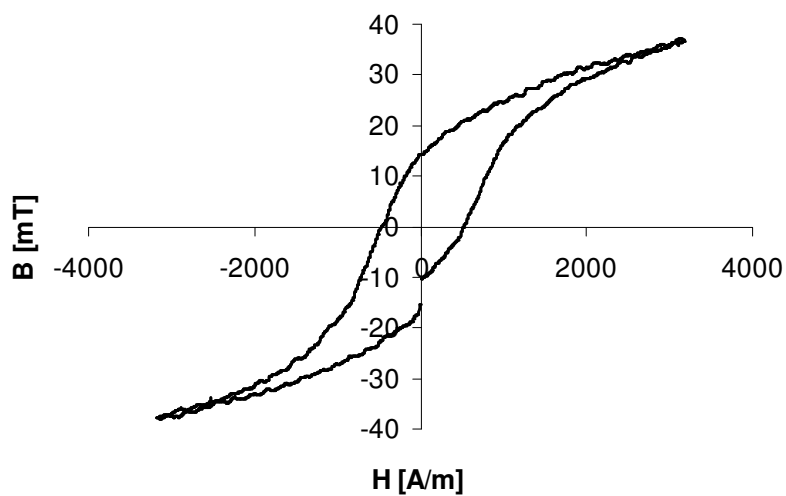


Figure 8. The B-H curve of the permalloy magnetic core characterized by the scanning Hall probe microscope located about 20 μm from the tip of the core.

In order to obtain the spatial distribution of the magnetic field, the Hall sensor probe is scanned across an area of $25 \times 25 \mu\text{m}^2$ around the probe tip, while maintaining the gap between the probe tip and the Hall sensor. Figure 9 shows both the axial and the 3D surface plot of the magnetic field distribution when an input current of 300 mA is applied. The field drops rapidly to half of its peak value (297.2 Gauss) within a distance of $4 \mu\text{m}$ and to a few gauss within a distance of about $12 \mu\text{m}$. This translates into large field gradients ($\partial B_z / \partial x = 2768 \text{ T/m}$ and $\partial B_z / \partial y = 2531 \text{ T/m}$) suitable for biological applications which require site-specific field delivery [1, 7, 9, 28]. On the other hand, the gradient term ($\partial B_z / \partial z$) important for force generation (equation 3) can be found by measuring the magnetic field at two different Hall sensor to probe tip separations. Using this approach, $\partial B_z / \partial z$ was calculated to be 2484 T/m , which is similar to the two other gradient components of B_z . This result indicates that the straying of the magnetic field component B_z is almost symmetrical in all three axis.

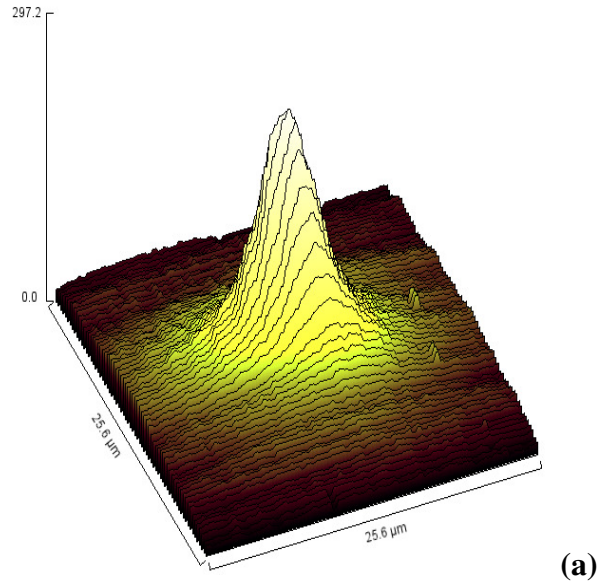
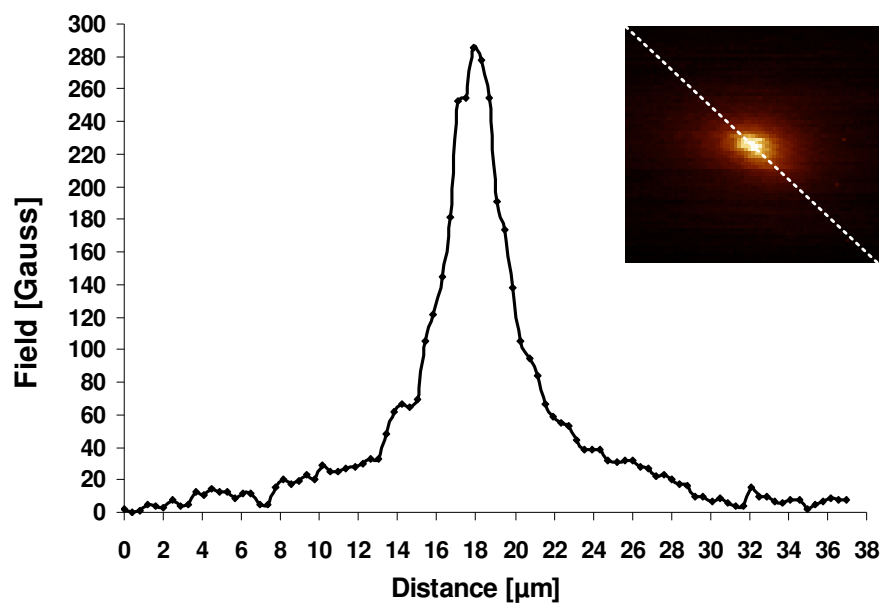
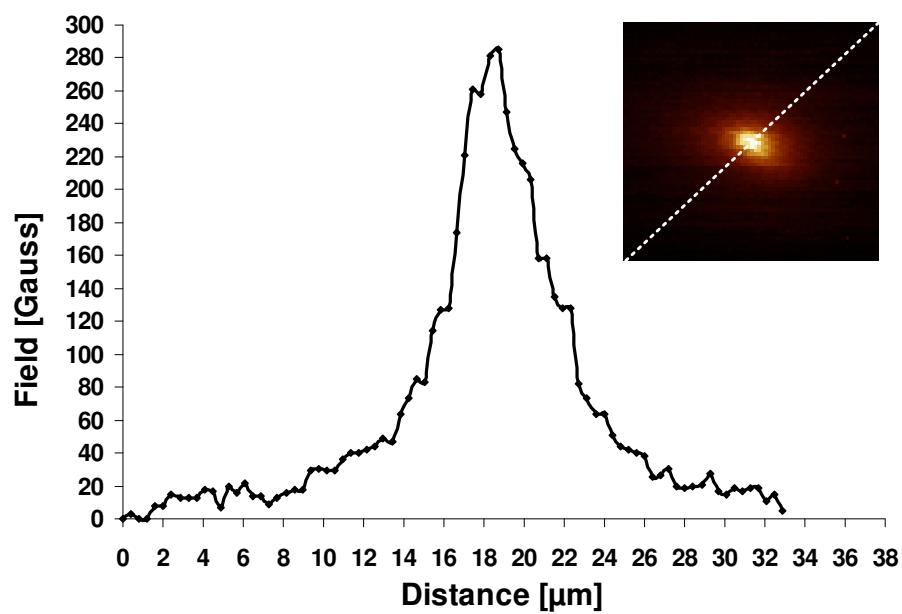


Figure 9. Measured spatial distribution of the magnetic field output (the component parallel to the axis of the probe) with an input current of 300 mA: (a) surface plot; (b) and (c) axial field plots along the diagonals of the probe tip obtained from the cross-sectional field distribution.



(b)



(c)

Figure 9. Continued.

During experimental characterizations, it was found out that the spatial distribution of the magnetic field is extremely sensitive to the actual profile of the probe tip, which inevitably is different from the design due to imperfections in probe fabrication. This indicates that in applications where an accurate mapping of field distribution is critical, a good experimental characterization is indispensable.

2.5 Magnetic Particle Manipulation

The fabricated micro electromagnetic probe was tested to manipulate fluorescent superparamagnetic particles, which contain 63.4% magnetite and have a spherical shape with mean diameter of 0.9 μm (Bangs Laboratories). Using the values measured with the SHPM for the maximum magnetic field intensity and gradient, and with the magnetic particle susceptibility value (χ_m) of 1.539, forces on the order of several pico newtons (34.52 pN) can be exerted on magnetic particles, and particle manipulation can be achieved. For the manipulation experiments, in order to avoid rapid evaporation of the water based magnetic particle solution during testing, it was first mixed with glycerol and then a small drop of the mixture was applied on a microscope cover slide. Next, the micro electromagnetic probe with the copper backing is attached to a micro-positioning stage at angle of 40° with the vertical direction.

Manipulation of the magnetic particles was observed under a confocal microscope with 63× immersion lens. Figure 10(a) shows the fluorescent magnetic particles at their equilibrium position when the probe was kept above the particle solution with no input current. Figures 10(b) and 10(c) show the gradual attraction of magnetic particles towards the probe tip after the probe is lowered down using a micro-positioner to contact the liquid surface and an input current of 300 mA is supplied.

In a second experiment, a magnetic particle agglomerate was manipulated to show the capability of moving larger objects in liquid solutions. This capability is important for the manipulation of actual biological entities, such as cells and DNA labeled with magnetic particles [31]. As shown in figure 11, initially the probe is off and the particle agglomerate is at rest. When, the probe is turned on with 300 mA input

current, the object moves steadily towards the probe tip and is captured within 4 seconds.

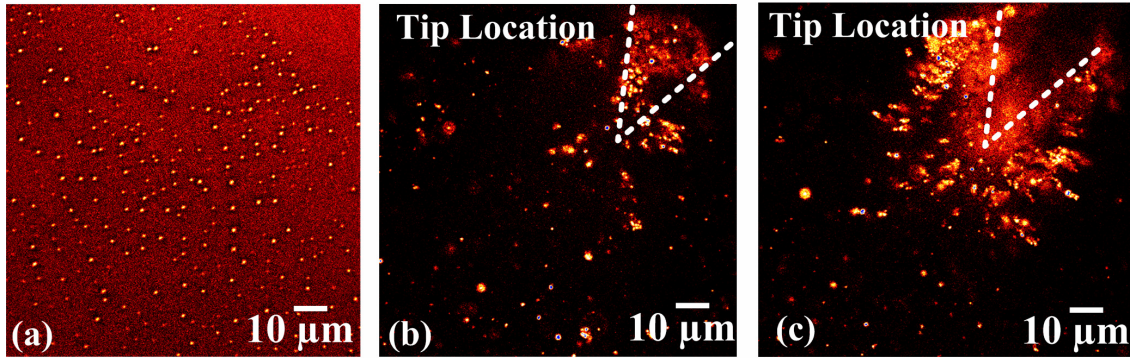


Figure 10. Manipulation of fluorescent magnetic particles using the developed electromagnetic probe (observed under a fluorescence microscope): (a) Magnetic particles stay in their equilibrium position; (b) and (c) After the probe is turned on, magnetic particles move steadily towards the probe tip.

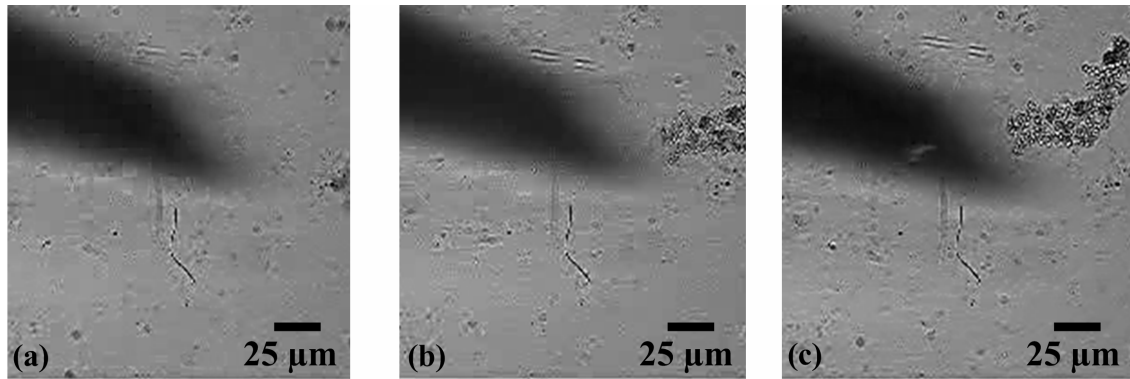


Figure 11. Manipulation of magnetic particle agglomerate: (a) At $t = 0\ \text{s}$, magnetic field is applied; (b) At $t = 2\ \text{s}$, magnetic agglomerate moves toward the probe tip; (c) At $t = 4\ \text{s}$, magnetic agglomerate is captured.

2.6 Discussion and Conclusions

The design, fabrication and experimental characterization of a new micro electromagnetic probe were demonstrated. By combining surface micromachining and guided assembly to circumvent some of the fundamental challenges in current micromachining technology, a simple, straightforward and versatile probe fabrication has been achieved. With the assistance of the newly-developed robotic systems (e.g. Zyvex[®] Microgripper system) to perform automated micro manipulation and assembly, an efficient mass production of the micro electromagnetic probes is also possible.

By using an SHPM with high spatial resolution and field sensitivity, a comprehensive experimental characterization of the fabricated probes has been successfully conducted. The experimental measurement technique presented herein allowed real time measurement of magnetic phenomena at the micro scale and provided a venue to evaluate the probe performance for optimized design and application. Results indicate that, further improvement on the probe performance can be achieved through optimizations in the core geometry. For example, fabricating magnetic cores with sharper tips will increase the flux concentration (i.e. magnetic flux density or induction) thereby allowing a higher localization of the field. This can be achieved by using high resolution pattern generation (e.g. electron beam lithography) or by further sharpening the tips, e.g. with focused ion beam (FIB) etching techniques.

CHAPTER III

PERMALLOY-COATED TUNGSTEN MICRO ELECTROMAGNETIC PROBE FOR MICRO DROPLET MANIPULATION

3.1 Introduction

Recently, there has been significant effort in developing droplet-based microfluidic systems, in which micro scale droplets instead of continuous fluids are manipulated to achieve accurate handling of very small amount of liquid [32-39]. For manipulation of droplets, different methods based on optical, electrical, mechanical and magnetic principles have been investigated [40]. Among these methods, magnetic manipulation is of particular interest due to a number of unique advantages, including “remote” actuation, ability to provide relatively large and long-range forces, being independent of surface charges and dielectric properties of the surrounding environment [41-43]. To achieve magnetic manipulation of droplets in a controllable manner, localized and spatially reconfigurable magnetic fields are necessary. In the past few years, on-chip magnetic fluidic interface devices have been investigated and demonstrated, which consist of one-dimensional or two-dimensional arrays of individually addressable planar inductive coils or electromagnets [1, 2, 6, 7, 44, 45]. When turned on, each micro magnetic device can generate a local magnetic field peak. Different routes (in discrete steps) of particle manipulation could be achieved by “pre-programming” the set of planar coils in the array to be activated. However, the development of these magnetic fluidic interface devices requires complex processes, dedicated microfabrication tools and expertise. Moreover, their reconfigurability is largely limited by the fact that little modification can be made in device layout and structure once they are fabricated.

In addition to the magnetic fluidic interface devices, highly localized and concentrated magnetic fields could be also generated using a micro electromagnetic probe, which consists of a solenoid conducting coil for magnetic field generation and a protruding magnetic core with a sharp tip for magnetic field concentration [46]. When

equipped with a suitable micromanipulator, the micro electromagnetic probe can deliver localized magnetic fields at any location, providing great flexibility in configuring the manipulation route (figure 12).

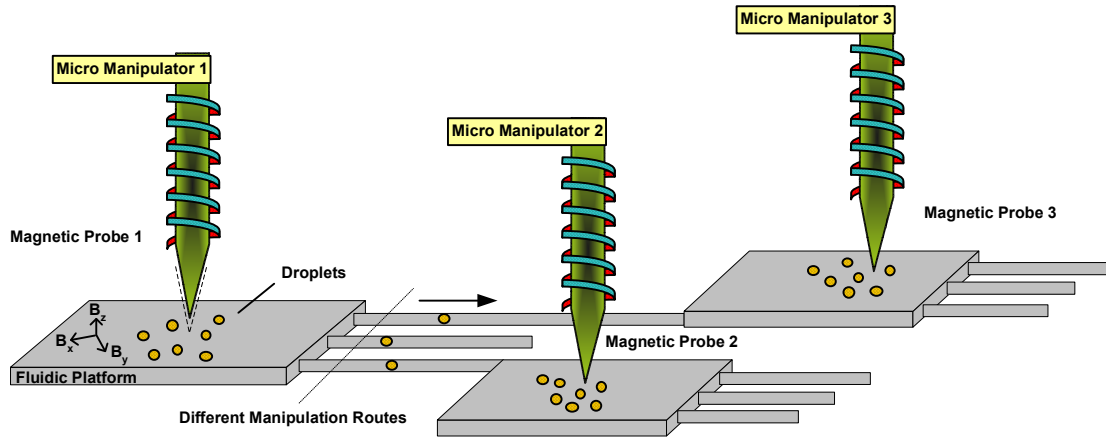


Figure 12. Schematic diagram of probe-based manipulation of droplets. The use of multiple magnetic probes and micromanipulators allows complex droplet manipulation.

However, technical issues still remain in the development of micro scale electromagnetic probes. While MEMS (Microelectromechanical systems) techniques can be employed, traditional fabrication methods turn out to be quite challenging due to small size and complex three-dimensional (3D) structure of the probe [22-24]. In addition, other non-MEMS based methods (e.g. electrochemical sharpening of magnetic wires) are also rather complex and hardly repeatable. Therefore, alternative approaches to achieve a simple and straightforward probe fabrication for rapid manufacturing and immediate use in a basic lab setting are sought.

In this chapter, the development of a new micro electromagnetic probe and its application in the manipulation of micro encapsulated droplets is presented. The micro electromagnetic probe consists of a permalloy-coated tungsten needle as the magnetic core, and a conducting coil made of copper wires. The innovative aspect of this new electromagnetic probe is that it can be readily fabricated in a typical laboratory setting

without involving expensive microfabrication facilities, which results in a straightforward and low-cost fabrication. Meanwhile, the hybrid structure of the magnetic core provides not only the necessary magnetic property, but also increased mechanical robustness, resulting in improved performance of the electromagnetic probe. The developed magnetic probe is shown to be a versatile actuator for droplet-based microfluidic systems through successful demonstrations of manipulation experiments conducted on biocompatible alginate droplets with encapsulated magnetic particles.

3.2 Probe Development

3.2.1 Design and Simulation

Effective and efficient magnetic manipulation of droplets requires an electromagnetic probe with the capability to generate spatially localized and concentrated magnetic field, which can be readily turned on and off to start and stop the manipulation at will. This requirement can be met by using a magnetic core with a sharp tip, which is made of soft ferromagnetic material with low remnant magnetization, such as permalloy. Previously, permalloy needle made of electrochemically sharpened wires [20, 21] or on-chip electromagnetic devices were developed and used to manipulate magnetic particles. However, these fabrication techniques require special processes or microfabrication tools. Moreover, since permalloy is not a hard material, the sharp tip of the permalloy needle can be easily bent or damaged when bumping into a hard object, causing instability and repeatability issues (with altered magnetic field). To address this problem, a new hybrid magnetic core structure consisting of a sharp tungsten needle with electroplated permalloy coating was developed (figure 13).

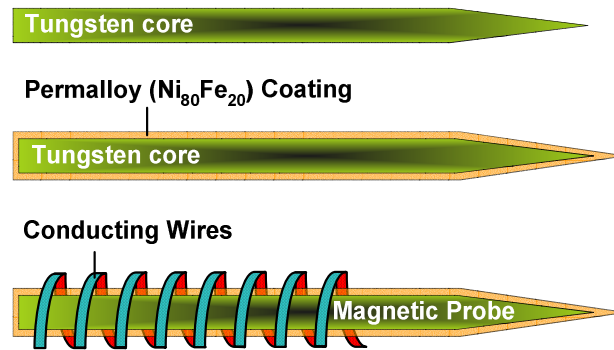


Figure 13. Schematic design of the new electromagnetic probe with a hybrid magnetic core.

Due to their superior mechanical properties and ease of fabrication, sharp tungsten needles with different tip geometries are commercially available and widely used for electrical testing in many applications ranging from integrated circuits to biological samples. By using a sharpened tungsten needle as a “mold” for permalloy deposition with suitable thickness and profile, a hybrid magnetic core with desirable magnetic properties and improved mechanical stability could be obtained without involving special microfabrication processes and tools.

For magnetic field generation and control, a conducting coil wound around the magnetic core can be used to supply a magnetizing field (H), which in turn produces a magnetic induction (B) in the permalloy core. To achieve maximum field generation, a magnetizing field value of 2150 A/m (~ 27 Oe) is necessary to drive the permalloy core into saturation [30]. For a solenoid structure, the field (H) that can be produced is directly related to its turn density (number of turns in a given length) and the applied current, which are both dependent on the wire diameter of the conducting coil. To maximize the range of applicable input currents for tuning the output magnetic field, the wire diameter of the conducting coil needs to be optimized to balance the trade-off between the turn density and current handling capability of the conducting coil. Based on ideal solenoid assumption, a coil with turn density of 10 (turns/mm) and input current of 0.3-0.4 A is expected to generate necessary magnetizing field to saturate the

permalloy core [47]. In the design of the electromagnetic probe, we chose gauge 38 (diameter $\sim 101.6 \mu\text{m}$) copper magnet wire, which is capable of handling the specified current levels and also provide the necessary turn density.

To verify the magnetic field generation and concentration capability of the hybrid magnetic core, electromagnetic simulations were conducted using Maxwell 3D[®] electromagnetic design software. Different profiles of the tungsten core and thickness of the permalloy coating were simulated and compared. To simplify the simulation process, the magnetic field generated by the conducting coil was represented as a uniform field parallel to the axis of the core structure. Different strengths of magnetizing field were applied and the magnetization of the core was found to be saturated at $\sim 0.85 \text{ T}$ at field strength of 2150 A/m . Figure 14(a) shows the magnetic field distribution at the (x-y) plane directly below the probe tip. The maximum field generated at the tip is $\sim 867 \text{ Gauss}$, and the peak magnetic field is localized within $10 \mu\text{m}$. The line plot figure 14(b) shows the field distribution starting on a point on the probe, and then moving into the air region and extending $100 \mu\text{m}$ away from the probe tip. These results indicate that the hybrid magnetic core has the capability to produce magnetic fields of suitable magnitude and concentration to conduct droplet manipulation.

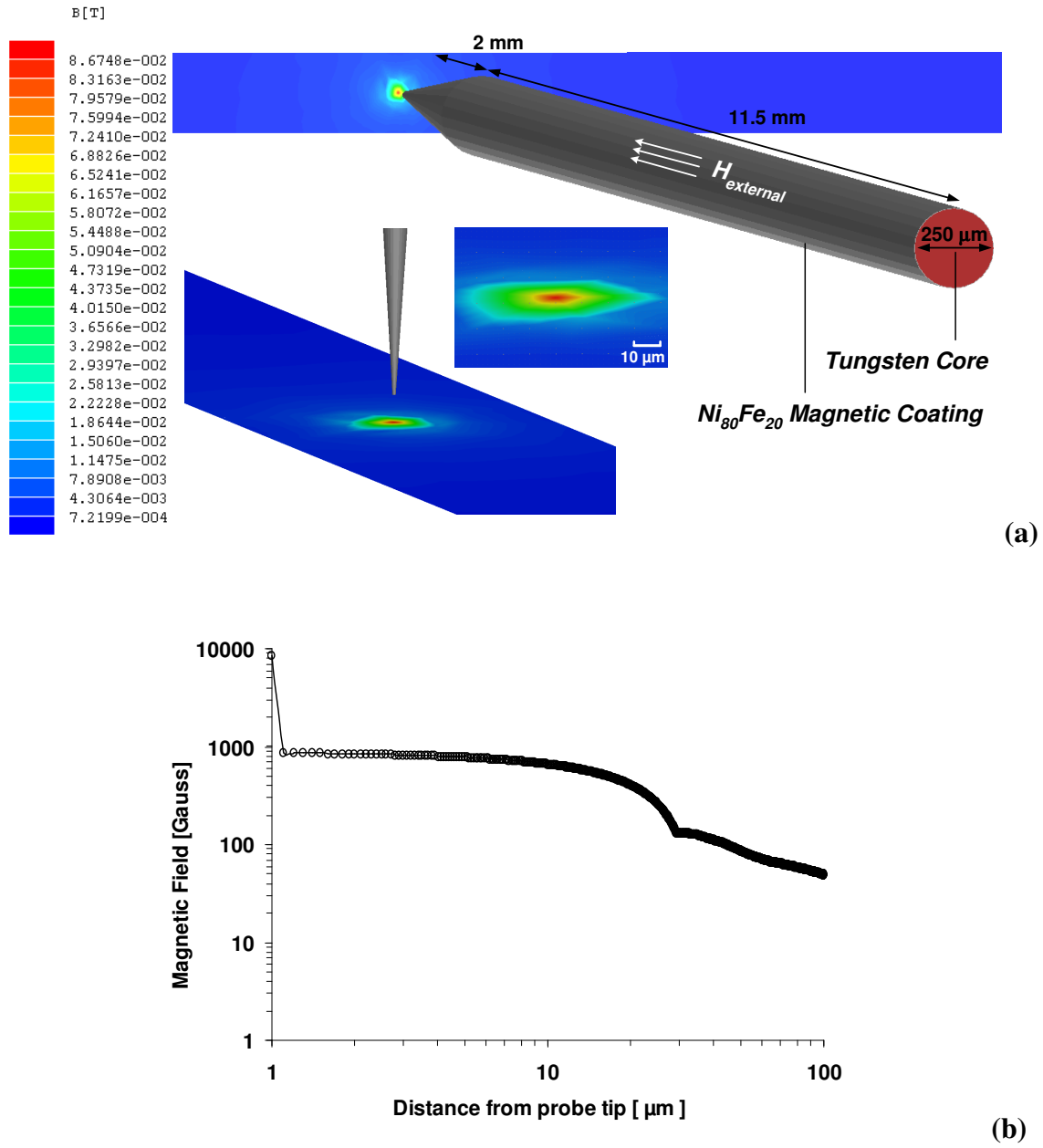


Figure 14. Finite element simulation of the magnetic field generated by a permalloy-coated tungsten probe: (a) The spatial field distribution below the tip; (b) The line plot (in log scale) of the magnetic field vs. the distance from the probe tip.

3.2.2 Fabrication

The micro electromagnetic probe consists of two major components: a magnetic core and a conducting coil. For the magnetic core, sharpened tungsten needles (with tip radii of 0.5 μm) obtained from Signatone (Gilroy, CA) were used as structural molds. The permalloy coating was deposited with electroplating in a home-made solution (Table 1).

Table 1. Permalloy plating solution composition and electroplating conditions.

Bath Composition		Operating Conditions	
NiCl ₂ 6H ₂ O	39 g/L	pH	2.7-2.8
NiSO ₄ 6H ₂ O	16.3 g/L	Temperature	20-25°C
H ₃ BO ₄	25 g/L		
Sodium Saccharin	1.5g/L		
NaCl	25g/L		
FeSO ₄ 7H ₂ O	1.4g/L		

To ensure high magnetic field localization and gradient, it is necessary to maintain the sharp probe tip profile after permalloy electroplating. Several electroplating experiments were conducted to determine optimal plating conditions. First, a typical electroplating setup having a large anode to cathode separation ($\sim 7\text{cm}$) was tested, in which the tungsten probe (cathode) was placed parallel to a 3-inch permalloy sputtering target (anode) (figure 15(a)). However, this configuration was found to result in poor selective deposition, and difficult to retain the initial profile of the tungsten probe tip. Figures 15(b) and (c) show the scanning electron micrographs of the tungsten probe before and after electroplating, which clearly indicate the rounding of a sharp tip after permalloy electroplating. As shown in figure 16, in order to preserve the probe tip profile, the ratio of the deposition at the probe shank to the deposition on the

probe tip ($\Delta x/\Delta y$) must be equal to or less than $\tan(\alpha_1)$ or w/l . Considering the specific dimensions of the used tungsten probe ($w = 0.005$ in and $l = 0.08$ in), the deposition at the probe tip must be at least 16 times as much as that on the probe shank.

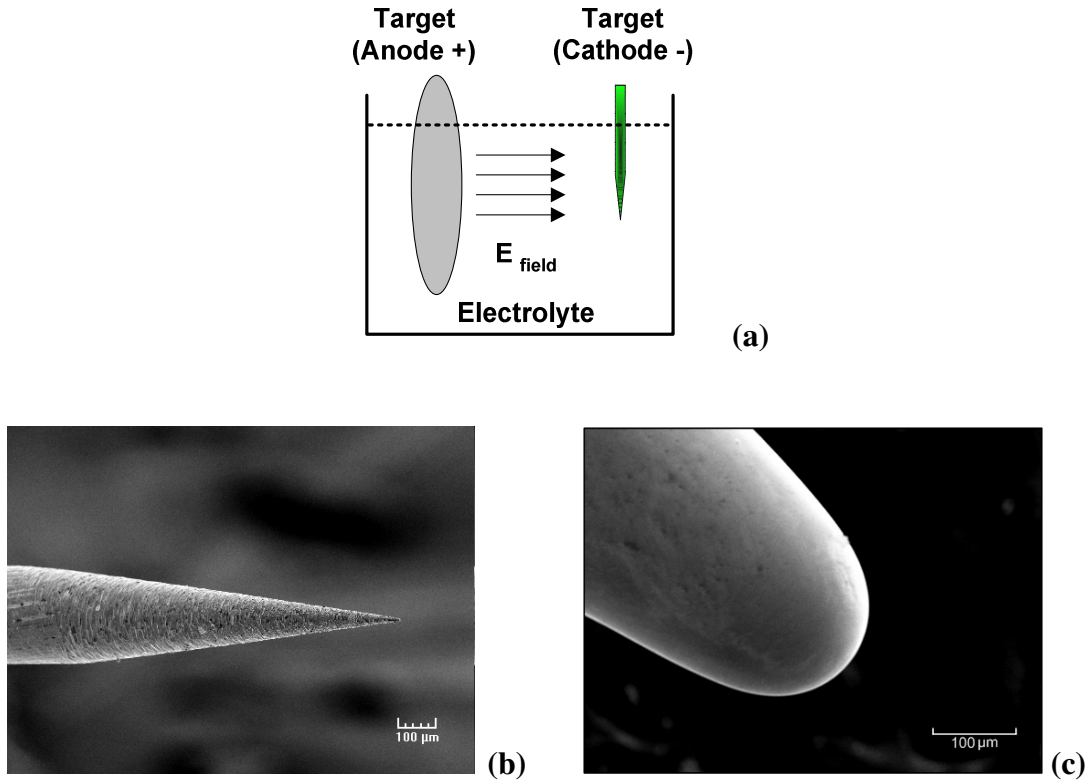


Figure 15. (a) Schematic of a typical electroplating setup, where the entire target is exposed to the plating solution, with large anode-cathode separations; (b) Scanning electron micrographs of the commercially obtained tungsten needle before permalloy coating; (c) Scanning electron micrographs of the commercially obtained tungsten needle after permalloy coating.

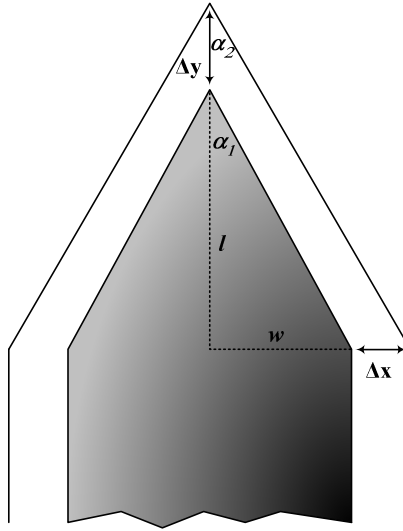


Figure 16. Illustration of the deposition rate necessary to preserve the tip profile. In order to have the same probe profile ($\alpha_1 = \alpha_2$) or decrease the taper angle ($\alpha_2 < \alpha_1$), the deposition ratio $\Delta x / \Delta y$ should be less than or equal to $\tan(\alpha_1)$ or w/l . The grey region represents the original tungsten needle structure.

To address the above issue, a new electroplating setup was investigated to achieve the needed non-uniform and localized permalloy deposition. In the new electroplating configuration, the tip of the tungsten probe (cathode) is placed vertically above the permalloy target at a very small distance and the active area of the plating cell is confined within a narrow region. During electroplating, the sharp tip of the tungsten probe and the small gap between the anode and cathode facilitate the concentration of electric field and thus current density at the tip [48, 49]. Since the deposition rate is proportional to the current density, the needed localized deposition can be expected. To study the micro-scale, localized plating process, finite element simulations using Maxwell 2D[®] software were performed to reveal the current density (J) distribution at the tungsten probe tip under the new plating condition. In the simulation, an electrical conductivity of 19.43 $\mu\text{S}/\text{cm}$ was used for the plating solution, which was determined through measurements. A DC bias of 0.91V was tentatively applied between the anode (permalloy target) and cathode (tungsten needle). Theoretically, this DC bias would

produce a uniform current density of $\sim 5 \text{ mA/cm}^2$ on a flat surface tantamount to the probe area immersed in the electrolyte, which is suitable for permalloy electroplating.

Figure 17 shows the simulated 2D spatial distribution of the current density and the line plot of the distribution along the trajectory of the tapered region. It clearly indicates the existence of a non-uniform and highly localized current density distribution. The current density and thus deposition rate at the probe tip is 48.8 times higher than those at other regions of the tungsten probe.

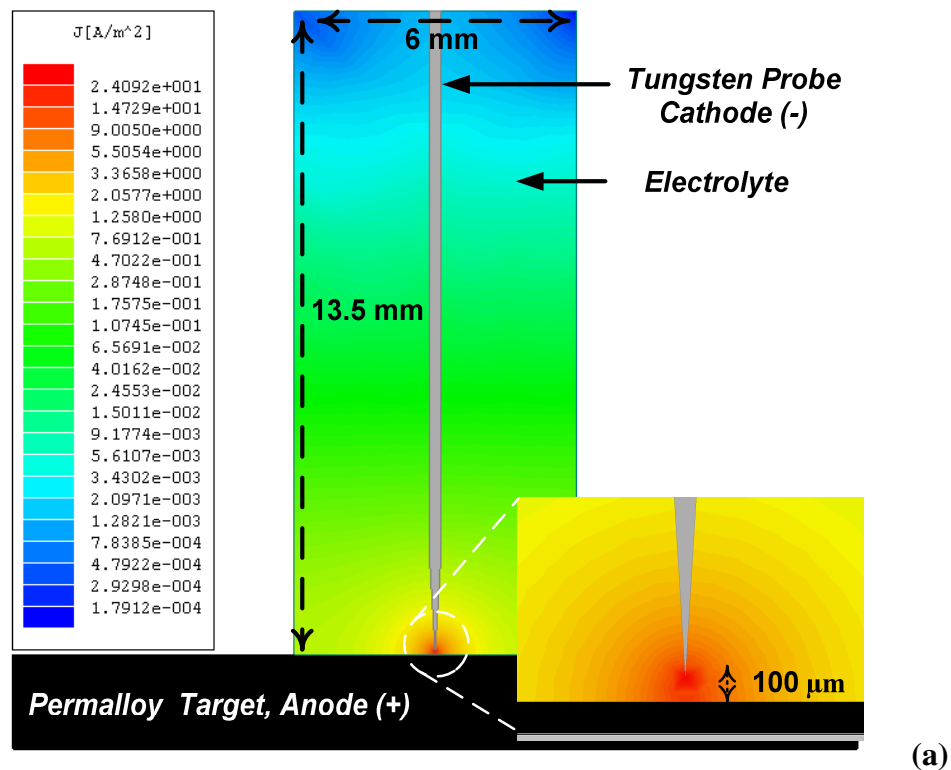


Figure 17. Finite element simulation showing the current density distribution on the tungsten probe.

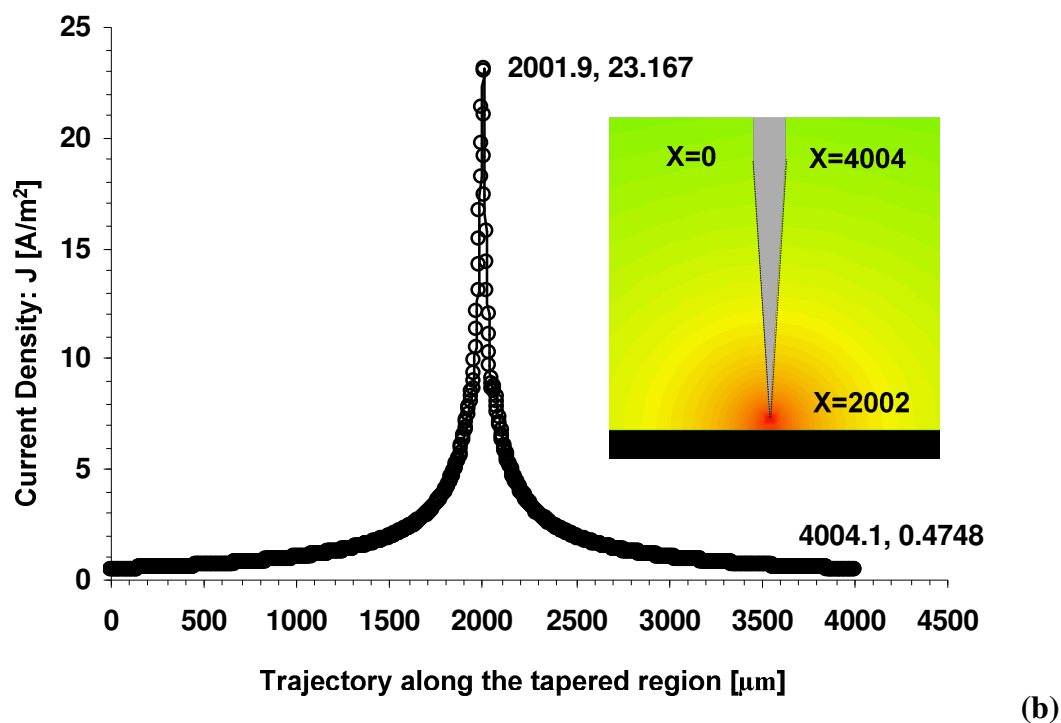


Figure 17. Continued.

To construct the new plating setup, plastic tubing was glued on the 3 inch permalloy target and used as a container to hold the electroplating solution (figure 18).

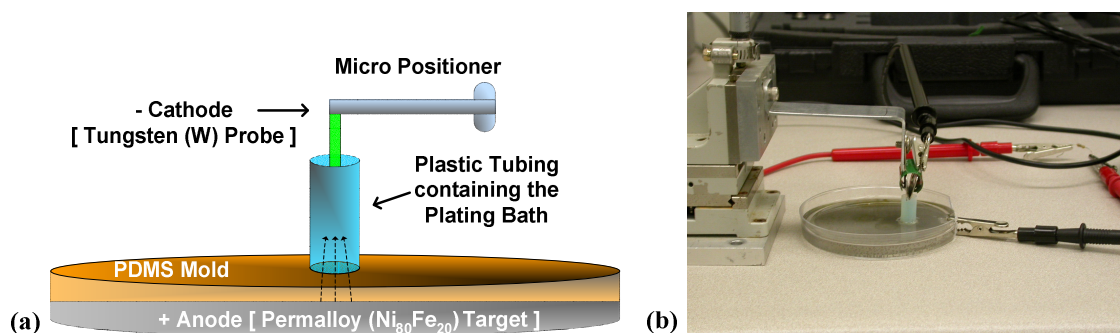


Figure 18. (a) Schematic of the new electroplating setup to enable controlled plating of permalloy; (b) the actual setup.

After mounted on a micromanipulator stage for accurate vertical positioning, a tungsten probe was connected to a multimeter and lowered down to contact the permalloy target. The current passing through the plating cell was constantly monitored as the probe was lowered down. When the current reading rapidly increased, this meant that the probe was in contact with the target. At this point, the probe was raised back a few steps ($\sim 100\text{ }\mu\text{m}$) using the dial on the micromanipulator, after which normal current levels were observed again. The current was then adjusted at 0.5 mA to provide the necessary current density levels used in the simulation. With this electroplating method, the original tungsten probe tip profile could be preserved after electroplating a $25\text{ }\mu\text{m}$ -thick permalloy layer (figure 19).

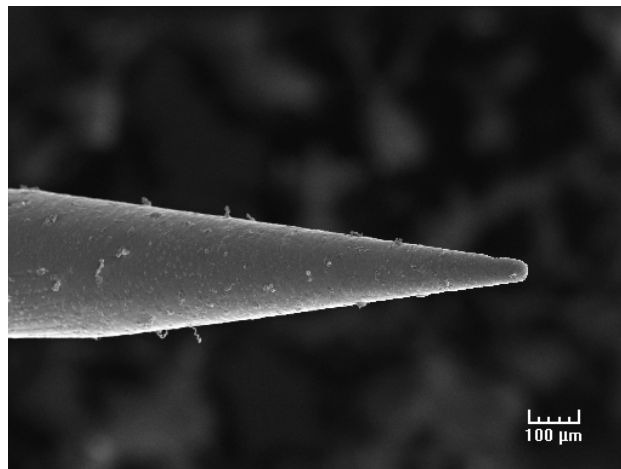


Figure 19. Scanning electron micrograph of a permalloy-coated tungsten needle using the new plating setup.

Following permalloy electroplating, insulated copper magnet wire was manually wound around the magnetic core to form the solenoid structure, which completed the probe fabrication (figure 20). To provide the necessary turn density for magnetic field generation, 120 turns of wire were wound within 6 mm. A bi-layer coil structure was used to further improve the turn density and facilitate field generation. The entire

solenoid structure has a resistance of $0.9\ \Omega$ and is positioned within 1 mm from the tip of the magnetic core.

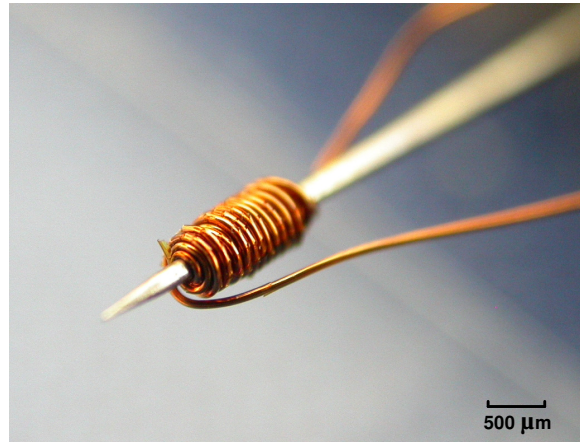


Figure 20. Optical image of the permalloy-coated tungsten magnetic probe.

3.2.3 Characterization

Due to its highly localized nature, it is difficult to experimentally characterize the magnetic field produced by the micro electromagnetic probe. This is because conventional magnetic measurement devices (e.g. Gauss meter), do not provide the necessary spatial resolution. To address this issue, a scanning Hall probe microscope (SHPM) system was used to conduct experimental characterization of the probe performance. The SHPM system consists of a computer controlled stage and a very fine Hall sensing element to provide the necessary spatial resolution for measuring the field produced by the magnetic probe.

To characterize the output magnetic field, the probe was positioned under the Hall sensing element and raised up until only a small gap ($\sim 30\ \mu\text{m}$) was left so that possible collision damages to the sensor element and the probe tip are prevented. Before the testing, the micro electromagnetic probe tip was demagnetized using the built-in coil of the SHPM by applying an exponentially decaying sinusoidal magnetic field with alternating polarity to the axis of the magnetic core. After the demagnetization, the peak

output magnetic field density (B) as a function of the input current (I) was measured. As shown in (figure 21), the output magnetic field density (B) first increases linearly as a function of the input current (I) and then saturates around 150 Gauss with an applied current of 0.4 A.

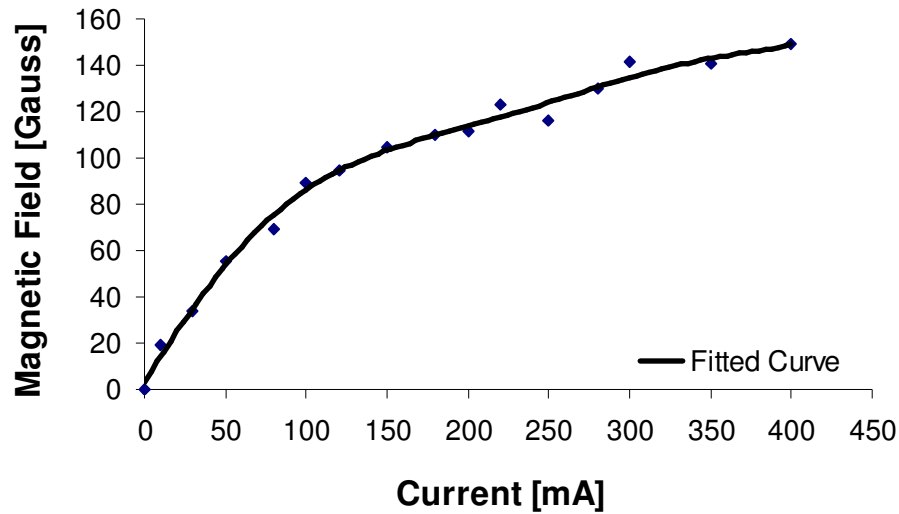


Figure 21. Experimental SHPM measurement of the output magnetic field vs. DC input current for the tested micro electromagnetic probe.

To verify that electroplating of the magnetic permalloy layer actually provided the desired magnetic property on the tungsten probe, the B-H curve of the electroplated probe was also measured, which shows a characteristic hysteresis and low remnant magnetization for a soft magnetic material (figure 22). The experimental characterization results demonstrate the magnetic field generation capability of the hybrid permalloy-coated tungsten magnetic probe.

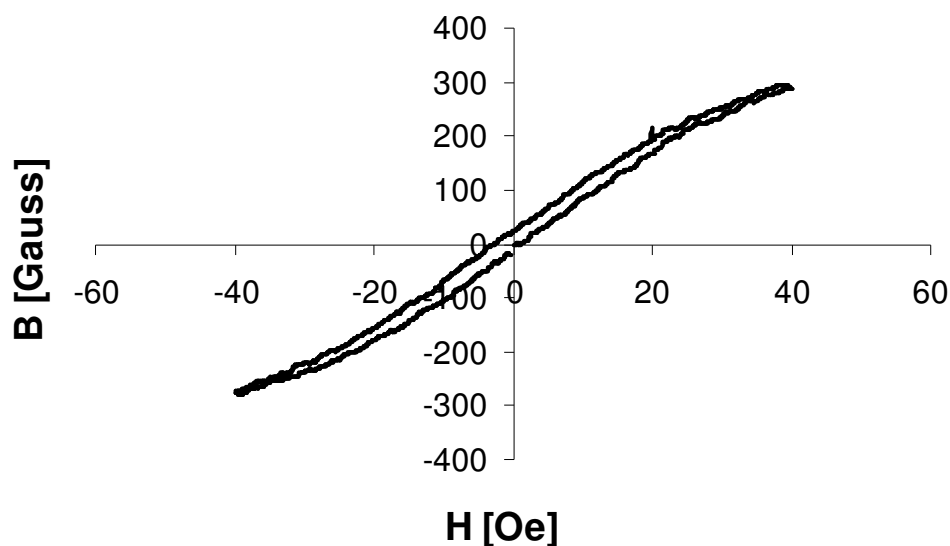


Figure 22. B-H curve of the magnetic probe measured using the scanning Hall probe microscope.

3.3 Droplet Synthesis

Alginate droplets were synthesized for the manipulation experiments with the developed micro electromagnetic probe. The motivation for manipulating alginate droplets were due their widespread use in the pharmaceutical industry and their potential as drug carrying agents for controlled release of drugs [50, 51]. With an electrospray device [52-54], alginate droplets of size (150-200 μm) were made and iron oxide magnetic particles were encapsulated inside the droplets. The materials used for the synthesis include sodium alginate (powder) and calcium chloride (from Sigma-Aldrich, Milwaukee, WI) and SPHERO™ streptavidin magnetic particles (1.89 μm mean diameter and 0.5% wt) (from Spherotech Inc, Lake Forest, IL). Figure 23 shows the process flow for synthesis of alginate droplets.

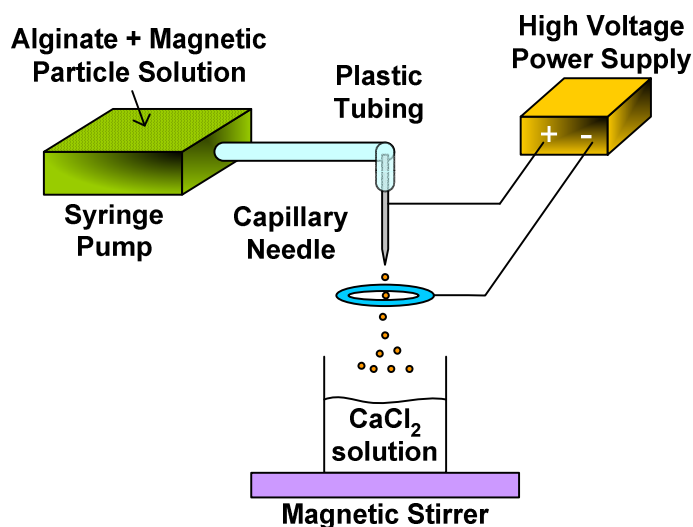


Figure 23. Illustration of the synthesis of stable alginate droplets containing magnetic particles. The alginate and magnetic particle solution is put in a syringe pump and applied to a capillary needle that is connected to an electro spray device.

First, 2% wt alginate aqueous solution was made by mixing alginate powder with DI water. Streptavidin magnetic particles were well dispersed into the alginate solution. The alginate solution (containing magnetic particles) was filled to a plastic clinic syringe and then mounted on a syringe pump. The pump controlled the flow rate, and then the alginate solution was conducted to an electro spray device. Alginate droplets of different sizes were generated in the dripping mode by tuning the voltage and frequency. They were immediately collected in calcium chloride solution (2% wt), in which the alginate quickly gelled and encapsulated the magnetic particles inside. Two types of alginate droplets having high and low concentrations of magnetic particles were obtained by adjusting the initial magnetic particle content in the alginate solution. The magnetic alginate gel particles were extracted for the following droplet manipulation experiments.

3.4 Droplet Manipulation

Droplets containing magnetic particles were first mixed with water, then placed on top of a microscope glass slide with an etched groove and sealed with a thin, glass

cover slip (Micro Cover Glasses No.1, 150 μ m thick), (from VWR, West Chester, PA). The manipulation experiments were conducted under a microscope stage equipped with a CCD camera for recording the motion of the droplets during manipulation. The magnetic probe controlled by a micro manipulator was first lowered down to the top surface of the cover slip (figure 24).

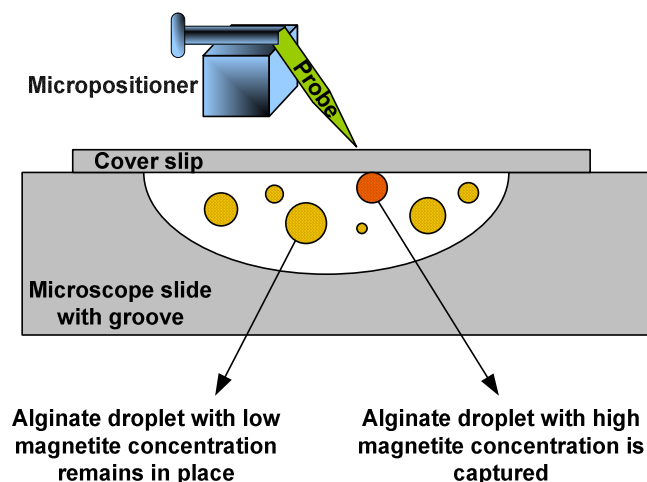


Figure 24. Illustration of droplet manipulation with the new electromagnetic probe. In selective droplet capture the cover slip in the figure is kept in place, whereas in non-selective droplet capture and capture-transport experiments the cover slip is removed.

After an input current (0.35 A) was supplied, a concentration-based manipulation of the alginate droplets was observed. Alginate droplet with a high concentration of magnetic particles was captured while the droplets with low magnetite concentration were not affected (figure 25). A frame grabber was used to analyze the displacement of the droplet within a given time. The average velocity of the manipulated droplet (with high concentration of magnetic particles) was determined to be 4.35 μ m/s.

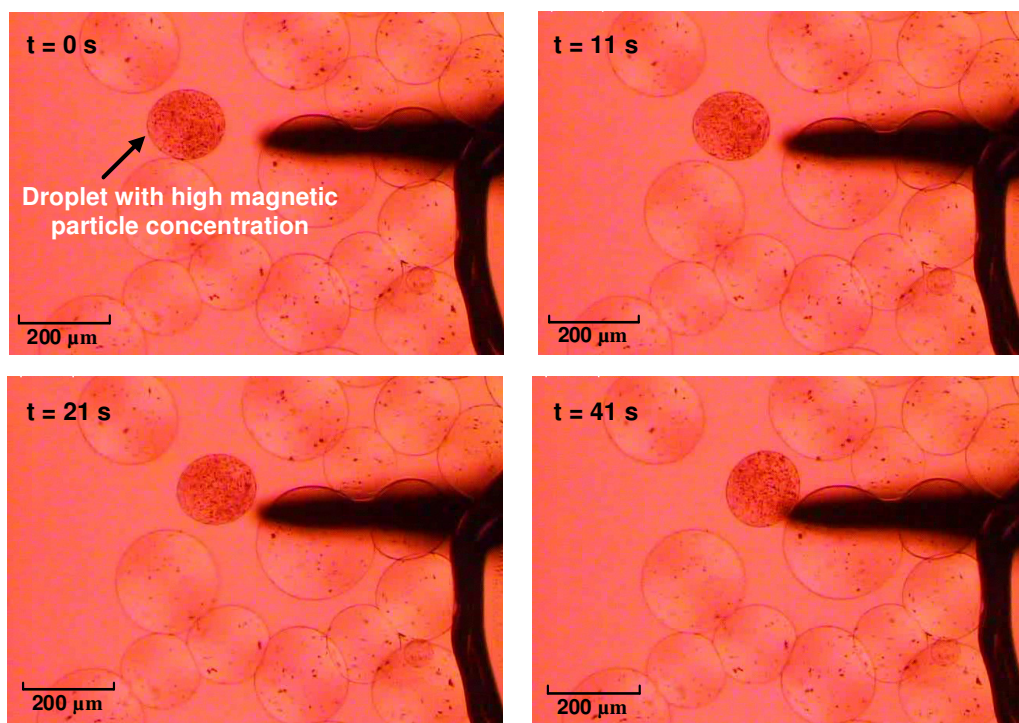


Figure 25. Concentration dependent manipulation of alginate droplets.

To evaluate and compare the effects of the cover slip on the droplet manipulation, the same experimental procedure was repeated without the cover slip. The electromagnetic probe was lowered down to the location where its sharp tip just touched the surface of the solution. After the probe is turned on, a non-selective capture (less than 2 seconds) of all the droplets (regardless of their magnetic particle concentration) was observed (figure 26). An average velocity of the droplets was determined to be 1.69 mm/s. The captured droplets were released after the probe was turned off.

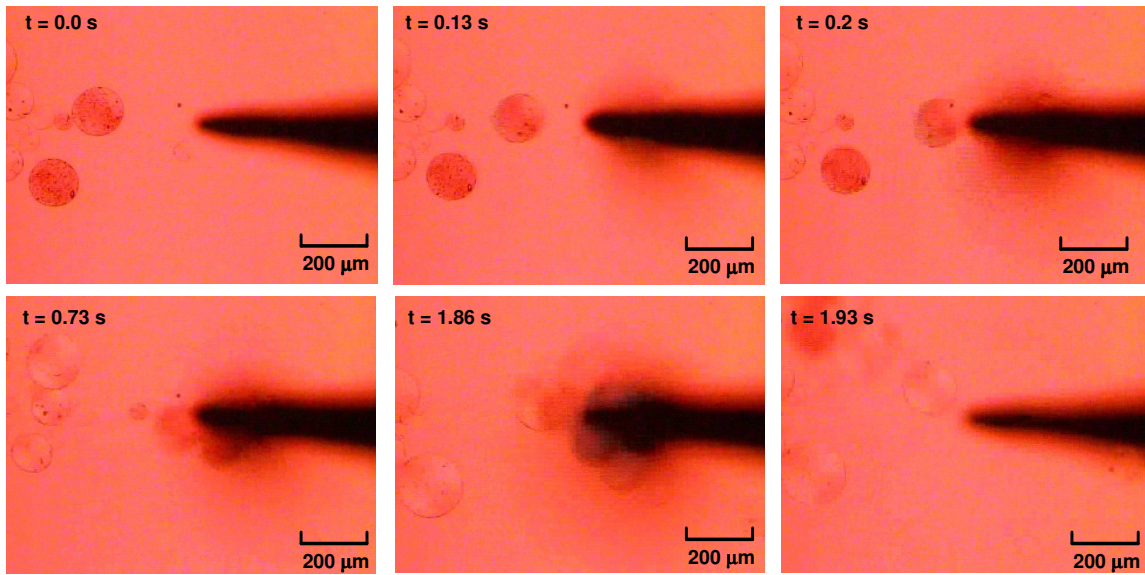


Figure 26. Non-selective droplet manipulation.

Experiments were also conducted (without the cover slip) to test the capability of the electromagnetic probe in capturing and transporting droplets on a microfluidic platform (figure 27). At $t=0$ s, the electromagnetic probe was lowered down to the surface of the droplet solution and turned on to capture the droplets. The probe was then moved continuously at a speed of 0.6 mm/sec for about 20 seconds. All the initially captured droplets remained within the vicinity of the probe tip during the entire transport process and any droplet along the probe trajectory was also captured. After the transport process, the electromagnetic probe was turned off to release the transported droplets at the new location.

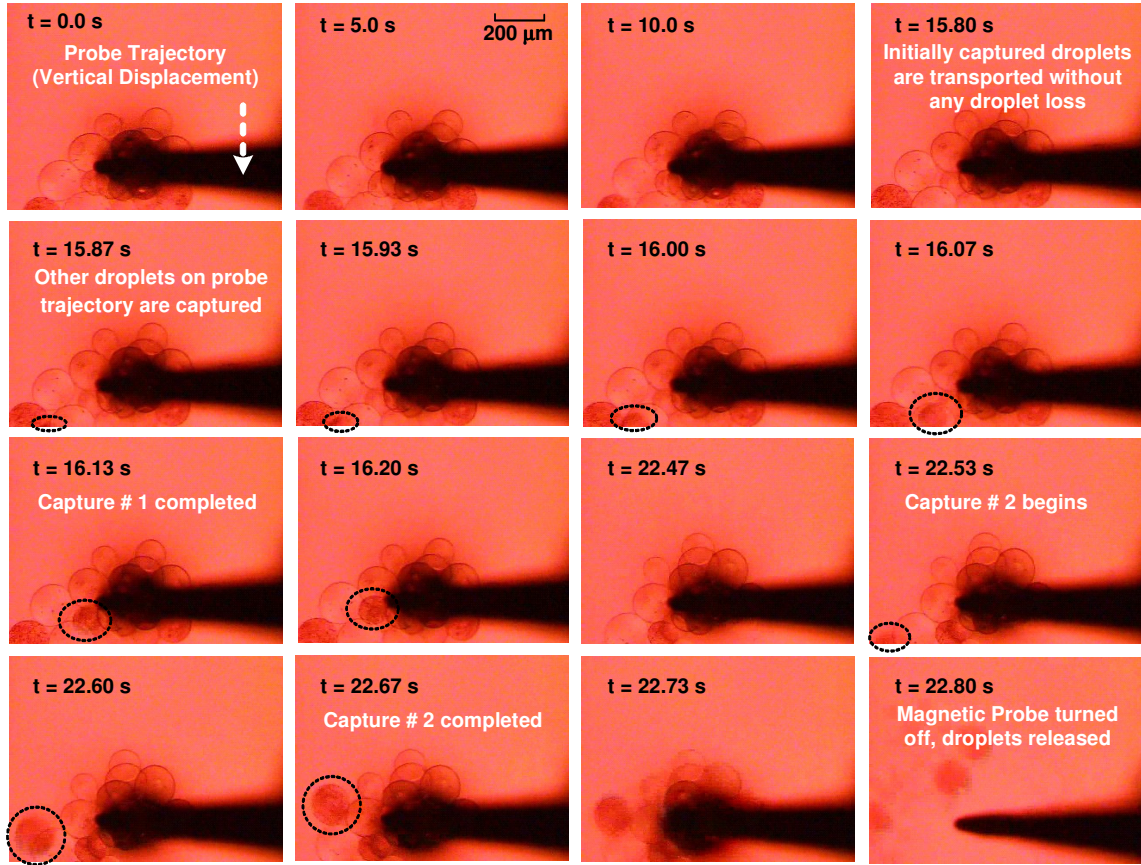


Figure 27. Droplet capture and transportation.

3.5 Results and Discussion

During magnetic manipulation, the micro droplets are subject to the action of three major forces: the magnetic actuation, the hydrodynamic drag and the friction (at the presence of the cover slip). The two other forces acting on the droplets (gravity and buoyancy) can be neglected, since the density of the alginate droplets (prepared from 2% wt solution of alginate powder and water) match very well with water [55]. First, the magnetic force acting on each droplet is estimated as,

$$F_m = \nabla(m \cdot B) = \frac{V\chi_m}{\mu_0} B \nabla B \quad (1)$$

where \mathbf{m} and χ_m are the magnetic moment and volumetric magnetic susceptibility of the magnetic particles, respectively, \mathbf{B} is the magnetic field at the location of the droplet, and V is the effective volume of all the magnetic particles encapsulated in the droplet [56].

In case of manipulating droplets underneath a cover slip, there will be additional frictional forces encountered by the droplets due to the resistance presented by the glass walls against the droplet motion. As a result, the net force for the manipulation of the droplets will be less than the magnetic actuation force and is equal to,

$$\mathbf{F}_{net} = \mathbf{F}_m - \mathbf{F}_f \quad (2)$$

where \mathbf{F}_f represents the friction force. Depending on the friction constant of the wall, the net force experienced by the droplets upon manipulation will be different.

On the other hand, according to Stoke's theorem, a particle moving inside a fluid with viscosity η experiences a hydrodynamic drag force (viscous force) given by,

$$\mathbf{F}_d = 6\pi\eta r\mathbf{v} \quad (3)$$

where r is the particle radius, and \mathbf{v} is the relative velocity of the particle with respect to the surrounding media [27]. The drag force represents the resistance presented by the liquid against the motion of the droplets. Initially, when the magnetic field is turned on, droplets accelerate and reach a velocity at which the net actuation force is balanced by the drag force. Therefore, at equilibrium when the droplets are still or moving with constant velocity, the net manipulation force is equal to the drag force, which gives,

$$\mathbf{F}_{net} = \mathbf{F}_d = 6\pi\eta r\mathbf{v} \quad (4)$$

In the manipulation experiments, the presence of the cover slip has two effects on the manipulation of the droplets. First, it separates the tip of the magnetic probe farther away from the droplets, resulting in smaller magnetic field (\mathbf{B}) and field gradient ($\nabla\mathbf{B}$) at the location of the droplets. Second, it presents additional friction on the manipulated droplets when they slide against it. Only for the droplets with the higher concentration of magnetic particles, the magnetic force (\mathbf{F}_m) can be large enough to overcome the

friction force (F_f), resulting in a selective manipulation. Meanwhile, the existence of the friction force reduces the total net force (F_{net}) for droplet manipulation, leading to a slow moving speed for the manipulated droplets. The removal of the cover slip eliminates the F_f and increases F_m (due to smaller distance of the probe tip and the droplets). As a result, the larger F_{net} leads to the non-selective manipulation of all the droplets at a much faster speed. With the larger F_{net} , it is also possible to readily capture and transport droplets to different locations within the microfluidic platform.

Equation 4 provides an effective way to estimate F_{net} or F_m , which is otherwise difficult to directly measure. For concentration-based selective droplet capture (with the presence of a cover slip), observing the motion of the droplet having high magnetic particle concentration (diameter: 172 μm , velocity = 4.35 $\mu\text{m/s}$) inside water medium (η : 1002 $\mu\text{Pa.s}$) F_d as well as F_{net} is calculated as 7.05 pN. Alternatively, for non-selective droplet capture (without the cover slip), F_d as well as F_m is determined to be 2.34 nN.

3.6 Conclusions

A new electromagnetic probe has been successfully developed and tested in the manipulation of micro alginate droplets. By employing an innovative hybrid magnetic core structure, the fabrication of the electromagnetic probe is conducted in a straightforward and simple manner. The hybrid core structure is also expected to improve the mechanical strength and stability of the probe. The magnetic response of the electromagnetic probe is verified with both simulation and experimental characterization, showing the feasibility of the hybrid magnetic core approach.

In micro alginate droplet manipulation, depending on the magnetic particle concentration, the strength of the applied magnetic field and the surface properties (e.g. friction coefficient and hydrophobicity) of the manipulation platform, different manipulation schemes (selective or non-selective) have been demonstrated, which can be readily tailored for different applications, such as sorting.

CHAPTER IV

GOLD-COATED SCANNING PROBES FOR DIRECT WRITE OF SUB-MICRON METALLIC STRUCTURES

4.1 Introduction

In the past decade, scanning probe (SP) instruments, such as atomic force microscope (AFM) have become not only powerful nanoimaging tools, but also versatile platforms for nanofabrication under ambient conditions [57]. By using the sharp scanning probe tip to introduce certain physiochemical interactions or dispense pre-coated materials, nanoscale patterns or structures can be directly generated at desired locations. For SP-based nanofabrication, the direct “write” capability is critical since it eliminates the need for additional chemicals (e.g. resists for material patterning) and processing steps (e.g. lithography and etching). As a result, a much more efficient and lower-cost fabrication process with greater material compatibility (especially with biological materials on chip) could be achieved.

However, one fundamental challenge in current SP-based nanofabrication technology is the direct “write” of metallic nanostructures, which are critical for the development of many nano devices and systems (e.g. as electrodes, interconnects and catalysts). Due to their insolubility in both water and solvents, metal atoms are “immobile” under ambient conditions. Unlike many other materials, it is difficult to achieve direct metal material transfer from the probe tip to the fabrication substrate. To address this issue, soluble metallic salt or precursor were first deposited on a substrate surface and then converted into metal atoms with chemical reductions [58, 59]. More recently, scanning probes have been used in conjunction with pulsed currents to achieve deposition on material surfaces [60, 61]. Deposition of metals with low melting temperatures (e.g. indium) was also demonstrated by heating the tip of a scanning probe to very high temperatures [62]. Nevertheless, these approaches inevitably involve certain physical inputs or chemical processes, which may incur compatibility issues with the substrates and other pre-deposited materials.

This chapter discusses the fabrication and application of new gold-coated scanning probes with controllably-formed tip profile for a successful demonstration of direct “write” of sub-micron gold structures on a smooth silicon surface. The formation of the gold structures is a result of direct material transfer from the gold coating on the probe tip to the silicon surface, which is believed to be triggered by the friction-induced bonding of gold and silicon atoms (as often seen in adhesive wear) during repetitive probe scanning (figure 28). Since friction and wear exist in nearly all material system, this technique is expected to provide a general approach to achieve SP-based direct “write” of metallic micro and nanostructures.

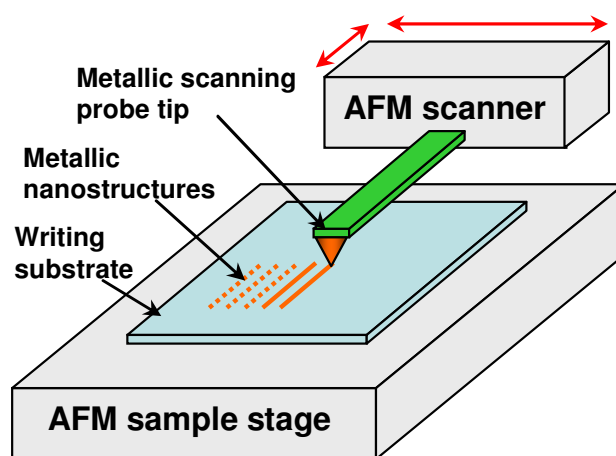


Figure 28. An illustration of the direct “write” of metallic nanostructures using a metal-coated scanning probe.

4.2 Principle of Material Transfer

As early as late 1960s, people have observed smoothed metal surfaces of packed and reorganized atoms due to mechanical polishing [63]. Fundamental study has shown that mechanical stimulation (e.g. friction) triggers chemical reactions that are different from equilibrium chemical reactions. For example, when materials are under friction, they can be oxidized and dissolved by the interaction of frictional stresses and chemical attack in water [64-67]. Another detailed study on friction-induced chemical reaction

has been conducted on boundary lubrication of steels [68, 69]. Without any lubricants, metals generate metallic bonds, plastic deformation, and mechanically mixed layers. The feasibility of friction-stimulated nanostructure growth was also demonstrated on brushite with probe scanning on AFM [70, 71]. Based on these prior research results, it is believed that the frictional energy associated with probe scanning induce bonding of probe tip and substrate materials and enable subsequent formation of metallic structures in the path of probe scanning.

To demonstrate the SP-based direct “write” of metallic structures, investigations were focused on gold and single crystal silicon surface. Silicon is commonly used in microelectronics as the substrate for device and circuit fabrication. On the other hand, gold is chemically stable and can form eutectic phase and thus good bonding with silicon [72]. These unique properties make the gold-silicon system a good candidate for the direct “write” experiments. Once successful, the directly-written gold structure could be readily interfaced with silicon microelectronics, which could be useful for the development of integrated nanobiosensor systems [73-75].

4.3 Probe Fabrication

To demonstrate the SP-based direct “write” of gold structures on silicon surface, first commercially-available standard AFM imaging probes (made of silicon nitride) were used. Before the “writing”, a thin layer of gold (~200 nm thick) coating was formed on the tip of each probe using thermal evaporation, which was verified under an SEM (scanning electron microscope). Different “writing” conditions (e.g. scanning speed and duration) were tested. After each “writing”, the original gold coating was completely removed and a new coating was re-applied. However, the “writing” results were found to be inconsistent (in pattern filling, width and thickness) among different probes and also different trials with the same probe. It is believed that this inconsistency is mainly due to the non-uniform tip profile of the AFM probes, which caused different tip-substrate contact and thus friction-wear conditions for gold transfer. The non-uniformity in the probe tip profile would be caused by the following conditions: 1) Due

to the nature of its fabrication process, there exists a variation in the probe tip profile after the probe fabrication; 2) The thermal evaporation of gold on the highly-protruding probe tip structure would result in non-conformal coatings onto different probe tips; 3) These two variations would manifest and augment themselves in the initial and transient tip-substrate contact during the “writing” process (where the gold coating is gradually consumed), which would cause random and inconsistent friction-wear process for gold transfer.

To address this issue, new gold-coated scanning probes with refined tip profiles were fabricated to achieve more consistent and repeatable “writing” results. The probe fabrication process is illustrated in figure 29. First, a thin layer of silicon oxide was grown on a {100} oriented silicon wafer using thermal oxidation and then patterned into square patches to serve as the etch mask for silicon bulk etching (figures 29(a) and (b)). Second, silicon bulk etching was conducted in EDP (ethylene diamine pyrocatechol) solution to form mesa structures (figure 29(c)). Third, thermal oxidation and subsequent oxide removal were conducted to sharpen the bulk etched mesa structures, which would serve as a mould for the subsequent probe tip formation (figure 29(d)). Next, silicon nitride was deposited using LPCVD (low pressure chemical vapor deposition) and patterned using reactive ion etching to define the scanning probe structures (figures 29(e) and (f)). Finally, the silicon nitride scanning probes with protruding cantilevers are formed by backside etching of the bulk silicon with EDP (figure 29(g)).

The unique aspect of the above probe fabrication process lies in its capability of creating uniform tip profile and more importantly precisely defining the tip radius of curvature. As shown in figure 29(e), due to the conformal nature of the LPCVD process, when the silicon nitride layer was deposited onto the sharpened bulk-etched mesa structure, the molded silicon nitride probe tips automatically assume a spherical tip apex. The radius of curvature of the probe tip is equivalent to the thickness of the deposited silicon nitride layer.

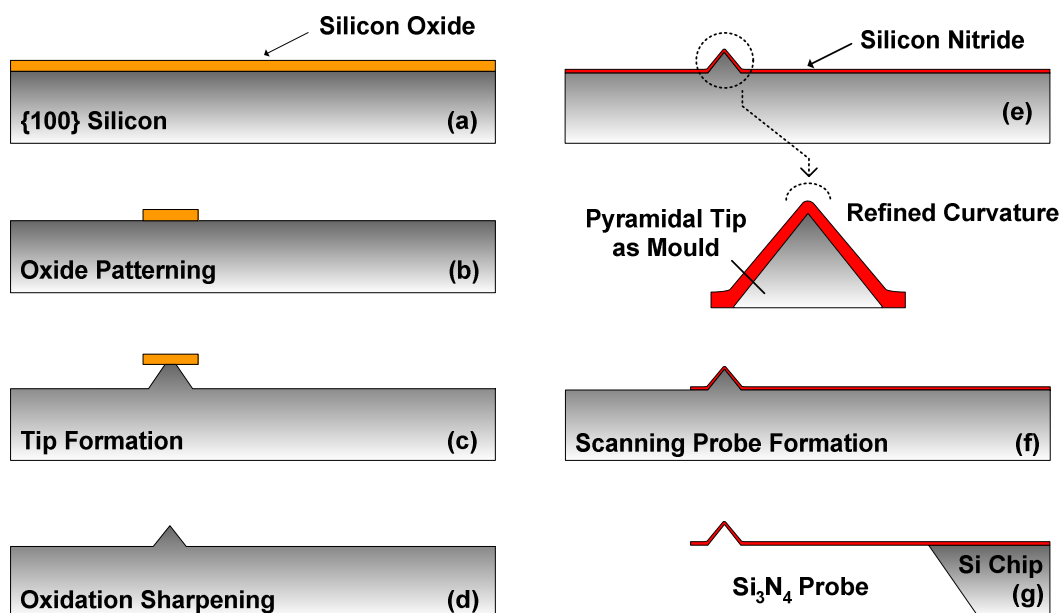


Figure 29. Process flow diagram outlining the fabrication of the scanning probes.

Using such probe tips on a flat surface naturally forms a predictable ball-surface sliding contact. Although the original tip profile and radius of curvature would change after the (non-uniform) gold coating, as long as the thickness of the gold coating is much less than thickness of the silicon nitride layer, a stable and consistent tip-substrate contact can be maintained during the probe scanning, which is critical for repeatable “writing” results. It should be noted that the deposition of silicon nitride and gold layer increases the radius of curvature of the probe tip, thus creating a more “blunt” tip. However, since the actual tip-substrate contact area is usually much smaller than the radius of curvature, direct “write” of sub-micron or even nanometer-sized gold structures is still possible.

Figure 30(a) shows the SEM micrograph of an array of fabricated scanning probes. Each scanning probe consists of a silicon nitride cantilever (900 nm thick). The probes are 320 μm long and 100 μm wide. Using a Young’s modulus of 260.5 GPa for LPCVD Si₃N₄ thin film [76], the force constant of the probe cantilever is calculated to be ~ 0.145 N/m, which is suitable for scanning on a hard silicon surface. To prepare for the

direct “write” of gold nanostructures, the nitride probes were coated with a 2-nm-thick chromium layer and a 200-nm-thick gold layer with thermal evaporation (figure 30(b)).

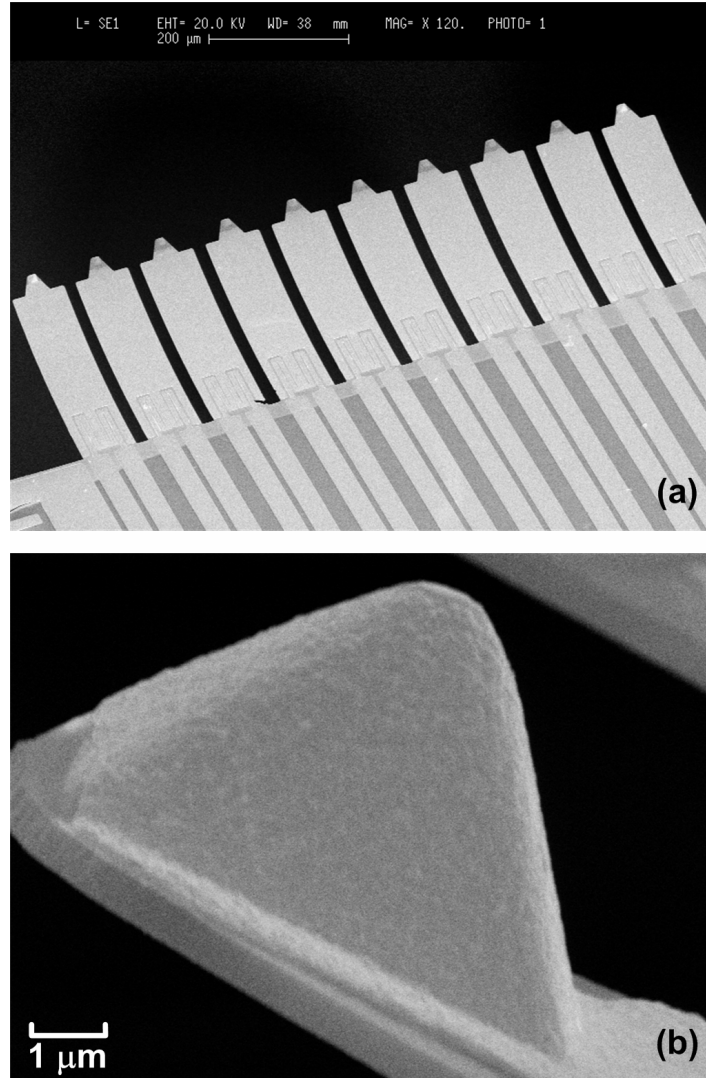


Figure 30. Scanning electron micrograph of an array of fabricated scanning probes for the writing experiment: (a) The entire array; (b) Zoom-in view of a probe tip.

4.4 Experimental Results

To test the effect of different “writing” conditions on the formation of gold structures, each scanning probe in the probe array was contacted onto silicon surface to

conduct the scanning one by one. After certain number of scans, the tip of the scanning probe was inspected under the SEM. Figure 31 shows a typical wear scar at the probe tip, which indicates a clear abrasive wear and loss of the gold coating due to material transfer.

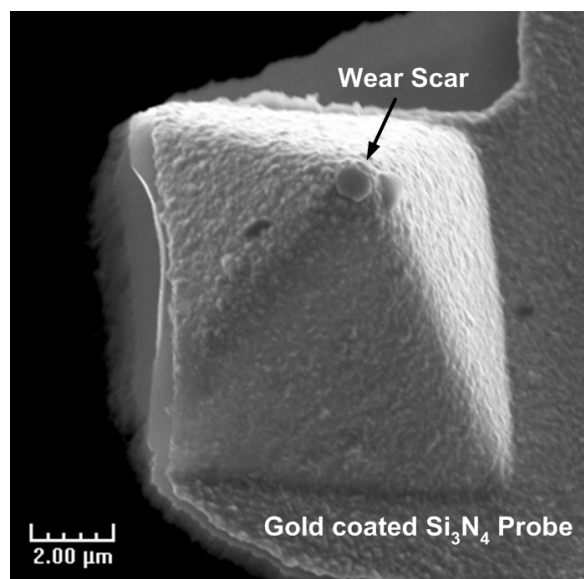


Figure 31. A scanning electron micrograph showing the existence of a wear scar on the scanning probe tip after writing.

Figure 32 shows the AFM images of a series of metallic gold structures that were written on the silicon surface. Figures 32(a) and (b) show continuous gold lines with dimensions ~ 600 nm wide and ~ 9 nm thick, and ~ 400 nm wide and ~ 4 nm thick formed after 100 scans ($80 \mu\text{m}/\text{scan}$) at a scanning speed of $480 \mu\text{m}/\text{sec}$ and at a contact force of ~ 500 nN. Under this condition, the “writing” of the line patterns was highly repeatable with the fabricated scanning probes and the width of the lines closely matched the size of the wear scar, which is smaller than the radius of curvature of the probe tip after gold deposition. However, as shown in figure 32(c) in rare cases dotted structures (ranging between ~ 650 - 900 nm in diameter) were generated rather than a continuous line, which is believed to arise due to some special conditions during writing and would require further investigation.

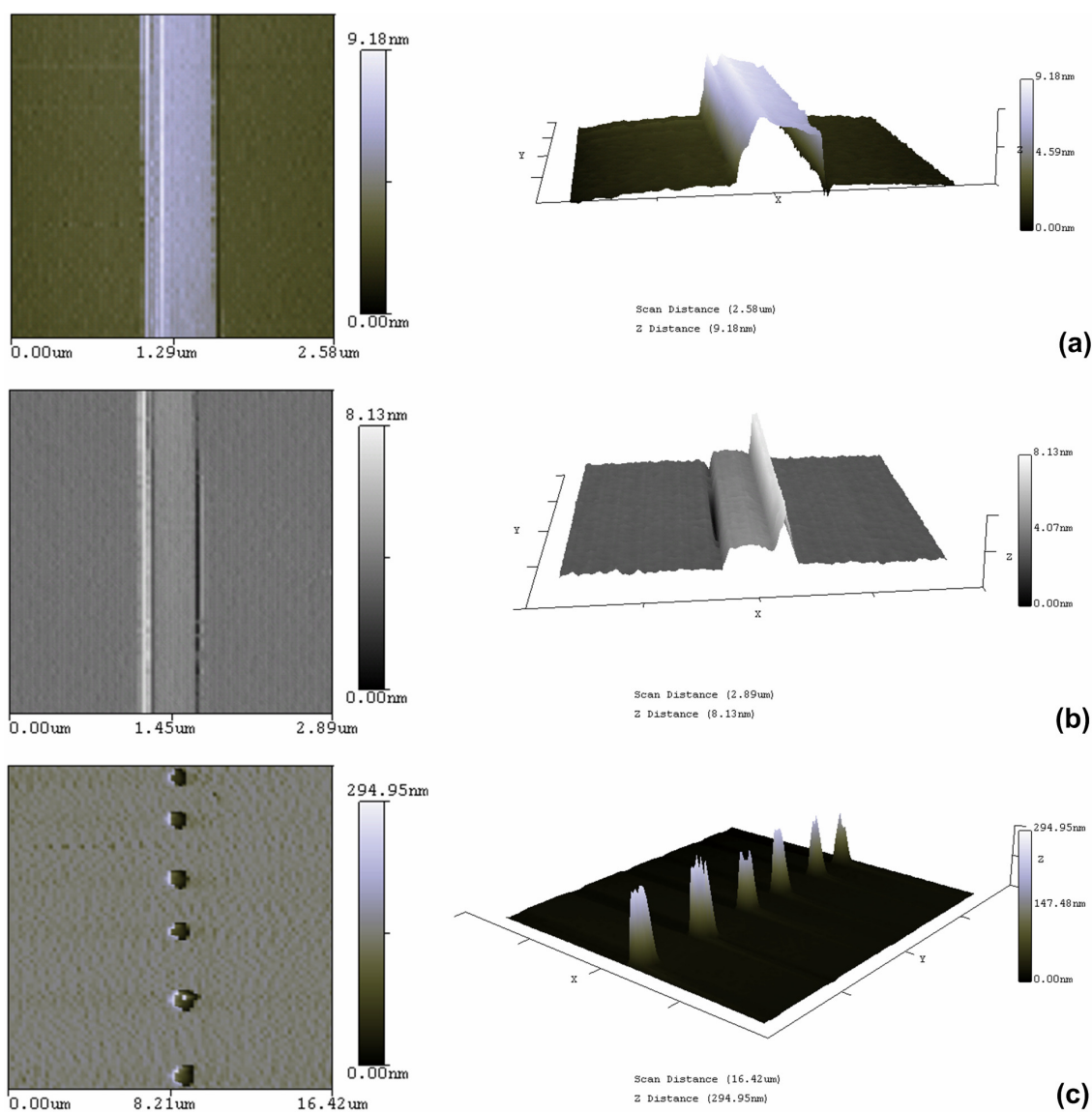


Figure 32. Computer images reconstructed from AFM measurement results showing the formation of metallic gold structures as a result of direct “write” on a silicon substrate: (a), (b) AFM images of gold lines (linewidths of ~ 600 nm and ~ 400 nm, respectively); (c) AFM image showing the rare case where dots were formed (diameter ~ 650 -900 nm).

4.5 Conclusions

The direct “write” of metallic structures using specially fabricated scanning probes with refined and more uniform tip radius of curvature was achieved. The results show that scanning probes can be directly used to promote material transfer and generate metallic structures with dimensions in the sub-micron scale. It is believed that the feature size of the structures created by this new method can be further reduced to nanoscale once the writing conditions (speed, contact force, temperature, etc.) as well as the probe design, fabrication and tip-substrate contact conditions are further optimized. Future work should be directed towards optimizing the writing conditions and investigating the properties of the directly-written structures to gather information on their electrical conductivity, hardness, surface roughness and adhesion forces.

CHAPTER V

SCANNING PROBES WITH PRECISELY DEFINED TIP CONTACT AREAS FOR SCANNING PROBE LITHOGRAPHY

5.1 Introduction

Recently, scanning probe (SP) instruments, such as the atomic force microscope (AFM) have developed into potential platforms for lithography applications [57, 77-79]. Most current scanning probe lithography (SPL) processes were demonstrated using commercially available scanning probes originally designed for imaging applications. Although the sharp probe tip (with a contact area of a few nm in diameter) facilitates the generation of nanoscale patterns, it will be time-consuming and inefficient to use them to fill in large-size microscale patterns, which are otherwise necessary for the functioning of many nano and micro devices. This situation creates a bottleneck issue in applying SPL in real device fabrication. To address this issue, a hybrid approach to combining SPL with other direct micropatterning techniques (e.g. microcontact printing and ink-jet printing) could be used to achieve a more effective and efficient lithography process. However, one potential issue of such an approach would be the increased complexity, non-uniformity and difficulty in alignment and registration due to the involvement of multiple pieces of equipment and processes. Therefore, it is highly desirable to use an array of scanning probes consisting of both “sharp” and “blunt” tips with different contact area to achieve variable-resolution SPL process (figure 33). This will allow both “coarse” and “fine” patterning to be achieved on the same platform and ensure the simplicity, uniformity, controllability and registration of patterning process, which will be especially useful for research and prototyping applications. In addition to SPL applications, “blunt” scanning probes with different tip contact areas or radii of curvature are also useful in various biological studies to investigate the mechanical behaviors of cells under different loading conditions [80-83].

However, existing probe fabrication techniques are not capable of batch fabricating such probe arrays in a controllable and repeatable manner, due to the

involvement of non-uniform and time-dependent processing steps. To fabricate “blunt” probe tips, different micromachining processes have been investigated (figure 34). The first approach utilizes isotropic silicon etching (plasma or wet etching) to form the probe tip underneath a silicon oxide mask (figure 34(a)) [84-86]. Instead of isotropic etching, the second approach uses anisotropic wet etching to create the probe tip (figure 34(b)) [87-89]. In the third one, trapezoidal cavities are first created in {100} silicon wafer with anisotropic wet etching and later used as molds for probe tip formation (figure 34(c)) [90]. To form a “blunt” probe with a desirable contact area, all the above approaches require a precise timing of the etching process, since an under-etching or over-etching will result in larger or smaller contact area. In the extreme case of over-etching, the silicon mesa structure for probe tip formation can be completely etched away (in the first two approaches) or trapezoidal cavities will become pyramidal ones (in the third approach). Unfortunately, both isotropic and anisotropic wet etching are affected by various etching conditions and thus the corresponding etch rates are quite non-uniform. During etching, the etch rate would vary significantly from time to time and from one location to another making it extremely difficult to apply the above fabrication techniques for efficient batch fabrication.

In this section, the development and application of a novel micromachining technique based on SOI (silicon-on-insulator) substrates is reported. The new technique eliminates the need for time-dependent etching steps and thus allows simultaneous formation of both “sharp” and “blunt” scanning probe tips (with precisely defined contact areas) with excellent uniformity and repeatability. To demonstrate its application in variable-resolution SPL, prototype scanning probe arrays have been successfully fabricated and used to directly “write” fluorescent line patterns with different linewidths in a parallel mode.

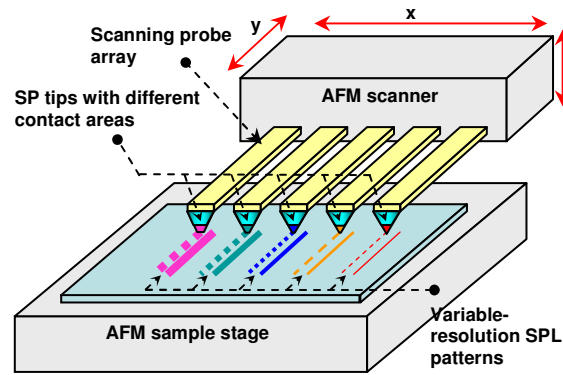


Figure 33. An illustration of variable-resolution SPL process using an array of both “sharp” and “blunt” probes.

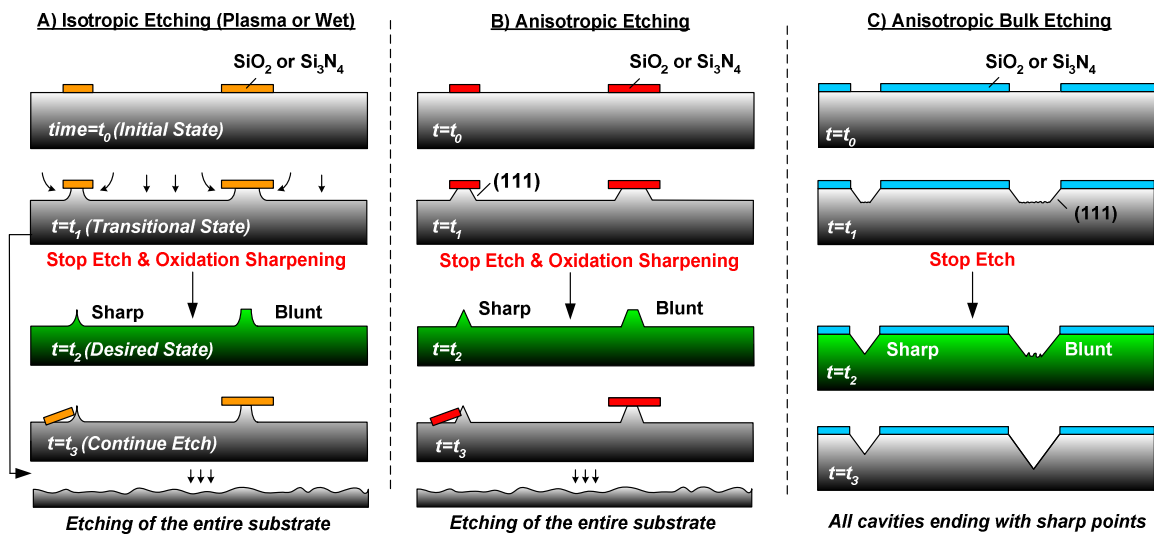


Figure 34. Summary of existing micromachining processes to realize “blunt” tips.

5.2 Principle and Validation

The new micromachining technology for both “sharp” and “blunt” probe tip formation is illustrated in figure 35. A {100} surface oriented SOI wafer is used as the fabrication substrate. A typical SOI wafer consists of a bulk silicon layer (handle layer, 300 ~ 500 μm thick), a thin single crystal silicon layer with a thickness ranging from one

tenth of a micron to a few microns (device layer), and a buried silicon oxide (BOX) layer sandwiched between. First, a thin layer of silicon oxide is thermally grown on the SOI substrate, which serves as an etch mask for silicon anisotropic wet etching. Instead of silicon oxide, other effective protective materials (e.g. silicon nitride) can be used as well. After oxide growth, photolithography and oxide etching are conducted to “open” square “windows” (aligned to crystal direction $\langle 110 \rangle$) with different size (w) (figure 35(a)). Next, silicon anisotropic wet etching is carried out to form cavities in the device (silicon) layer. The anisotropic wet etching mainly proceeds in the $\{100\}$ planes while it is negligible in the $\{111\}$ planes. Depending on the window size (w), and the SOI device layer thickness (t), the etching will terminate either in the device layer forming a stable pyramidal cavity with an end point, or on the top surface of the BOX layer, which results in a trapezoidal cavity with a flat bottom square area (figures 35(b) and (c)).

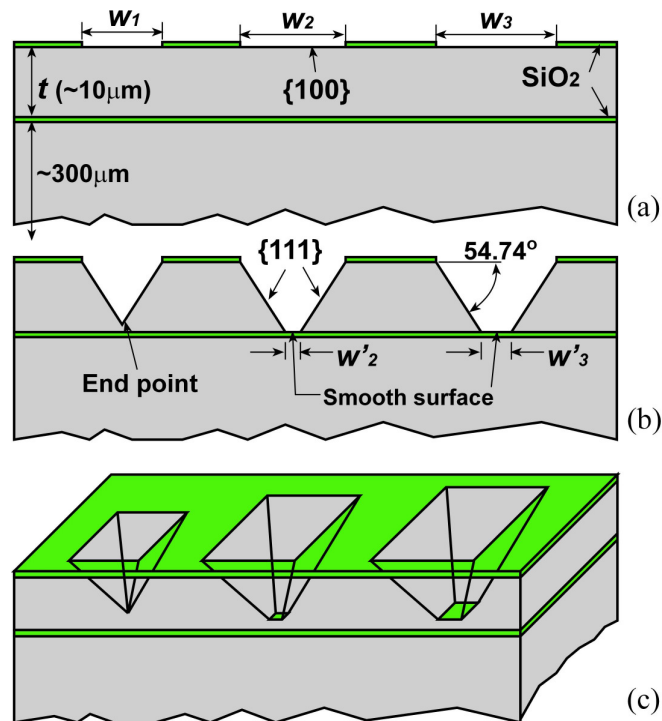


Figure 35. An illustration of the controllable process for the formation of variable sized cavities based on bulk micromachining of an SOI wafer.

Once either of these two situations is reached, the wet etching in these cavities will be self-terminated and the profile of the formed cavities will become stable and resistant to over-etching. Therefore, even though the anisotropic etching is a highly non-uniform process, all the needed cavities (either pyramidal or trapezoidal) even on a large substrate can still be readily formed simply by conducting the etching process long enough to ensure the etching in all the formed cavities is complete.

Considering that the $\{111\}$ planes form a 54.74° slope with the $\{100\}$ planes, the size of the bottom area of etched cavities (w') can be simply determined as:

$$w' = w - 2t / \tan 54.74^\circ \quad (1)$$

Using these cavities as molds, scanning probe tips with uniform profile and precisely defined contact area can be readily batch-fabricated. From Equation 1, a positive value of w' means a flat tip, while a negative or zero value of w' represents a sharp tip. Therefore, once the SOI substrate is chosen (with a given device layer thickness of t), any value of the probe tip contact area can be simply achieved by choosing a desirable size of the etch window (w) in the mask layout design.

To verify the above concept, anisotropic wet etching experiments were conducted using a $\{100\}$ SOI wafer with a 10- μm -thick device silicon layer. The size (w) of the oxide mask windows for cavity etching ranged from 11 μm to 20 μm with a 1 μm increment. According to equation 1, mask openings that are greater than $\sim 14.14 \mu\text{m}$ would result in the formation of trapezoidal cavities (thus blunt tips), while openings smaller than 14.14 μm would result in the formation of pyramidal cavities (thus sharp tips). In the experiments, the time of the bulk etching was not tightly controlled, but was maintained long enough to ensure that all the cavities were properly formed. After the etching, all the formed cavities (after removing the oxide layer) were inspected under an SEM (scanning electron microscope) and the size of the bottom surfaces of the trapezoidal cavities (w') were estimated (figure 36). A more detailed description of the cavity fabrication is discussed in Section 5.3. The cavities were uniformly formed

across the entire wafer and a good agreement between the predicted and actual values of (w') was reached. For example, according to equation 1, a w of $20\text{ }\mu\text{m}$ will result in a w' of $5.86\text{ }\mu\text{m}$, which matches well with the actual value of $5.64\text{ }\mu\text{m}$ estimated from the SEM zoom-in images. The slight difference between the predicted and estimated values of w' is believed to be caused by process variations in different fabrication steps (e.g. mask making, lithography and etching) as well as errors in the estimation from the SEM images.

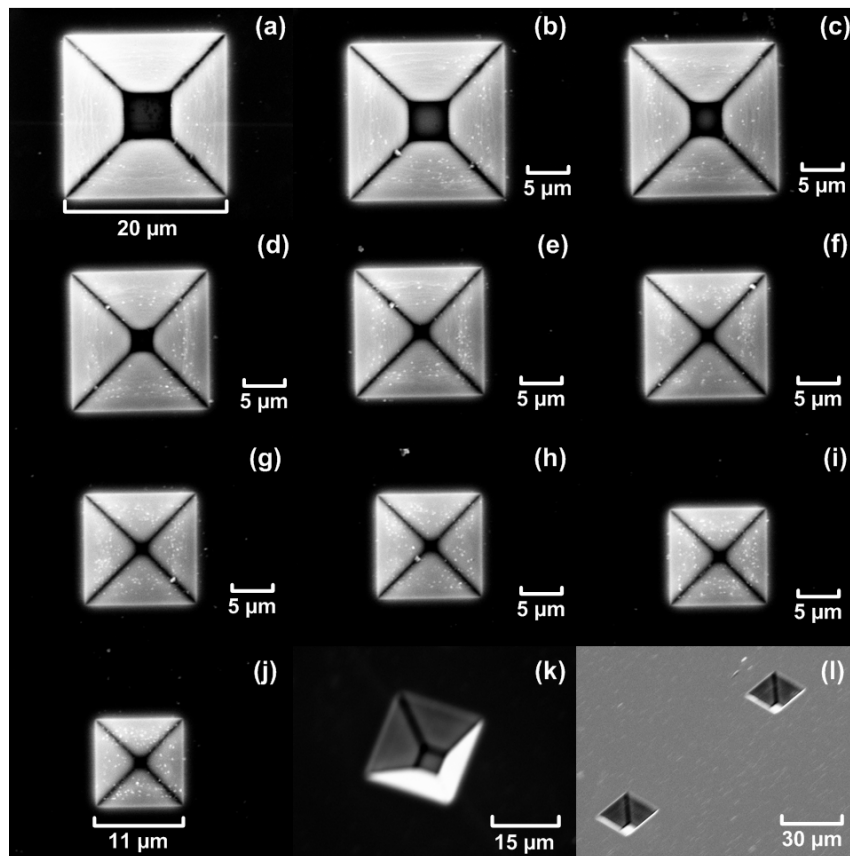


Figure 36. Scanning electron micrographs of bulk etched cavities in a $\{100\}$ SOI substrate. Inset (a) shows the cavity with the largest window opening ($20\text{ }\mu\text{m}$) and a flat square base, whereas inset (j) is the cavity with the smallest window opening ($11\text{ }\mu\text{m}$) and a sharp endpoint, from (a) to (j) window opening decreases by $1\text{ }\mu\text{m}$ in each cavity. Inset (k) and (l) show perspective views of the cavities.

5.3 Fabrication of Scanning Probe Array with Different Tip Contact Area

Based on the new scanning probe tip formation technique, prototypes of a new scanning probe array were successfully fabricated, in which each probe has a different but precisely defined tip contact area. The entire probe fabrication process consists of the following three steps: a) Create the tip-molding cavities on an SOI wafer; b) Deposit and pattern the sacrificial and structural materials for the scanning probe; and c) Remove the sacrificial layer and transfer the entire probe array onto its handle structure (figure 37). For probe fabrication, chromium, gold and SU-8 (MicroChem, MA) were chosen as the materials for the sacrificial layer, the probe structure and probe handle layer, respectively. Their deposition and patterning can be readily achieved using simple and room-temperature processes, which would result in quick fabrication. Moreover, conductive scanning probes fully or partially made of metal materials would be very useful in characterizing surface electrical properties [91]. On the other hand, the above probe fabrication process based on a “mold-transfer” approach can readily accommodate a wide range of materials for probe fabrication, including silicon nitride, different metals and polymers [92].

5.3.1 Tip Formation

Figures 37(a) and (b) show the fabrication steps to create the pyramidal and trapezoidal cavities as the molds for forming scanning probe tips with different contact area. Since the total time for the anisotropic wet etching is usually 10 ~ 20 minutes, a thin layer of silicon oxide (100 nm thick) grown with dry oxidation is used as the etch mask material. The wet etching was then conducted in EDP (ethylene diamine pyrocatechol) due to its almost negligible etch rate on silicon oxide. After the cavities are formed, the oxide layer is no longer needed and should be removed before the probe structure can be properly fabricated.

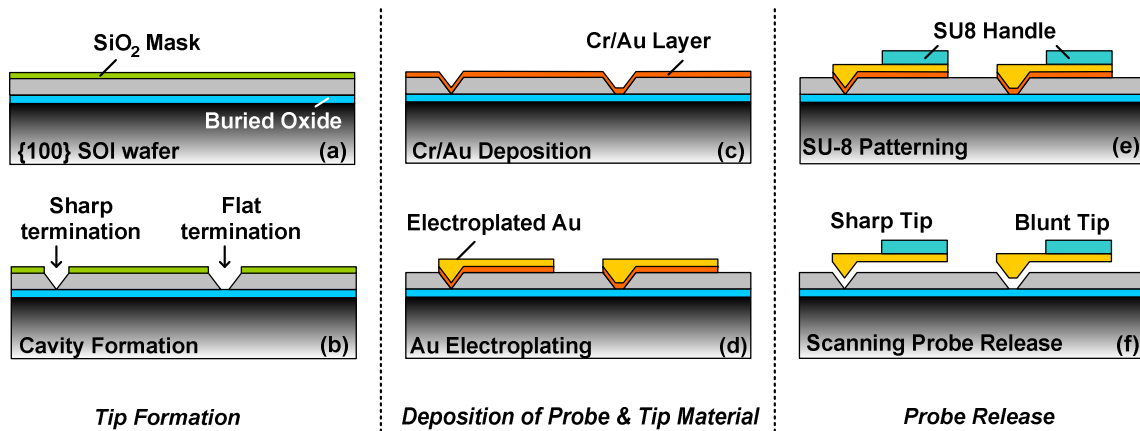


Figure 37. An illustration of the fabrication process for scanning probes with different contact areas. The process flow is divided into three steps: (1) tip formation where variable sized cavities for tip molding are precisely defined, (2) deposition of the desired probe and tip materials, and (3) the probe release by sacrificial layer etching.

Due to the proximity effect in photolithography, the patterned square etch windows in oxide layer usually assume rounded corners. Figure 38 illustrates the top and cross sectional views of an etched cavity with an overhanging oxide layer. As shown in the cross sectional view, if not removed, the oxide layer will become an unwanted locking mechanism, which will prevent the “release” of fabricated probe structures from the mold wafer and “transfer” to the handle wafer during the last step of probe fabrication. However, for oxide removal an immediate immersion into an oxide etchant is not desirable since it will also damage the exposed BOX layer in the trapezoidal cavities. To ensure the integrity of the etched cavities, the BOX layer has to be fully protected during the oxide etching.

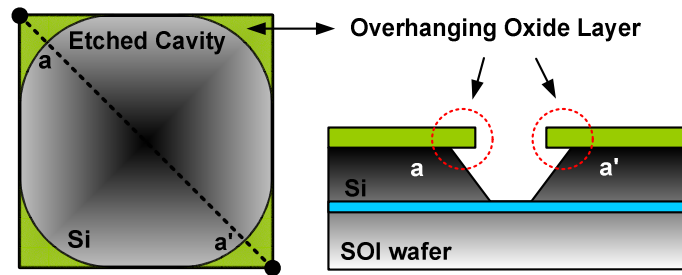


Figure 38. An illustration of the top and cross sectional views of an etched cavity. Due to possible rounding of sharp corners during lithography, an undesired overhang of the oxide layer over the silicon cavities is possible. Removal of the oxide layer is necessary to prevent probe lock-in during the release step.

To address this issue, a straightforward and effective solution was developed where the etch cavities were filled with spin-on photoresist (figure 39). As shown in figure 39(a), a layer of positive-tone photoresist was first spun onto the SOI wafer with etched cavities. As long as the photoresist can properly fill in the cavities, a low-viscosity photoresist and a fast spin rate should be used to minimize the thickness of the photoresist layer on the flat oxide etch mask. We used AZ 5214 photoresist and a spin rate of 6000 rpm, which resulted in a final thickness of around 1 μ m on the flat oxide etch mask surface. After soft baking, a flood exposure of the photoresist was conducted with a dosage slightly higher than that recommended by the manufacturer for a 1- μ m-thick photoresist layer. After the exposure, a full development was conducted to completely dissolve the photoresist layer on the flat oxide etch mask (figure 39(b)). For the much thicker photoresist filling in the cavities, this exposure and development only removed the top surface layer, while leaving the exposed BOX layer completely covered. After the development, the oxide etch mask was completely stripped in a BHF (buffered hydrofluoric acid) solution (figure 39(c)). A scanning electron micrograph of the photoresist filled cavities after BHF etching is shown in figure 40.

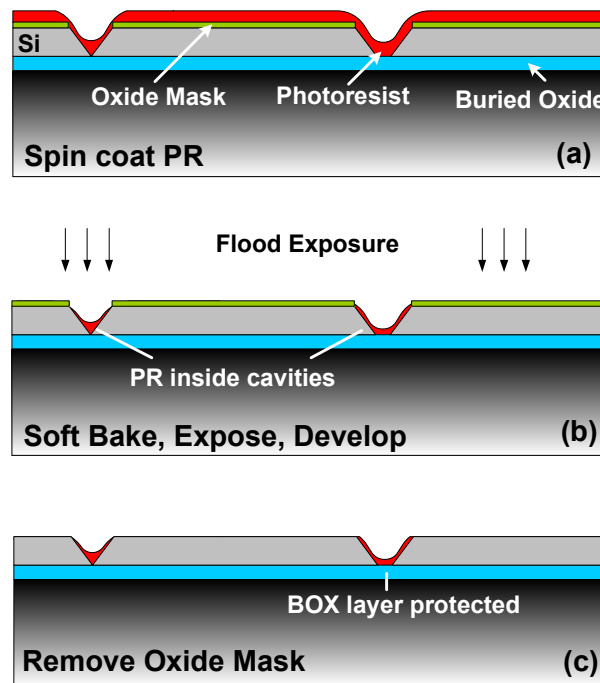


Figure 39. Process flow diagram outlining the maskless photoresist filling of the cavities before oxide removal.

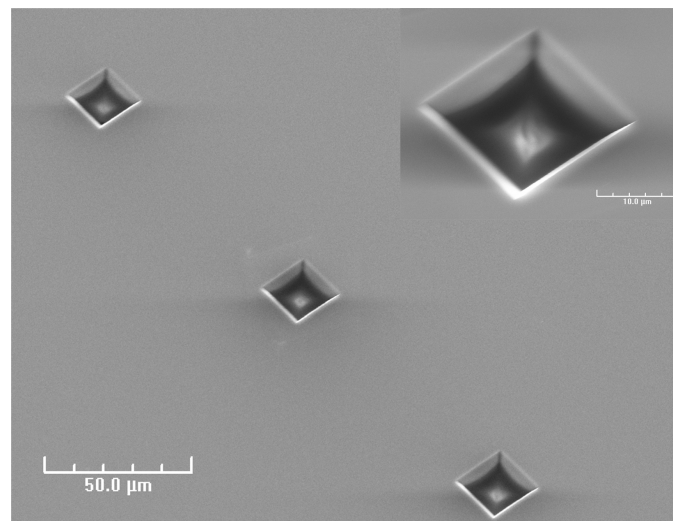


Figure 40. Scanning electron micrograph of photoresist filled cavities using the maskless photoresist filling technique.

5.3.2 Deposition and Patterning of Probe Structures

After the cavities were formed and oxide mask was removed, the desired material for making the scanning probes can be deposited. First, a thin chromium/gold layer (Cr/Au: 25/250 nm) was deposited using thermal evaporation (figure 37(c)). The chromium layer serves both as an adhesion layer and as the sacrificial layer for the final release step. Next, AZ 5214 photoresist was spin coated (2000 rpm, 30sec) and patterned to provide a 2 μm thick mold, which was followed by sulfide-based gold electroplating using a commercial plating bath (Type TFA, Transene Company, MA). Electroplating was conducted for 70 minutes at a current density of 5 A/m^2 , resulting in an average plating rate of $\sim 1.7 \mu\text{m}/\text{hr}$ and a final gold layer of thickness $\sim 2 \mu\text{m}$. After electroplating, the photoresist mold was removed and the gold seed layer outside the electroplated area was etched away to define the cantilever beam structures of the scanning probes (figure 37(d)). To fully protect the electroplated gold structure during seed layer etching, a layer of patterned photoresist was used as an etch mask.

5.3.3 Probe Release and Transfer

Before “releasing” the scanning probes from the SOI mold wafer, special “handle” structures (made of 50 μm -thick SU-8 resist) were patterned for easy manipulation and use of the fabricated scanning probes (figure 37(e)). Following the SU-8 handle formation, all the fabricated probe structures were released by sacrificial layer etching of the thin chromium layer, which does not affect either of the SU-8, gold structural layers or the SOI mold wafer, which can be readily re-used for next run of fabrication (figure 37(f)). Scanning probes with a fixed width of 55 μm and different cantilever lengths (from 275 to 475 μm) were fabricated (figure 41(a)). Figures 41(b) and (c) show the zoom-in microscopic pictures of a fabricated scanning probe array with 10 probes and cantilever length of 425 μm . Based on the fixed-free cantilever beam model, the force constant (k) of the scanning probe can be estimated as $k = E \cdot wt^3/4l^3$, where E , w , t and l are the Young’s modulus, width, thickness and length of the cantilever. Using a Young’s modulus of 41.9 GPa for the electroplated gold thin film

[93], the force constant of the fabricated probes are determined to range between 0.04-0.22 N/m, providing “soft” cantilevers suitable for various SPL processes usually conducted on a flat surface in contact mode. To verify the proper formation of the probe tips, the fabricated scanning probes were also inspected under a scanning electron microscope. Figure 42 shows the close-up views of the tips in the scanning probe array shown in figure 41(c), which were molded from the same group of cavities shown in figure 4. Figures 42(b)-(g) show the “blunt” tips with a contact area ranging from 5.6 to 0.8 μm , while figures 42(h)-(k) show the “sharp” tips $\sim 200\text{ nm}$. The close match of the probe tip profile to that of the mold cavities indicates the successful implementation of the probe fabrication.

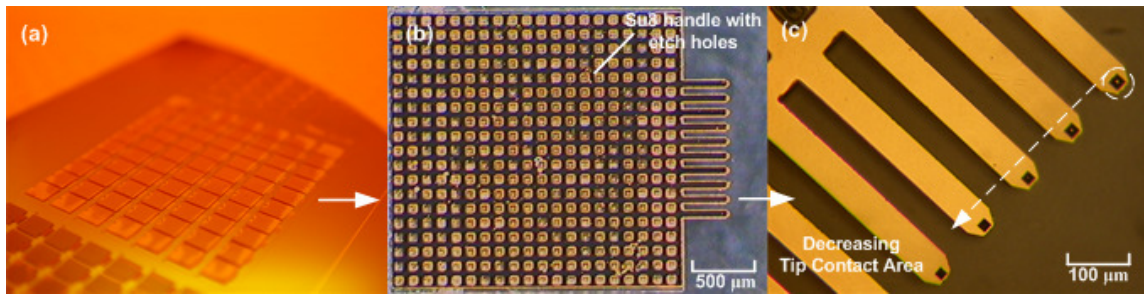


Figure 41. Optical microscopic images of fabricated scanning probe arrays: (a) Scanning probe arrays (7×10) on SOI substrate before release; (b) A released scanning probe chip with SU-8 handle; (c) A zoom-in view of the probe array showing the details of the probe tips.

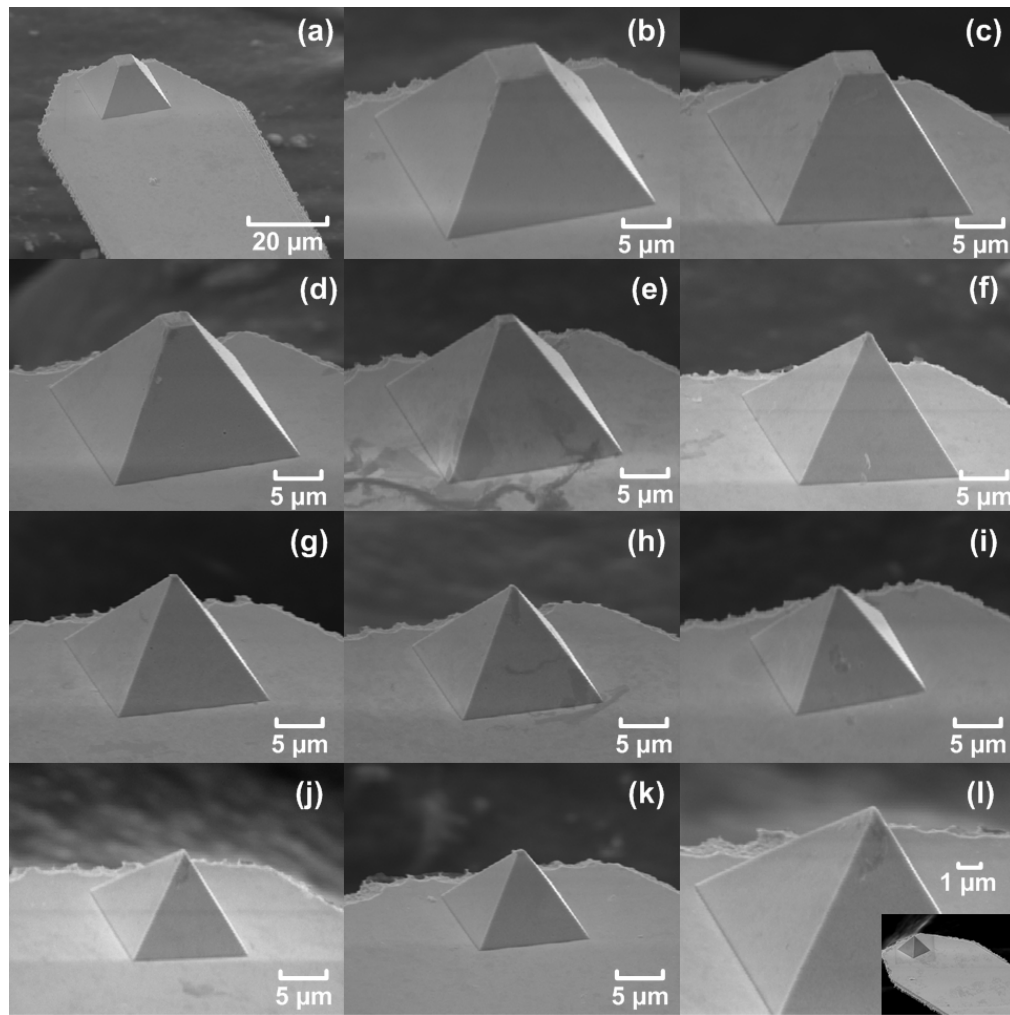


Figure 42. Scanning electron micrographs showing the controllable fabrication of scanning probe tips with precisely defined tip contact area. Inset (a) shows the probe with the bluntest tip, and inset (l) shows the sharpest probe. Insets (b)-(k) show the close-up views of each tip in the fabricated scanning probe chip consisting of 10 cantilevers. The tip contact area decreases from $5.6 \times 5.6 \mu\text{m}^2$ in (b) to $0.8 \times 0.8 \mu\text{m}^2$ in (g) and then remains almost the same through sharper tips $\sim 200 \text{ nm}$ in (h)-(k).

5.4 Demonstration of Variable-Resolution SPL

Using the fabricated gold scanning probe array with different probe-tip contact area, the proof-of-concept of parallel SPL with variable pattern resolution was successfully demonstrated. A commercially available DPN (dip-pen nanolithography) system “NSCRIPTOR” (from Nanoink Inc., Chicago, IL) was used with the probe array for the demonstration. In DPN, the sharp tip of a scanning probe is first coated with the chemical for patterning (“ink”). Under certain temperature and environmental humidity conditions, contacting an inked probe tip onto a suitable substrate allows ink molecules to diffuse from the probe tip onto the substrate surface at the point of contact through the water meniscus formed in between [59, 94]. Using a standard atomic force microscope (AFM) or a specialized DPN system to control the scanning of the probe, different line patterns can be directly “written”. Like any other SPL process, DPN is suitable for the generation of nano scale dot or line patterns. However, when micro scale block patterns are needed, a long raster scanning will be necessary to fill the whole pattern, which would result in a very low efficiency and throughput. Therefore, it is highly desirable to have the multiple linewidth (resolution) capability for efficient generation of both “coarse” and “fine” patterns.

For DPN, the ink transportation is affected by a number of experimental conditions, including temperature, humidity and probe scanning speed, which can serve as “control knobs” for obtaining increased linewidth [95, 96]. For example, raising the temperature and humidity facilitates ink diffusion on the writing surface, thus resulting in larger linewidth. Meanwhile, reducing scanning speed can generate wider patterns, since the ink diffusion is enhanced by a longer probe dwelling time. However, using the above “control knobs” to achieve different linewidths has several inherent drawbacks. First, ramping up or down the temperature and humidity is a slow process, which does not provide the needed fast response time. The resulting effects also depend on the ink and substrates, which will need an intensive calibration process. Second, changing the scanning speed would result in extremely long writing process. Third, all these take effect on all the scanning probes in the array. Different linewidths cannot be achieved simultaneously in parallel writing using

arrayed probes with same tip profile. Therefore, the ultimate solution is to control the tip-substrate contact area, which is a direct factor that affects the pattern linewidth or resolution.

To demonstrate multiple-resolution DPN, the fabricated gold probe array (shown in figures 41(b) and (c)) was first inked with Rhodamine-B fluorescent dye. A “dip-inking” method was used, in which the probe array was immersed into Rhodamine-B ethanol solution for 20 seconds [97]. The Rhodamine-B concentration of the solution is 4 mg/ml. After the dipping, the probe array was gently blown dry with nitrogen to remove excess dye solution. To ensure that the probe tips were fully coated with Rhodamine-B, the probe tips before and after the inking were carefully inspected under an optical microscope and a confocal microscope, respectively (figures 43(a) and (b)). For the patterning substrate, a thin glass cover slip (from VWR, West Chester, PA) was used after a thorough cleaning cycle in acetone, isopropyl alcohol, DI water and methanol. Figure 43(c) shows the experimental setup used in DPN patterning with the probe chip and substrate mounted in place and the laser beam aligned on a cantilever for contact feedback. After lowering the stage to contact all the probe tips on the glass substrate (with a contact force $\sim 0.1\text{ nN}$) line patterns were written by programming the system control software under different conditions (humidity and writing speed). The ambient temperature is kept constant at 25°C . Immediately after the writing, the generated patterns were inspected with a Leica® (TCS SP5) confocal microscope. Figure 44 shows the successful parallel-mode patterning of multiple resolution lines on a glass substrate with a variable contact area probe array under an environmental humidity of 30 % and a writing speed of $0.1\text{ }\mu\text{m/s}$. The fluorescence images reveal 4 lines with different widths (from approximately $1\text{ }\mu\text{m}$ to $4\text{ }\mu\text{m}$), which were created by 4 different probes with tip contact areas ranging from $0.8\text{ }\mu\text{m}^2$ to $3.8\text{ }\mu\text{m}^2$ respectively. In figure 44, it is seen that the patterned lines show slight fluctuations in fluorescence intensity. We believe that the fluctuation in the linewidth is mainly caused by the possible inconsistent diffusion of rhodamine-B molecules on the patterning surface. First, low-grade cover glass slips were used as the patterning substrate whose surface conditions might not be quite uniform. Second, due to its relatively small molecular weight and lack of SAM

(self-assembled monolayer) formation, rhodamine-B molecules tend to diffuse more randomly on the glass substrate. On the other hand, using fluorescent “inks” eases the measurement and characterization of the written patterns. By choosing a better combination of the “ink” and substrate and optimizing the patterning condition, a more uniform linewidth can be achieved.

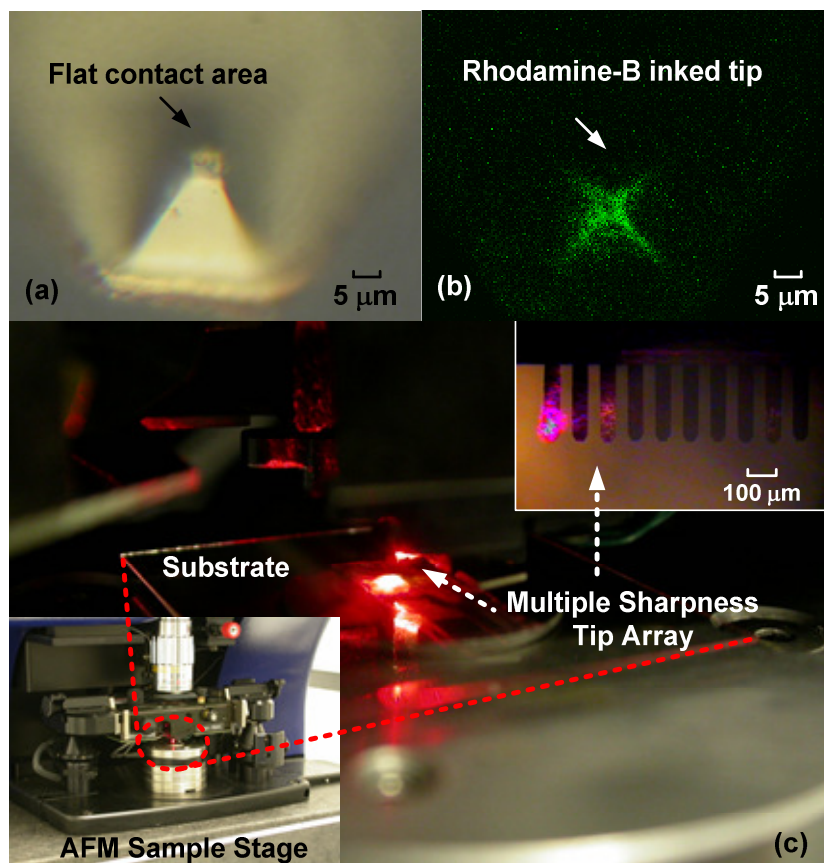


Figure 43. (a) Optical microscopic image of a “blunt” gold probe tip with flat contact area before inking; (b) Fluorescence image of the probe tip after inking with Rhodamine-B dye; (c) Experimental setup employed in patterning experiments.

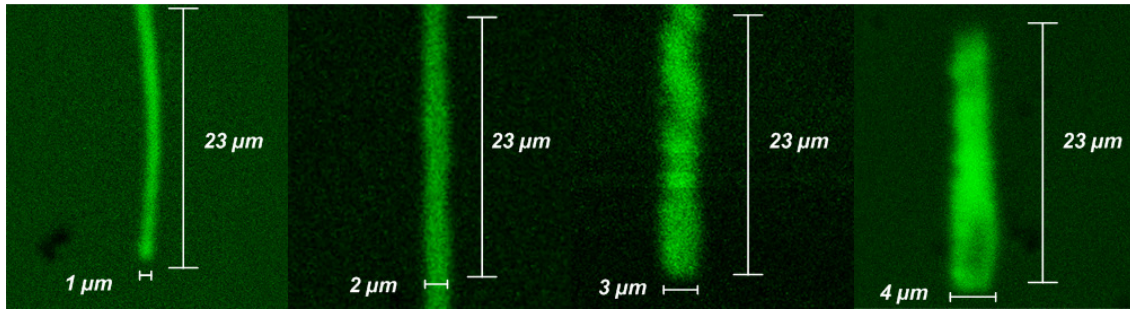


Figure 44. Rhodamine-B patterns with different linewidths created simultaneously by the gold probe array.

5.5 Conclusions

A new scanning probe fabrication technology was developed, which utilizes bulk-etched cavities in {100} SOI substrates as molds for probe tip formation. Different from conventional {100} silicon substrates where only stable pyramidal cavities can be obtained, the unique sandwich structure of SOI substrates enables controllable formation of not only pyramidal but also trapezoidal cavities. As a result, scanning probes with desirable “sharp” or “blunt” tips can be readily batch-fabricated. The overall “mold-transfer” strategy of probe fabrication allows the re-use of the SOI mold and also accommodates a wide range of structural materials, which leads to an efficient, low-cost, and versatile fabrication process. The ability to create scanning probes with different contact area in arrayed format is expected to significantly improve the efficiency and throughput of various SPL process by realizing parallel and variable-resolution “writing” modes.

CHAPTER VI

MICROFABRICATION OF COLLOIDAL SCANNING PROBES WITH DIFFERENT TIP RADII OF CURVATURE

6.1 Introduction

Apart from imaging purposes scanning probes have started to be used in many exciting nano and biotechnology applications, ranging from scanning probe lithography (SPL) [57] to applications in cell mechanics, cell adhesion [98-103] and for the analysis of interaction, adhesion forces between particles and surfaces (also referred to as Colloid Probe Atomic Force Microscopy) [104-109]. However, many of these applications are largely limited by commercially-available scanning probes with only sharp tips, which are not very desirable for the above mentioned nano biotechnology applications.

1) In SPL, when larger size, microscale block regions are to be patterned (for instance micro scale interface pads for a nano size sensor element), it would be impractical and time-consuming to use sharp tips. Therefore, it is highly desirable to use an array of scanning probes consisting of both “sharp” and “blunt” tips with different radius of curvature to achieve variable resolution SPL (figure 45(a)).

2) In case of biological applications, sharp tips can penetrate through the cell during measurements [110], which result in misleading data and also rupture of the cell (figure 45(b)). Using rounded, spherical tips a lot less damage is incurred on the cells, and measurements can be done within the narrow time frame where cells are alive in the solution [81].

3) In case of Colloid Probe AFM, the tip geometry has to be well known and uniform for ease of comparison of measurement results with theory [111]. Usually the Derjaguin approximation is used to relate the energy per unit area between two planar surfaces into corresponding values when the geometries are arbitrary (e.g. energy or force between a round object and a flat surface). However, this approximation is valid only when the tip radius of curvature (r) is much greater than the interaction distance (d)

[112] (figure 45(c)). Therefore, measurement results with sharp tips are not always reliable.

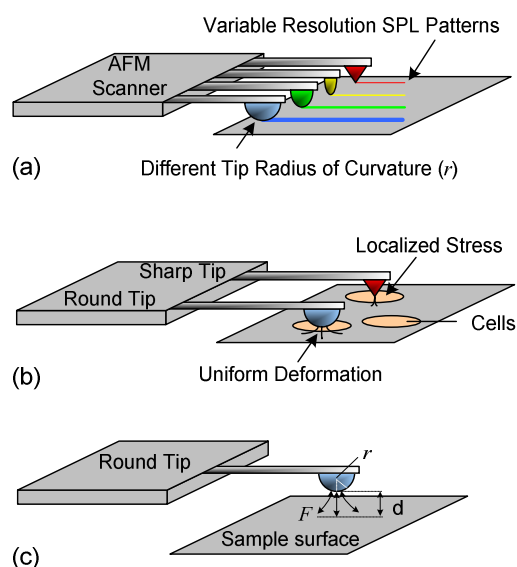


Figure 45. Illustration of the applications of colloidal probes: a) Scanning probe lithography; b) Cell studies; and c) Measurement of surface interfacial forces.

To circumvent the limitations posed by sharp tips, different methods have been investigated to control the tip radius of curvature and obtain probes with round, curved tips. Several groups have referred to such curved-tip probes as *colloidal probes* although the tip was not necessarily a colloid; the same convention will be used.

The most widely used method to obtain a round probe tip, is the microsphere attachment method (figure 46(a)). While measuring colloidal forces, Ducker et al. first proposed the idea to use spherical particles or colloids (e.g. silica, glass, polystyrene) of uniform dimensions (1-50 μm) and smooth surface as the probe tip [80]. However, this is a tedious, difficult and infeasible approach as spheres have to be manually glued to the distal end of a cantilever one by one using micromanipulators while viewed under an optical microscope. Care must be taken in not spilling glue on the sphere surface [112], and accurately positioning the sphere in the correct location every time. Therefore, the

reliability and repeatability of sphere attachment is not standard. A recent review on microsphere attachment techniques can be found at [113].

In search of finding alternatives to microsphere bonding, several groups tried different methods of modifying sharp AFM tips into round tips of uniform radius of curvature. These include, thermal oxidation of silicon tips [114, 115] (figure 46(b)), physical or chemical vapor deposition on tips [116, 117] (figure 46(c)), and chemical etching of silicon using an isotropic etchant composition (HNA= $\text{HF} + \text{HNO}_3 + \text{CH}_3\text{COOH}$) [118] (figure 46(d)). However, in thermal oxidation the oxide growth is diffusion limited [119] and the maximum achievable SiO_2 thickness is limited to $\sim 1\text{-}2\ \mu\text{m}$ [120], so is the tip radius of curvature. Similarly, the material thickness achieved by deposition techniques (evaporation, sputtering, chemical vapor deposition) is time-consuming and therefore limited due to practical reasons. On the other hand, isotropic etching method depends solely on critical timing of a transient chemical etching process, and makes it difficult to control the tip radius of curvature.

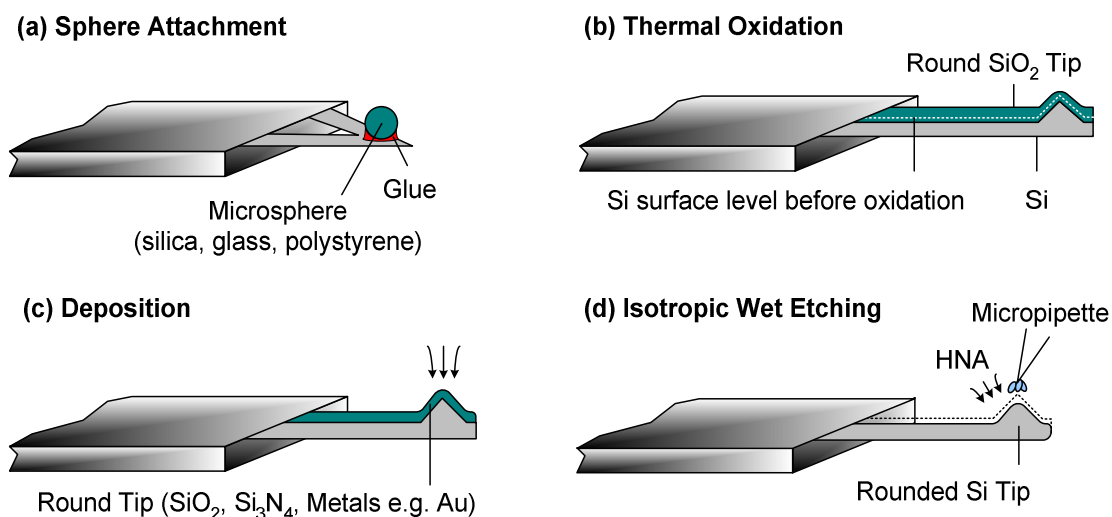


Figure 46. Existing colloidal probe fabrication methods: a) Microsphere attachment; b) Oxidation of silicon tips; c) Thermal evaporation; d) Chemical etching.

None of the currently available methods present simple, batch-fabrication capability; neither they are capable of generating probes with a wide range of tip curvature. This chapter presents the first technique up to date that can controllably mass fabricate scanning probe arrays with well defined tip radius of curvature based on standard micromachining processes.

6.2 Process Principle

The bulk etching of silicon is a well-established process, and it is known that the (111) planes in silicon show strong anisotropy to certain etchants like KOH (potassium hydroxide), EDP (ethylene-diamene-pyrocatechol), TMAH (tetramethylammonium hydroxide). By using {100} surface oriented silicon wafers, stable pyramidal pits (inverted pyramidal cavities), trenches, and mesa structures have been formed and harnessed for many applications including scanning probe fabrication [121].

To effectively and easily mass-fabricate curved-tip probes, we have developed a new tip formation technology. The process is based on transforming silicon bulk-etched cavities with sharp terminations into cavities with round surface profiles. This is achieved by controlled filling of suitable materials (composed of a liquid solvent and a solid part) into sharp cavities. This process will be referred to as the *mould filling technique* for curved tip formation.

Mould filling begins with the formation of sharp cavities in silicon using SiO₂ as an etch mask and EDP as the etchant. For cavity formation silicon is first thermally oxidized to provide ~ 250 nm-thick SiO₂ layer and then patterned into square window openings after which bulk etching is conducted (figure 47(a)). In order to modify sharp cavity terminations into round profiles, a liquid filling material of certain viscosity is uniformly dispensed (figure 47(b)), and coated over the cavities using standard spin coating methods (figure 47(c)). After spin coating, the substrate is baked for further removal of the solvent and solidification of the coated material, rendering a stable round topography (figure 47(d)).

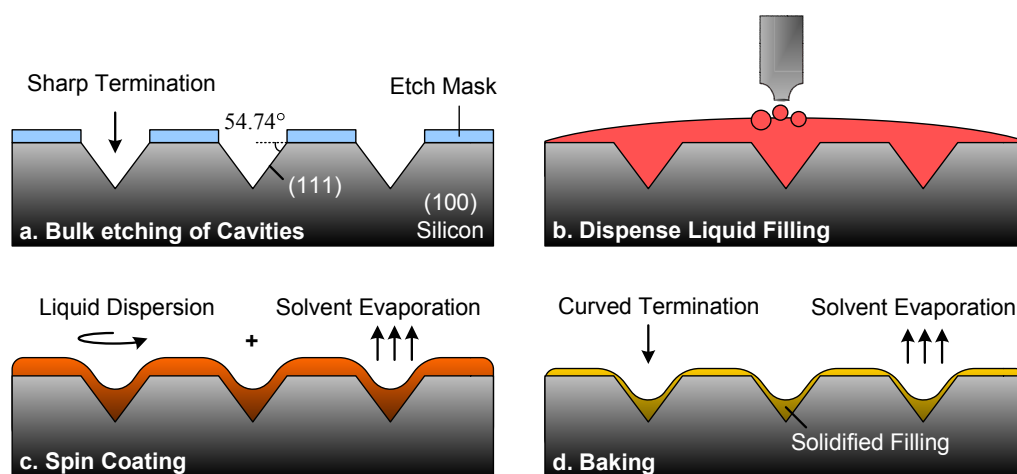


Figure 47. Illustration of the mould filling technique for transforming sharp end cavities into curved ones.

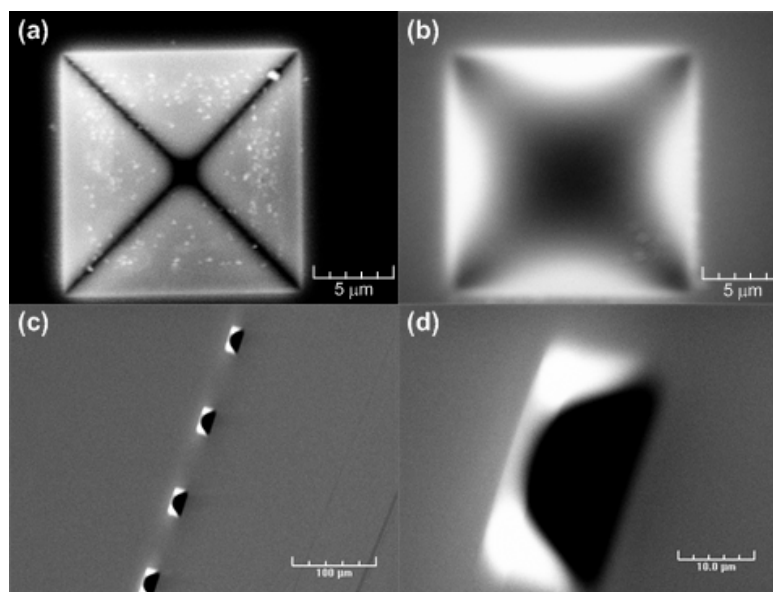


Figure 48. Scanning electron micrograph showing (a) bulk-etched cavity in silicon with a sharp termination versus cavities with curved, round ending, (b) top view; (c) 65° tilted view of multiple rounded cavities; (d) 65° tilted view of a single round cavity.

In order to test and verify the round cavity formation, the cavities were observed under a scanning electron microscope (SEM) before and after mould filling. Scanning electron micrographs indicate a clear rounding of the cavities with sharp terminations after the mould filling process. Figure 48(a) shows the top view of a bulk-etched cavity in silicon with a sharp end termination. However, after mould filling the top view and tilted views (figures 48(b)-(d)) of cavities indicate a clear rounding of the cavity terminations, confirming the suitability of the technique in achieving curved profiles.

There have been in-depth studies on the spin coating of materials over flat and topographical surfaces both for lithography and planarization applications [122]. It has been shown that several parameters will affect the final thickness and profile of the spin-on filling material. These parameters include, viscosity of the filling material, spin speed and duration, and baking conditions like temperature and time. During mould filling such processing conditions and material properties will be effective on the coating profile and thus the tip radius of curvature, which will be discussed in the next section.

6.3 Process Development and Validation

For curved-tip probe fabrication the first step is the mould filling of bulk-etched sharp cavities in silicon. Due its widespread use, photoresist was selected as the mould filling material and the filling technique outlined previously was followed. Spin speed of 4000 rpm for 30 seconds was used. To ensure the complete evaporation of the solvent (PGMEA: propylene glycol monomethyl ether acetate) inside photoresist, the substrate was first soft baked for 1 minute at 95°C on a hot plate, then hard baked for 4 hours in a convection oven at 135°C. After the photoresist is baked dry, its top surface will naturally assume a certain radius of curvature (figure 49(a)). This curved profile is then replicated into a stable metallic mould by evaporating a 200nm-thick layer of Aluminum (figure 49(b)). Using the curved metallic cavities, mould-transfer scanning probe fabrication is conducted to create probes with curved tips by deposition of the desired probe material (figure 49(c)). After successful patterning of the probe material, sacrificial layer etching is conducted to release the probe structures from the substrate

(figure 49(d)). The sacrificial layer removal is done by using diluted hydrochloric acid ($\text{HCL}:\text{H}_2\text{O} = 1:3$) for Aluminum etching. The etching is typically conducted for ~ 20 minutes at ambient temperature, and does not affect the probes or the underlying photoresist filling layer.

For process demonstration SU-8 was selected as the probe structural material since it can be readily patterned. However, by minor modifications in the fabrication process, the outlined technique can easily accommodate different structural materials for the probe such as metals or silicon nitride by using filling materials compatible with high temperature deposition processes (e.g. spin-on glass).

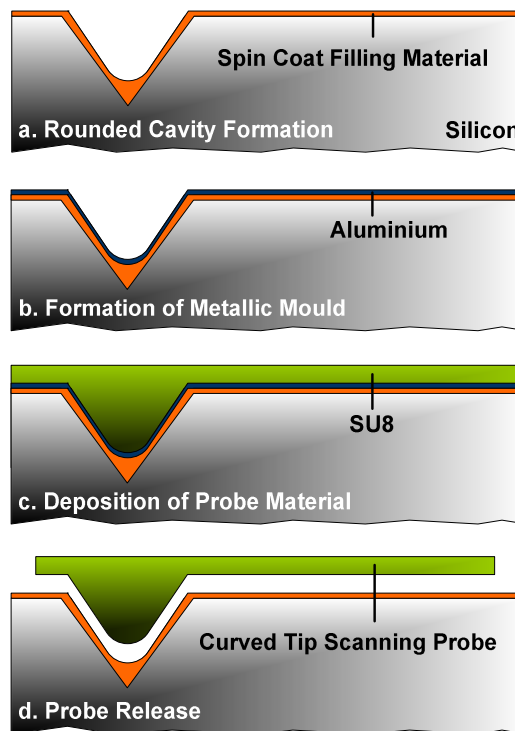


Figure 49. Fabrication process flow of scanning probes with curved tips.

Scanning electron micrographs in figures 50(a) and (b) shows images of a curved-tip probe chip after released from the substrate. Probes with a fixed width of 55 μm and different cantilever lengths (from 275 to 475 μm) were fabricated. The zoom-in

and sideview images of the tip reveal a well-defined, round tip profile (figures 50(c) and (d)). The force constant (k) of the scanning probe can be estimated as $k = E \cdot wt^3 / 4l^3$, where E , w , t and l are the Young's modulus, width, thickness and length of the cantilever. Using a Young's modulus of 2 GPa for SU-8, the force constant of the fabricated probes are determined to range between 0.09-0.45 N/m, providing “soft” cantilevers suitable for the intended applications.

The tip radius of curvature of the fabricated probe is directly affected by the volume of the filling material solidified inside the cavity after spin coating and baking cycles. This in turn is determined partly by the processing conditions (spin speed, baking conditions) and more importantly by physical properties of the filling material like the percent solid content and viscosity. In order to achieve probes with different tip radius either one of the properties in these two categories could be utilized. However, since it is harder to control processing conditions to vary the filling volume, we chose 1) to change material properties (% solid content) while keeping the processing parameters fixed at all times, 2) implement a multiple spin and bake approach to coat several “stacked” layers of filling material.

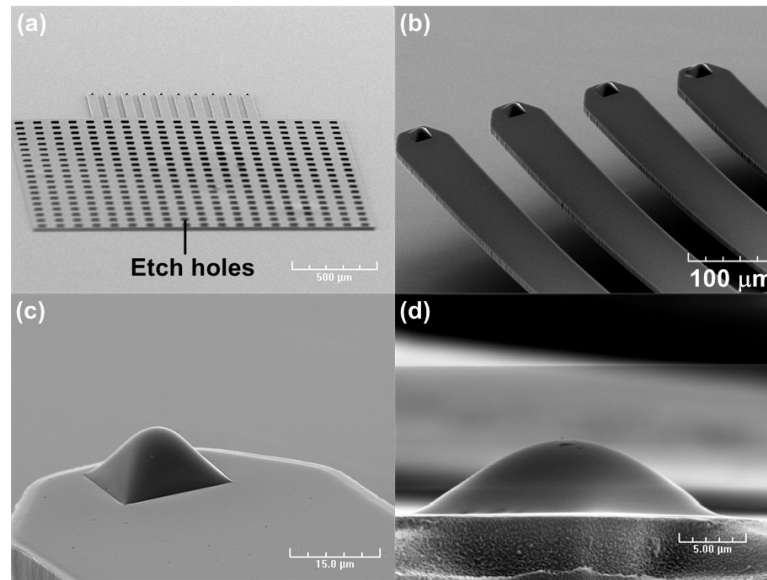


Figure 50. Scanning electron micrographs of a fabricated curved tip probe array.

6.3.1 Solid Content vs. Tip Radius of Curvature

Typically, standard photoresists are comprised of three parts which are the novalak resin, the photo active compound and the solvent. After spin coating and baking most of the solvent evaporates and the solids inside the photoresist are left behind. Therefore, the final volume of the material inside the cavity is directly affected by the solid content of the photoresist. To obtain the flexibility for creating different tip radius of curvature, the probe fabrication was conducted under different photoresist concentrations, that is by adding more solvent (PGMEA) to the original photoresist composition or diluting the photoresist. The photoresist concentrations that were used, and the corresponding amounts of solvent added in each case are summarized in Table 2. In this study, AZ 5214E photoresist from Clariant (Somerville, NJ) was used.

Table 2. Summary of the photoresist concentrations and the dilution amount required in each case.

AZ 5214E Amount	Initial Solvent (%)	Additional Solvent	Solid (%)
X (ml)	71.7 %	-	28.3 %
X (ml)	71.7 %	1/3 X	21.225 %
X (ml)	71.7 %	X	14.15 %
X (ml)	71.7 %	3X	7.075 %

Scanning electron micrographs of the fabricated probes under different PR concentrations are shown in figures 51(a)-(e). It is seen that the photoresist profile inside the cavity and therefore the tip radius of curvature is directly affected by the solid content of the spun photoresist. Therefore, the tip radius of curvature can be easily controlled by changing the photoresist concentration. The plot of the tip radius of curvature versus solid content shows that, the tip curvature ranges from ~ 250nm to 10.5 μ m with increasing PR content from 0% to 28 % (figure 52).

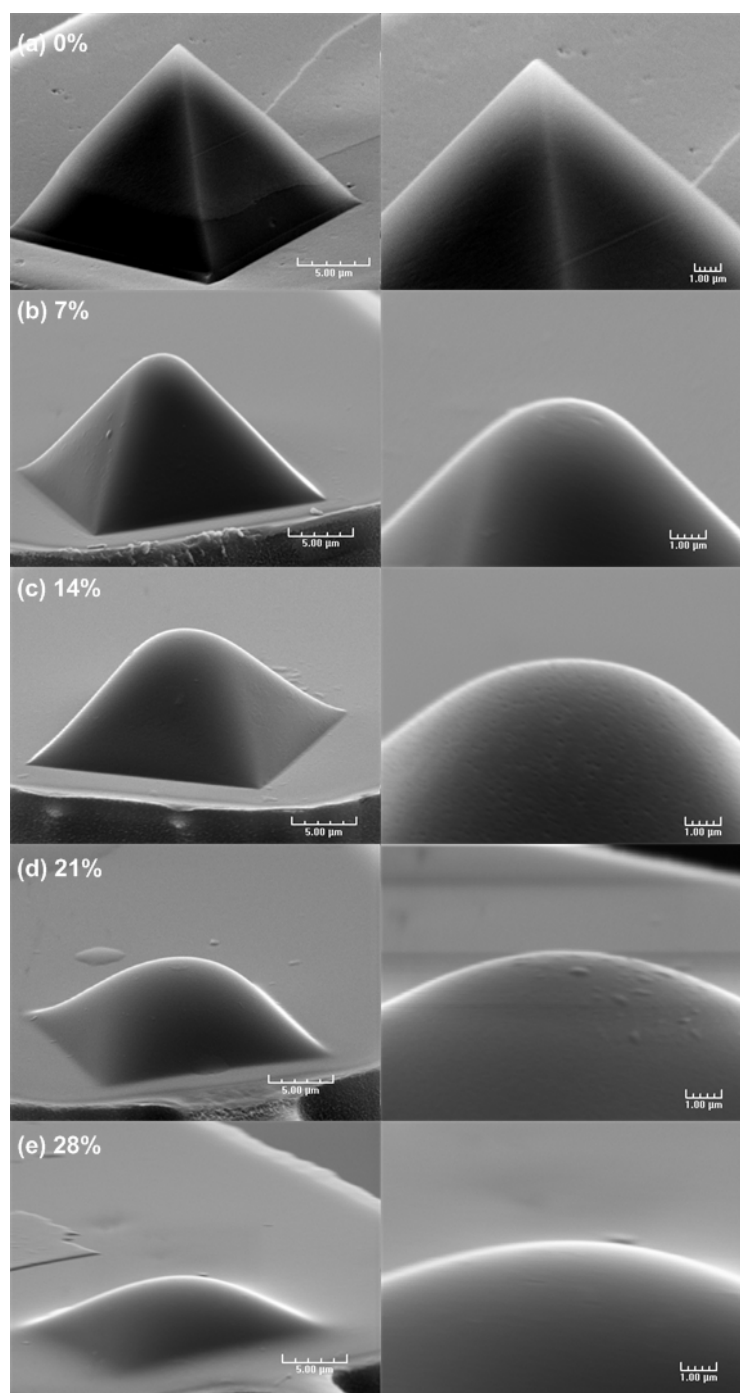


Figure 51. Scanning electron micrograph showing SPM tips with different radius of curvature where the tip radius of curvature is controlled by changing the solid content (%) or viscosity of the photoresist mould filling material. a) No photoresist filling 0%; b) 7.075 %; c) 14.15 %; d) 21.225 %; e) 28.3 %.

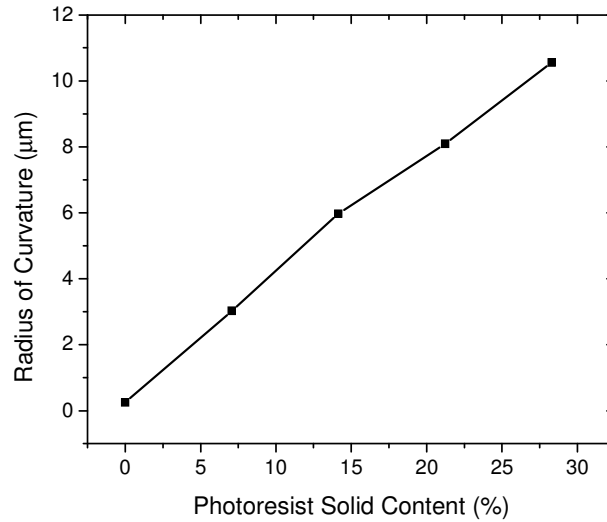


Figure 52. Plot of the tip radius of curvature versus photoresist solid concentration.

6.3.2 Number of Coating Cycles vs. Tip Radius of Curvature

The second method developed for controlling the tip radius of curvature is based on layer-by-layer filling. Here, the cavities are coated with multiple layers of filling material which are built subsequently on top of each other (figure 53). First a suitable photoresist concentration is selected and several cycles of spin coating and baking is conducted. Spinning and baking conditions are the same as in the previous case (4000 rpm, 30 sec. followed by 95°C, 1 min. softbake and 4 hr. 135°C hardbake) and baking is carried out after each new spinning. To increase the range of achievable number of layers and thus the tip radius of curvature, a low photoresist solid content of 7 % was chosen.

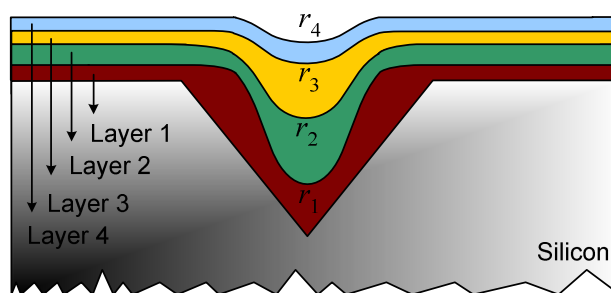


Figure 53. Illustration of the layer-by-layer filling process for controlling the tip radius of curvature.

Samples with bulk-etched cavities were processed, and exposed to different number of spin coating cycles. Up to 4 layers were coated and probes were fabricated on these samples which had multiple layers of filling material. Later, probes were released and imaged under an SEM which revealed different tip radius of curvature for different number of spin coatings (figures 54(a)-(d)). This indicates that layer-by-layer filling allows controllable build-up of material inside cavities and thus the probe tip radius of curvature can be controlled through conducting different number of spin-coat cycles during mould filling. The plot of the tip radius of curvature versus number of spins shows that, the tip curvature ranges from $\sim 2.8\mu\text{m}$ to $5.3\mu\text{m}$ with increasing spin coating cycles from 1 to 4 (figure 55).

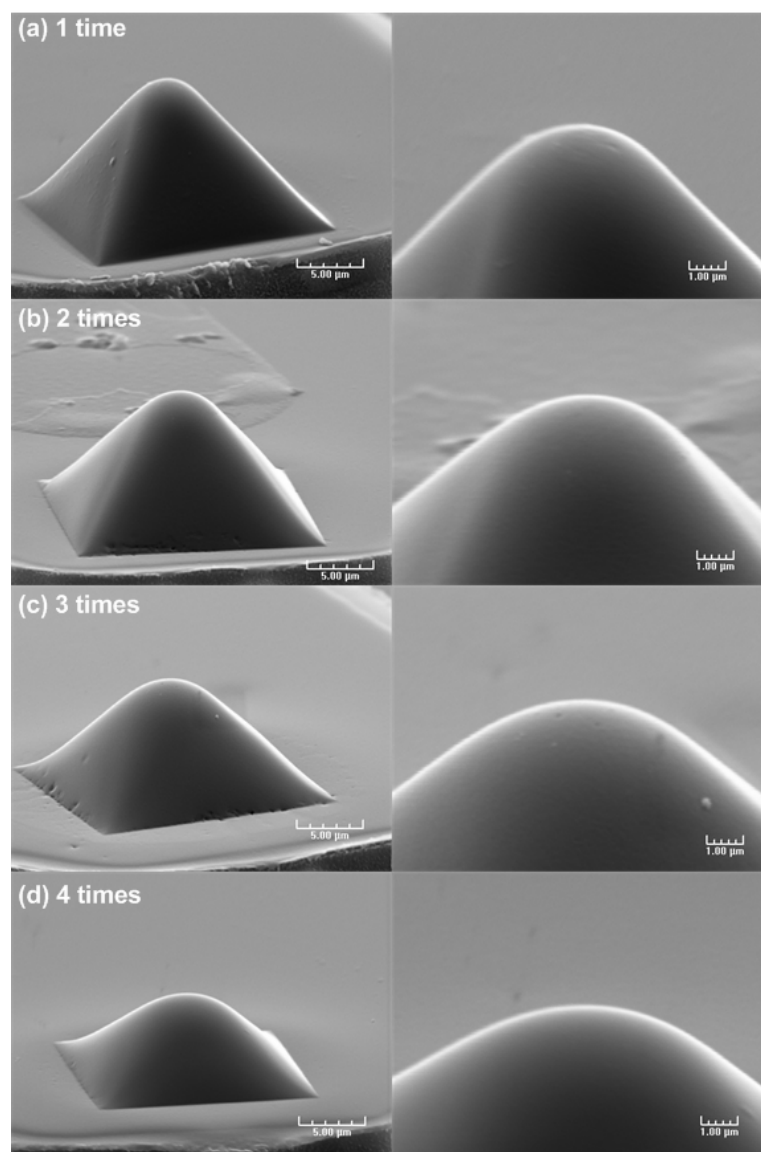


Figure 54. Scanning electron micrograph showing SPM tips with different radius of curvature where the tip radius of curvature is controlled by spinning multiple layers of photoresist at a fixed solid content (7.075 %). a) 1 time of spinning; b) 2 times; c) 3 times; d) 4 times.

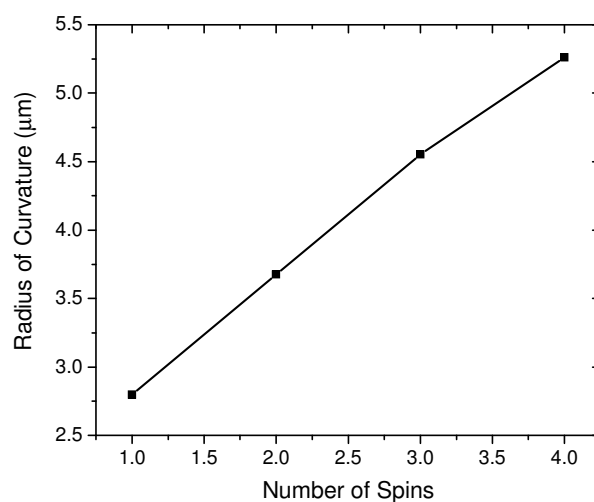


Figure 55. Plot of the tip radius of curvature versus number of photoresist spin cycles.

6.4 Discussion and Conclusions

A new technology for mass-fabrication of scanning probes with curved tips was developed and successfully implemented. The technique allows control of the tip radius of curvature simply by changing the concentration of the filling material or the number of spin-coat cycles. The development of this new technology will provide rapid fabrication of colloidal probes with desired tip radius of curvature and will be useful in many applications like scanning probe lithography, colloid probe force microscopy and biological applications.

CHAPTER VII

CONCLUSIONS

The major goal that was set before conducting this study was to demonstrate the usefulness of probes as a key tool in enabling and facilitating research in biological and nanotechnology applications. To prove this hypothesis, 5 different kinds of probes along with their applications in biology and nanotechnology were presented. 1) MEMS-based electromagnetic probe (cell/particle manipulation, single cell magnetic stimulation); 2) permalloy-coated tungsten electromagnetic probe (droplet manipulation, digital microfluidics); 3) Gold-coated scanning probe (direct write of metallic micro/nano structures); 4) Scanning probes with flat tips having precisely defined contact areas (dip-pen/scanning probe nanolithography, cell mechanics); 5) Colloidal scanning probes with curved tips (dip-pen/scanning probe nanolithography, cell mechanics, colloidal force microscopy, interfacial studies). The development of the probes included multiple steps that range from establishing new microfabrication technology to implementing novel characterization techniques and experimentation methods. Following development phases, the probes were used in some of the above-mentioned applications to demonstrate functionality and feasibility.

It has been shown in this study that “probes” are key enablers and indispensable tools to investigate micro/nano scale phenomena due to three major reasons. First, each micro/nano scale application requires a well-defined interaction volume; and this can be achieved through the unique tip geometry of a probe. Second, probes can be used either as sensors or actuators and can be designed to provide different stimuli (electrical, magnetic, mechanical), which allows them to be used for a variety of applications. Third, the ability of probes to be easily mounted on micromanipulators provides them with superior positioning, motion and scanning capability. Through the different probe designs discussed in this thesis, it has been demonstrated that by either controlling the tip geometry or by adding “new” stimulus sources (e.g. electromagnetic, electric, thermal, mechanical stimuli), probes can be tailored for a multitude of applications.

REFERENCES

- [1] Lee C S, Lee H and Westervelt R M 2001 Microelectromagnets for the control of magnetic nanoparticles *Appl. Phys. Lett.* **79** 3308-10
- [2] Deng T, Whitesides G M, Radakrishnan M, Zabow G and Prentiss M 2001 Manipulation of magnetic microbeads in suspension using micromagnetic systems fabricated with soft lithography *Appl. Phys. Lett.* **78** 1775-7
- [3] Lee H, Purdon A M and Westervelt R M 2004 Manipulation of biological cells using a microelectromagnet matrix *Appl. Phys. Lett.* **85** 1063-5
- [4] Lee H, Purdon A M, Chu V and Westervelt R M 2004 Controlled assembly of magnetic nanoparticles from magnetotactic bacteria using microelectromagnets arrays *Nano Lett.* **4** 995-8
- [5] Rong R, Choi J-W and Ahn C H 2006 An on-chip magnetic bead separator for biocell sorting *J. Micromech. Microeng.* **16** 2783-90
- [6] Smistrup K, Tang P T, Hansen O and Hansen M F 2006 Microelectromagnet for magnetic manipulation in lab-on-a-chip systems *J. Magn. Magn. Mater.* **300** 418-26
- [7] Pekas N, Granger M, Tondra M, Popple A and Porter M D 2005 Magnetic particle diverter in an integrated microfluidic format *J. Magn. Magn. Mater.* **293** 584-88
- [8] Mirowski E, Moreland J, Russek S E and Donahue M J 2004 Integrated microfluidic isolation platform for magnetic particle manipulation in biological systems *Appl. Phys. Lett.* **84** 1786-8
- [9] Berger M, Castelino J, Huang R, Shah M and Austin R H 2001 Design of a microfabricated magnetic cell separator *Electrophoresis* **22** 3883-92
- [10] Walsh V and Cowey A 2000 Transcranial magnetic stimulation and cognitive neuroscience *Nature Rev. Neurosci.* **1** 73-9
- [11] Loo C K and Mitchell P B 2005 A review of the efficacy of transcranial magnetic stimulation (TMS) treatment for depression, and current and future strategies to optimize efficacy *J. Affect. Disord.* **88** 255-67

- [12] George M S, Wassermann E M, Kimbrell T A, Little J T, Williams W E, Danielson A L, Greenberg B D, Hallett M and Post R M 1997 Mood improvement following daily left prefrontal repetitive transcranial magnetic stimulation in patients with depression: a placebo-controlled crossover trial *Am. J. Psychiatry* **154** 1752-6
- [13] Massot O, Grimaldi B, Bailly J M, Kochanek M, Deschamps F, Lambrozo J and Fillion G 2000 Magnetic field desensitizes 5-HT_{1B} receptor in brain: pharmacological and functional studies *Brain Res.* **858** 143-50
- [14] Espinosa J M, Liberti M, Lagroye I and Veyret B 2006 Exposure to AC and DC magnetic fields induces changes in 5-HT_{1B} receptor binding parameters in rat brain membranes *Bioelectromagnetics* **27** 414-22
- [15] Rohan M, Parow A, Stoll A L, Demopulos C, Friedman S, Dager S, Hennen J, Cohen B M and Renshaw P F 2004 Low-field magnetic stimulation in bipolar depression using an MRI-based stimulator *Am. J. Psychiatry* **161** 93-8
- [16] Carlezon W A, Rohan M L, Mague S D, Meloni E G, Parsegian A, Cayetano K, Tomasiewicz H C, Rouse E D, Cohen B M and Renshaw P F 2005 Antidepressant-like effects of cranial stimulation within a low-energy magnetic field in rats *Biol. Psychiatry* **57** 571-6
- [17] Repacholi M H and Greenebaum B 1999 Interaction of static and extremely low frequency electric and magnetic fields with living systems: health effects and research needs *Bioelectromagnetics* **20** 133-60
- [18] Fitzpatrick S M and Rothman D L 2000 Meeting report: transcranial magnetic stimulation and studies of human cognition *J. Cogn. Neurosci.* **12** 704-9
- [19] Ueno S, Tashiro T and Harada K 1988 Localized stimulation of neural tissues in brain by means of a paired configuration of time-varying magnetic fields *J. Appl. Phys.* **64** 5862-4
- [20] Barbic M, Mock J J, Gray A P and Schultz S 2001 Scanning probe electromagnetic tweezers *Appl. Phys. Lett.* **79** 1897-9

- [21] Matthews B D, LaVan D A, Overby D R, Karavitis J and Ingber D E 2004 Electromagnetic needles with submicron pole tip radii for nanomanipulation of biomolecules and living cells *Appl. Phys. Lett.* **85** 2968-70
- [22] Chomnawang N, Lee J-B and Davis W A 2003 Surface micromachined arch-shape 3D solenoid inductors for high frequency applications *J. Microlith. Microfab. Microsyst.* **2** 275-281
- [23] Lu H, Lee J-C, Pillans B, Kim K and Lee J-B 2007 High aspect ratio air core solenoid inductors using an improved UV-LIGA process with contrast enhancement material," *Microsyst. Technol.* **13** 237-43
- [24] Yoon J-B, Kim B-K, Han C-H, Yoon E, Lee K and Kim C K 1998 High-performance electroplated solenoid-type integrated inductor (SI^2) for RF applications using simple 3D surface micromachining technology in *Proc. IEEE Int. Electron Devices Meeting*, San Francisco, CA, 544-7
- [25] Thiaville A, Belliard L, Majer D, Zeldov E and Miltat J 1997 Measurement of the stray field emanating from magnetic force microscope tips by Hall effect microsensors *J. Appl. Phys.* **82** 3182-91
- [26] Chang A M, Hallen H D, Harriott L, Hess H F, Kao H L, Kwo J, Miller R E, Wolfe R, Van der Ziel J and Chang T Y 1992 Scanning Hall probe microscopy *Appl. Phys. Lett.* **61** 1974-6
- [27] Pankhurst Q A, Connolly J, Jones S K and Dobson J 2003 Applications of magnetic nanoparticles in biomedicine *J. Phys. D.: Appl. Phys.* **36** R167-81
- [28] Ahn C H, Allen M G, Trimmer W, Jun Y-N and Erramilli S 1996 A fully integrated micromachined magnetic particle separator *J. Microelectromech. Syst.* **5** 151-8
- [29] Chiou C-H and Lee G-B 2005 A micromachined DNA manipulation platform for the stretching and rotation of a single DNA molecule *J. Micromech. Microeng.* **15** 109-17
- [30] Park J Y and Allen M G 1998 Development of magnetic materials and processing techniques applicable to integrated micromagnetic devices *J. Micromech. Microeng.* **8** 307-16

- [31] Chiou C-H, Huang Y-Y, Chiang M-H, Lee H-H and Lee G-B 2006 New magnetic tweezers for investigation of the mechanical properties of single DNA molecules *Nanotechnol.* **17** 1217-24
- [32] Pollack M G, Shenderov A D and Fair R B 2002 Electrowetting-based actuation of droplets for integrated microfluidics *Lab Chip* **2** 96-101
- [33] Taniguchi T, Torii T and Higuchi T 2002 Chemical reactions in microdroplets by electrostatic manipulation of droplets in liquid media *Lab Chip* **2** 19-23
- [34] Velev O D, Prevo B G and Bhatt K H 2003 On-chip manipulation of free droplets *Nature* **426** 515-16
- [35] Srinivasan V, Pamula V K and Fair R B 2004 Droplet-based microfluidic lab-on-a-chip for glucose detection *Anal. Chim. Acta.* **507** 145-50
- [36] Dorvee J R, Derfus A M, Bhatia S N and Sailor M J 2004 Manipulation of liquid droplets using amphiphilic crystal chaperones *Nature Mat.* **3** 896-9
- [37] Yamada R and Tada H 2005 Manipulation of droplets by dynamically controlled wetting gradients *Langmuir* **21** 4254-6
- [38] Ohashi T, Kuyuma H, Hanafusa N and Togowa Y 2007 A simple device using magnetic transportation for droplet-based PCR *Biomed. Microdev.* **9** 695-702
- [39] Wang Y, Zhao Y and Cho S K 2007 Efficient in-droplet separation of magnetic particles for digital microfluidics *J. Micromech. Microeng.* **17** 2148-56
- [40] Yi C, Li C W, Ji S and Yang M 2006 Microfluidics technology for manipulation and analysis of biological cells *Anal. Chim. Acta.* **560** 1-23
- [41] Lehmann U, Hadjidi S, Parashar V K, Vandevyver C, Rida A and Gijs M A M 2006 Two-dimensional magnetic manipulation of microdroplets on a chip as a platform for bioanalytical applications *Sens. Actuators B* **117** 457-63
- [42] Nguyen N T, Ng K M and Huang X 2006 Manipulation of ferrofluid droplets using planar coils *Appl. Phys. Lett.* **89** 052509
- [43] Pamme N 2006 Magnetism and microfluidics *Lab Chip* **6** 24-38
- [44] Ramadan Q, Yu C, Samper V and Poenar D P 2006 Microcoils for transport of magnetic beads *Appl. Phys. Lett.* **88** 032501

- [45] Rong R, Choi J W and Ahn C H 2006 An on-chip magnetic bead separator for biocell sorting *J. Micromech. Microeng.* **16** 2783-90
- [46] Joung J, Shen J and Grodzinski P 2000 Micropumps based on alternating high-gradient magnetic fields *IEEE Trans. Magn.* **36** 2012-4
- [47] Johnk C T A 1988 *Engineering electromagnetic fields and waves* 2nd edn. Wiley, NY
- [48] Müller A D, Müller F and Hietscholda M 2000 Localized electrochemical deposition of metals using micropipettes *Thin Solid Films* **366** 32-6
- [49] Said R A 2003 Microfabrication by localized electrochemical deposition: experimental investigation and theoretical modeling *Nanotechnol.* **14** 523-531
- [50] Morgan S M, Al-Shamkhani A, Callant D, Schacht E, Woodley J F, Duncan R 1995 Alginates as drug carriers: covalent attachment of alginates to therapeutic agents containing primary amine groups. *Int. J. Pharmaceutics* **95** 121-8
- [51] Pasparakis G and Bouropoulos N 2006 Swelling studies and *in vitro* release of verapamil from calcium alginate and calcium alginate–chitosan beads *Int. J. Pharm.* **323** 34-42
- [52] Goosen M F A, Al-Ghafri A S, Mardi O E, Al-Belushi M I J, Al-Hajri H A, Mahmoud E S E, Consolacion E C 1997 Electrostatic Droplet Generation for Encapsulat ion of Somatic Tissue: assessment of High-Voltage Power Supply *Biotechnol. Prog.* **13** 497-502
- [53] Poncelet D, Neufeld R J, Goosen M F A, Burgarski B and Babak V 1999 Formation of microgel beads by electric dispersion of polymer solutions *AIChE J.* **45** 2018-23
- [54] Jayasinghea S N and Townsend-Nicholson A 2006 Stable electric-field driven cone-jetting of concentrated biosuspensions *Lab Chip* **6** 1086–90
- [55] Xie J and Wang C H 2007 Electrospray in the dripping mode for cell microencapsulation *J. Coll. Int. Sci.* **312** 247–55
- [56] Zborowski M, Sun L, Moore L R, Williams P S and Chalmers J J 1999 Continuous cell separation using novel magnetic quadrupole flow sorter *J. Magn. Magn. Mater.* **194** 224-30

- [57] Quate C F 1997 Scanning probes as a lithography tool for nanostructures *Surf. Sci.* **386** 259-64
- [58] Maynor B W, Li Y and Liu J 2001 Au “ink” for AFM “dip-pen” nanolithography *Langmuir* **17** 2575-8
- [59] Piner R D, Zhu J, Xu F, Hong S and Mirkin C A 1999 Dip-pen nanolithography *Science* **283** 661-3
- [60] Pumarol M E, Miyahara Y, Gagnon R and Grütter P 2005 Controlled deposition of gold nanodots using non-contact atomic force microscopy *Nanotechnol.* **16** 1083-8
- [61] Fujita D, Onishi K and Kumakura T 2003 Silver nanostructures formation on Si (111)-(7×7) surfaces by the tip of a scanning tunneling microscope *Jpn. J. Appl. Phys. Part 1* **42** 4773-6
- [62] Nelson B A, King W P, Laracuente A R, Sheehan P E and Whitman L J 2006 Direct deposition of continuous metal nanostructures by thermal dip-pen nanolithography *Appl. Phys. Lett.* **88** 033104
- [63] Bowden F P and Tabor D 1958 *The Friction and Lubrication of Solids* Clarendon Press, Oxford, UK
- [64] Fischer T 1988 Tribochemistry *Annu. Rev. Mater. Sci.* **18** 303-8
- [65] Heinicke G 1984 *Tribochemistry* Carl Hanser Verlag, Munich, Germany
- [66] Martin J M, Mogne Th Le, Grossiord C and Palermo T 1997 UHV friction of tribofilms derived from metal dithiophosphates *Tribology Lett.* **3** 87-94
- [67] Martin J M 1999 Antiwear mechanisms of zinc dithiophosphate: a chemical hardness approach *Tribology Lett.* **6** 1-8
- [68] Rigney D A and Hammerberg J E 1998 Unlubricated sliding behavior of metals *MRS Bulletin* **23** 32-6
- [69] Dickinson J T, Park N-S, Kim M-W and Langford S C A 1997 Scanning force microscope study of a tribochemical system: stress-enhanced dissolution *Tribology Lett.* **3** 69-80
- [70] Strosio J A and Eigler D M 1991 Atomic and molecular manipulation with the scanning tunneling microscope *Science* **254** 1319-26

- [71] Severs P, Soboleff J, Xu H and Liang H 2004 Friction-Induced Nano-Islands *Proc. of NSF Design, Service and Manufacturing Grantees and Research Conf.* SMU, Dallas, TX
- [72] Yeh J-J, Hwang J, Bertness K, Friedman D J, Cao R and Lindau I 1993 Growth of the room temperature Au/Si(111)-7×7 interface *Phys. Rev. Lett.* **70** 3768-71
- [73] Li C Z, He H X, Bunch J S and Tao N J 2000 Molecular detection based on conductance quantization of nanowires *Appl. Phys. Lett.* **76** 1333-5
- [74] Hahm J-I and Lieber C M 2004 Direct ultrasensitive electrical detection of DNA and DNA sequence variations using nanowire nanosensors *Nano Lett.* **4** 51-4
- [75] Radke S M and Alocilja E C 2005 A microfabricated biosensor for detecting foodborne bioterrorism agents *IEEE Sensors J.* **5** 744-50
- [76] Chuang W-H, Luger T, Fettig R K and Ghodssi R 2004 Mechanical property characterization of LPCVD silicon nitride thin films at cryogenic temperatures *J. Microelectromech. Syst.* **13** 870-9
- [77] Samori P 2004 Scanning probe microscopies beyond imaging *J. Mater. Chem.* **14** 1353-66
- [78] Garcia R, Martinez R V and Martinez J 2006 Nano-chemistry and scanning probe nanolithographies *Chem. Soc. Rev.* **35** 29–38
- [79] Xie X N, Chung H J, Sow C H and Wee A T S 2006 Nanoscale materials patterning and engineering by atomic force microscopy nanolithography *Mat. Sci. and Eng. Rev.* **54** 1–48
- [80] Ducker W A, Senden T J and Pashley R M 1991 Direct measurement of colloidal forces using an atomic force microscope *Nature* **353** 239-41
- [81] Berdyeva T K, Woodworth C D and Sokolov I 2005 Human epithelial cells increase their rigidity with ageing *in vitro*: direct measurements *Phys. Med. Biol.* **50** 81–92
- [82] Ke C, Humeniuk M, Gracz H S and Marszalek P E 2007 Direct measurements of base stacking interactions in DNA by single-molecule atomic-force spectroscopy *Phys. Rev. Lett.* **99** 018302

- [83] Kawakami M, Byrne K, Khatri B S, Mcleish T C B, Radford S E and Alastair D S 2005 Viscoelastic measurements of single molecules on a millisecond time scale by magnetically driven oscillation of an atomic force microscope cantilever *Langmuir* **21** 4765-72
- [84] Despont M, Takahashi H, Ichihara S, Shirakawabe Y, Shimizu N, Inoue A, Häberle W, Binnig G K and Vettiger P 2000 Dual-cantilever AFM probe for combining fast and coarse imaging with high-resolution imaging *Proc. 13th Int. Conf. on MEMS (Micro Electro Mechanical Systems)* Miyazaki, Japan, 126-31
- [85] Boisen A, Hansen O and Bouwstra S 1996 AFM probes with directly fabricated tips *J. Micromech. Microeng.* **6** 58-62
- [86] Chui B W, Stowe T D, Ju Y S, Goodson K E, Kenny T W, Mamin H J, Terris B D, Ried R P and Rugar D 1998 Low-Stiffness silicon cantilevers with integrated heaters and piezoresistive sensors for high-density AFM thermomechanical data storage *J. Microelectromech. Syst.* **7** 69-78
- [87] Wolter O, Bayer Th and Greschner J 1991 Micromachined silicon sensors for scanning force microscopy *J. Vac. Sci. Technol. B* **9** 1353-7
- [88] Chiou C-H, Chang S-J, Lee G-B and Lee H-H 2006 New fabrication process for monolithic probes with integrated heaters for nanothermal machining *Jap. J. App. Phys.* **45** 208-14
- [89] Liu C and Gamble R 1998 Mass producible monolithic silicon probes for scanning microscopes *Sens. Actuators A* **71** 233-7
- [90] Wang X and Liu C 2005 Multifunctional probe array for nano patterning and imaging *Nano Lett.* **5** 1867-72
- [91] Schneegans O, Houze F, Meyer R and Boyer L 1998 Study of the local electrical properties of metal surfaces using an AFM with a conducting probe *IEEE Trans. Compon. Packag. Manuf. Technol. A* **21** 76-81
- [92] Zou J, Wang X, Bullen D, Ryu K, Liu C and Mirkin C A 2004 A mould-and-transfer technology for fabricating scanning probe microscopy probes *J. Micromech. Microeng.* **14** 204-11

- [93] Baek C-W, Kim Y-K, Ahn Y and Kim Y-H 2005 Measurement of the mechanical properties of electroplated gold thin films using micromachined beam structures *Sens. Actuators A* **117** 17–27
- [94] Salaita K, Wang Y and Mirkin C A 2007 Applications of dip-pen nanolithography *Nat. Nanotechnol.* **2** 145-55
- [95] Hong S, Zhu J and Mirkin C A 1999 Multiple ink nanolithography: toward a multiple-pen nano-plotter *Science* **286** 523-5
- [96] Zhang H, Elghanian R, Amro N A, Disawal S and Eby R 2004 Dip pen nanolithography stamp tip *Nano Lett.* **4** 1649-55
- [97] Su M and Dravid V P 2002 Colored-ink dip-pen nanolithography *Appl. Phys. Lett.* **80** 4434-6
- [98] Radmacher M 1997 Measuring the elastic properties of biological samples with the AFM *IEEE Eng. Med. Biol. Mag.* **16** 47-57
- [99] Cohen S R and Bitler A 2008 Use of AFM in bio-related systems *Curr. Opin. Colloid Interface Sci.* **13** 316-25
- [100] Sagvolden G, Giaever I, Pettersen E O and Feder J 1999 Cell adhesion force microscopy *Proc. Nat. Acad. Sci. USA* **96** 471-6
- [101] Benoit M, Gabriel D, Gerisch G and Gaub H E 2000 Discrete molecular interactions in cell adhesion measured by force spectroscopy *Nat. Cell Biol.* **2** 313-7
- [102] Lulevich V, Zink T, Chen H Y, Liu F T and Liu G Y 2006 Cell mechanics using atomic force microscopy-based single-cell compression *Langmuir* **22** 8151-5
- [103] Li X and Logan B E 2004 Analysis of bacterial adhesion using a gradient force analysis method and colloidal probe atomic force microscopy *Langmuir* **20** 8817-22
- [104] Kappl M and Butt H-J 2002 The colloidal probe technique and its application to adhesion force measurements *Part. Part. Syst. Charact.* **19** 129-43
- [105] H-J Butt 1991 Measuring electrostatic, van der Waals, and hydration forces in electrolyte solutions with an atomic force microscope *Biophys. J.* **60** 1438-44

- [106] Schaefer D M, Carpenter M, Reifenger R, Demejo L P and Rimai D S 1994 Surface force interactions between micrometer-size polystyrene spheres and silicon substrates using atomic force techniques *J. Adhesion Sci. Technol.* **8** 197-210
- [107] Giesbers M, Kleijn J M, Fleer G J and Cohen Stuart M A 1998 Forces between polymer-covered surfaces: a colloidal probe study *Colloids Surf. A: Phys. Eng. Aspects* **142** 343-53
- [108] Zauscher S and Klingenberg D J 2000 Normal forces between cellulose surfaces measured with colloidal probe microscopy *J. Colloid and Interface Sci.* **229** 497-510
- [109] Bowen W R, Hilal N, Lovitt R W and Wright C J 1998 A new technique for membrane characterization: direct measurement of the force of adhesion of a single particle using an atomic force microscope *J. Membr. Sci.* **157** 269-74
- [110] Tortonese M 1997 Cantilevers and tips for atomic force microscopy *IEEE Eng. Med. Biol. Mag.* **16** (2) 28-33
- [111] Pasche S, Textor M, Meagher L, Spencer N D and Griesser H J 2005 Relationship between Interfacial Forces Measured by Colloid-Probe Atomic Force Microscopy and Protein Resistance of Poly(ethylene glycol)-Grafted Poly(L-lysine) Adlayers on Niobia Surfaces *Langmuir* **21** (14) 6508-20
- [112] Butt H-J, Cappella B and Kappl M 2005 Force measurements with the atomic force microscope: technique, interpretation and applications *Surf. Sci. Reports* **59** 1–152
- [113] Gan Y 2007 Invited review article: a review of techniques for attaching micro and nanoparticles to a probe's tip for surface force and near-field optical measurements *Rev. Sci. Instrum.* **78** 081101
- [114] Huttl G, Beyer D and Muller 1997 Investigation of electrical double layers on SiO₂ surfaces by means of force vs. distance measurements *Surf. Interface Anal.* **25** 543-7
- [115] Huttl G, Klemm V, Popp R, Simon F and Muller E 2002 Tailored colloidal AFM probes and their TEM investigation *Surf. Interface Anal.* **33** 50-3
- [116] Pucci G, De Santo M P, Carbone G and Barberi R 2006 A novel method to prepare probes for atomic force spectroscopy *Digest J. Nanomat. Biostr.* **1** 99-103

- [117] Yapici M K, Lee H, Zou J and Liang H 2008 Gold-coated scanning probes for direct “write” of sub-micron metallic structures, *Micro Nano Lett.* **3** 90-4
- [118] Hui X, Guo-hua X and Yue A 2006 A novel colloid probe preparation method based on chemical etching technique *J. Zhejiang Univ. Sci. B* **7** 304-9
- [119] Ravi T S, Marcus R B and Liu D 1991 Oxidation sharpening of silicon tips *J. Vac. Sci. Technol. B* **9** 2733-7
- [120] Madou M J 2002 *Fundamentals of Microfabrication: The Science of Miniaturization*, CRC Press, Boca Raton, FL
- [121] Albrect T R, Akamine S, Carver T E and Quate C F 1990 Microfabrication of cantilever styli for the atomic force microscope *J. Vac. Sci. Technol. A* **8** 3386-96
- [122] Stillwagon L E and Larson R G 1990 Leveling of thin films over uneven substrates during spin coating *Phys. Fluids A*. **2** 1937-43

VITA

Murat Kaya Yapici was born in Adana, Turkey in 1982. He received his middle and high school education at Uskudar American Academy. In May of 2004 he graduated from Texas A&M University, College Station with a B.S. degree in electrical engineering; and continued his PhD studies in the Solid State Electronics, Photonics and Nano-Engineering Laboratory under the same department. He has been conducting interdisciplinary research on MEMS, microsystems and nanotechnology since then. Upon joining the program, he worked on developing new micromachining technology for RF micro electromechanical systems. His current research interests lie in the development of micro/nano electromechanical devices/systems, sensors and actuators for biological applications and novel nano fabrication technology based on scanning probe techniques. He also served as a teaching assistant for the “Microelectronic Circuit Fabrication” and “Digital Systems Design” courses. During his graduate studies, he published seven peer-reviewed journal articles, has been an author on ten conference proceedings and had the opportunity to present his research in national and international symposia. He can be reached at his permanent address:

Akdogan Sk. Ay Apt.
40/7 Besiktas 80690
Istanbul, TURKEY.